Report No. C-SAFE-CD-IR-05-001

TAYLOR IMPACT TESTS: DETAILED REPORT

Biswajit Banerjee

Department of Mechanical Engineering, University of Utah, Salt Lake City, UT 84112, USA

Abstract

Taylor impacts tests were originally devised to determine the dynamic yield strength of materials at moderate strain rates. More recently, such tests have been used extensively to validate numerical codes for the simulation of plastic deformation. In this work, we use the material point method to simulate a number of Taylor impact tests. The goal is to partially validate some plasticity models used by the UINTAH multi-physics code. In addition, we would like to determine the plasticity model that is most appropriate for fire-structure interaction problems that are being simulated using UINTAH. We compare the Johnson-Cook, Steinberg-Cochran-Guinan-Lund, Zerilli-Armstrong, Mechanical Threshold Stress, and the Preston-Tonks-Wallace plasticity models. We evaluate these models for OFHC copper, 6061-T6 aluminum alloy, and 4340 steel alloy at various temperatures and strain rates. A number of validation metrics are presented for quantitative comparisons of numerical simulations and experimental data. It is observed that the accuracy of all the models drops when the initial conditions involve high temperatures and high impact velocities.

1 INTRODUCTION

The Taylor impact test (Taylor [86]) was originally devised as a means of determining the dynamic yield strength of solids. The test involves the impact of a flat-nosed cylindrical projectile on a hard target at normal incidence. Taylor provided an analytical solutions for the dynamic yield strength of the material of the projectile based on the length of the elastic region and the radius of the region of permanent set. As described by Whiffin [93], that use of the test was limited to relatively small deformations obtained from low velocity impacts. Though the Taylor impact test continues to be used to determine yield strengths of materials at high strain rates, the test is limited to peak strains of around 0.6 at the center of the specimen (Johnson and Holmquist [51]). For higher strains and strain rates, the Taylor test is currently used more as a means of validating plasticity models in numerical codes

for the simulation of high rate phenomena such as impact and explosive deformation as suggested by Zerilli and Armstrong [99].

In this paper, we describe our experience in validating the plasticity models in a parallel, multi-physics code (UINTAH) that uses the material point method (Sulsky et al. [83, 84]) and an implicit compressible Eulerian CFD code for simulating fire-structure interactions. A number of different validation tests such as uniaxial tension, flyer-plate impact, high velocity impact and penetration, and expanding ring fragmentation have been performed to validate plasticity and failure models in Uintah. In this paper, we have chosen to describe the results of Taylor impact tests for various strain rates and temperatures without considering any failure or damage. These tests provide a second layer of validation for the plasticity models beyond uniaxial tension tests. We also present a number of metrics that can be used to compare simulations and experiments for Taylor impact tests. These metrics can be used to better quantify the modeling errors in large-scale multi-physics simulations.

The objectives of the simulations presented in this paper are:

(1) To select a phenomenological plasticity model that is best suited for the fire-structure interaction problems to be simulated by UINTAH.
(2) To quantify the modeling errors that we incur while using a particular plasticity model.

The available experimental data at high temperatures (for high strain rate deformations) are sparse and often unreliable. We would caution that a decision on either of the above objectives cannot be made solely on the basis of Taylor impact tests and needs to be augmented with other validation tests.

The organization of this paper is as follows. Section 2 provides the background for the current study. Section 3 discusses the plasticity models, the equation of state, and the shear modulus and melting temperature models. A brief discussion of the materials is provided in Section 4. Validation metrics are identified and their significance is discussed in Section 5.1. Comparisons between experimental data and simulations of Taylor impact tests using the validation metrics are described in Section 5. Finally, conclusions and suggestions are presented in Section 6.

2 BACKGROUND

The goal of this work is to present some results and insights we have obtained during the process of validation of plasticity models within the multi-physics UINTAH code (de St. Germain et al. [29]). This code is used to simulate of the deformation and failure of a steel container due to gases produced by an explosively reacting high energy material (PBX 9501) contained inside. The entire process is simulated

using the massively parallel, Common Component Architecture (Armstrong et al. [3]) based, UINTAH Computational Framework (UCF) (de St. Germain et al. [29]).

Figure 1 shows the result of a simulation of a coupled fire-container-explosion using UINTAH. The simulation involves a fire that heats the steel container to a temperature exceeding the burn temperature of the high energy material (450 K to 600 K). The heated high energy material reacts and produces gases. These gases pressurize the container from inside and deform it plastically. The initial strain rates in the container during this process are around 1/s. However, the explosive nature of the high energy material rapidly increases the rate of straining to a peak of around 10^8/s. At some point in the process, large cracks develop in the container and fragments are produced. Experiments conducted at the University of Utah have shown that failure of the container can be due to ductile fracture associated with void coalescence and adiabatic shear bands. Depending on the geometry of the high energy material, the container either breaks into fragments or into a few large pieces.

The dynamics of the solid materials - steel and PBX 9501 - is modeled using the Lagrangian Material Point Method (MPM) (Sulsky et al. [83]). Gases are generated from solid PBX 9501 using a burn model (Long and Wight [58]). Gas-solid interaction is accomplished using an Implicit Continuous Eulerian (ICE) multi-material hydrodynamic code (Guilkey et al. [36]). A single computational grid is used for all the materials. A brief description of the Material Point Method is given in Appendix A.

The constitutive response of PBX 9501 is modeled using ViscoSCRAM (Bennett et al. [18]), which is a five element generalized Maxwell model for the viscoelastic response coupled with statistical crack mechanics. Solid PBX 9501 is

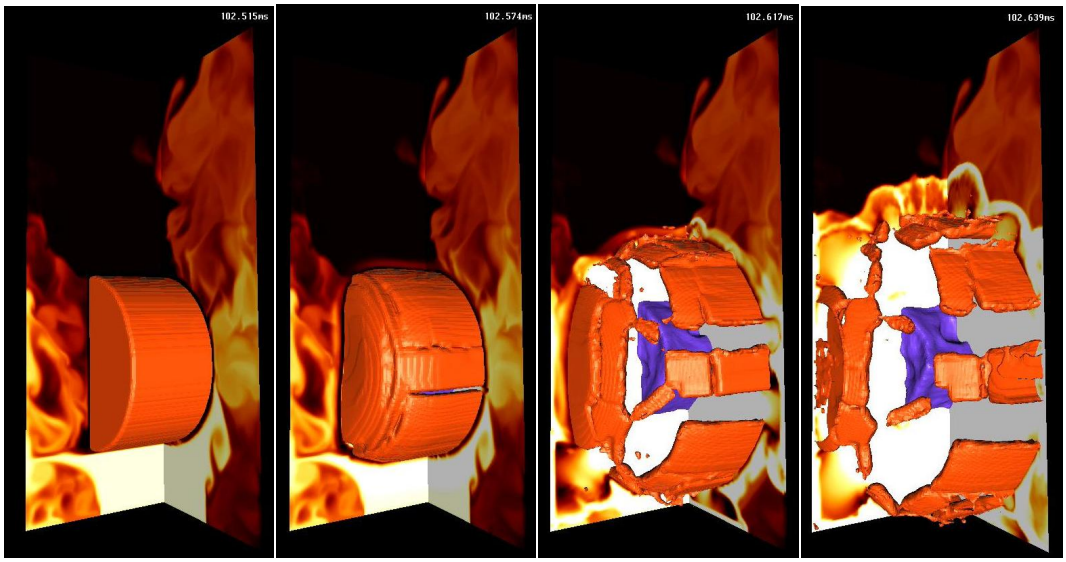

Fig. 1. Simulation of exploding cylinder.

progressively converted into a gas with an appropriate equation of state. The temperature and pressure in the gas increase rapidly as the reaction continues. As a result, the steel container is pressurized, undergoes plastic deformation, and finally fragments.

The main issues regarding the constitutive modeling of the steel container are the selection of appropriate models for nonlinear elasticity, plasticity, damage, loss of material stability, and failure. The numerical simulation of the steel container involves the choice of appropriate algorithms for the integration of balance laws and constitutive equations, as well as the methodology for fracture simulation. Models and simulation methods for the steel container are required to be temperature sensitive and valid for large distortions, large rotations, and a range of strain rates (quasistatic at the beginning of the simulation to approximately 10^8 s^{-1} at fracture).

The approach chosen in UINTAH is to assume an additive decomposition of the spatial rate of deformation tensor into elastic and plastic parts. The Cauchy stress is decomposed into a volumetric and a deviatoric part. The volumetric stress is computed using a Mie-Grüneisen equation of state. The deviatoric part of the stress is computed using a hypoelastic model in conjunction with a von Mises yield condition and a plasticity model. Hypoelastic materials are known not to conserve energy in a loading-unloading cycle. However, we justify our choice with the assumption that elastic strains are expected to be small for the problem under consideration and unlikely to affect the results significantly. A description of the stress update algorithm (Nemat-Nasser [65], Maudlin and Schiferl [61], Zocher et al. [101]) used in our calculations can be found Appendix B.

The effect of porosity on the yield surface is not discussed in this paper and neither is failure of the impact specimens. A discussion of these effects on the Taylor impact test will be presented in a future publication.

3 Models

One of the aims of our validation exercise has been to determine the plasticity model that is best suited for fire-container-explosive simulations. For the sake of completeness, we present below some of the strain-rate, strain, and temperature dependent models for metals that have been used in our simulations.

3.1 Equation of State

The hydrostatic pressure (p) is calculated using a temperature-corrected Mie-Grüneisen equation of state of the form used by Zocher et al. [101] (see also Wilkins [94], p.

61)

$$p = \frac{\rho_0 C_0^2 (\eta - 1)\left[\eta - \frac{\Gamma_0}{2}(\eta - 1)\right]}{\left[\eta - S_\alpha(\eta - 1)\right]^2} + \Gamma_0 E; \quad \eta = \frac{\rho}{\rho_0} \tag{1}$$

where C_0 is the bulk speed of sound, ρ_0 is the initial density, ρ is the current density, Γ_0 is the Grüneisen's gamma at reference state, $S_\alpha = dU_s/dU_p$ is a linear Hugoniot slope coefficient, U_s is the shock wave velocity, U_p is the particle velocity, and E is the internal energy per unit reference specific volume. The internal energy is computed using

$$E = \frac{1}{V_0}\int C_v dT \approx \frac{C_v(T - T_0)}{V_0} \tag{2}$$

where $V_0 = 1/\rho_0$ is the reference specific volume at temperature $T = T_0$, and C_v is the specific heat at constant volume.

3.2 Melting Temperature

We use a pressure dependent relation to determine the melting temperature (T_m). The Steinberg-Cochran-Guinan (SCG) melt model (Steinberg et al. [81]) has been used for our simulations of copper. This model is based on a modified Lindemann law and has the form

$$T_m(\rho) = T_{m0} \exp\left[2a\left(1 - \frac{1}{\eta}\right)\right] \eta^{2(\Gamma_0 - a - 1/3)}; \quad \eta = \frac{\rho}{\rho_0} \tag{3}$$

where T_{m0} is the melt temperature at $\eta = 1$, a is the coefficient of the first order volume correction to Grüneisen's gamma (Γ_0).

An alternative melting relation that is based on dislocation-mediated phase transitions - the Burakovsky-Preston-Silbar (BPS) model (Burakovsky et al. [22]) can also be used. This model has been used to determine the melt temperature for 4340 steel. The BPS model has the form

$$T_m(p) = T_m(0)\left[\frac{1}{\eta} + \frac{1}{\eta^{4/3}}\frac{\mu_0'}{\mu_0}p\right]; \quad \eta = \left(1 + \frac{K_0'}{K_0}p\right)^{1/K_0'} \tag{4}$$

$$T_m(0) = \frac{\kappa\lambda\mu_0\, v_{WS}}{8\pi \ln(z-1)\, k_b} \ln\left(\frac{\alpha^2}{4\, b^2 \rho_c(T_m)}\right) \tag{5}$$

where p is the pressure, $\eta = \rho/\rho_0$ is the compression, μ_0 is the shear modulus at room temperature and zero pressure, $\mu_0' = \partial\mu/\partial p$ is the derivative of the shear modulus at zero pressure, K_0 is the bulk modulus at room temperature and zero pressure, $K_0' = \partial K/\partial p$ is the derivative of the bulk modulus at zero pressure, κ is a constant, $\lambda = b^3/v_{WS}$ where b is the magnitude of the Burgers' vector, v_{WS} is the Wigner-Seitz volume, z is the coordination number, α is a constant, $\rho_c(T_m)$ is the critical density of dislocations, and k_b is the Boltzmann constant.

3.3 Shear Modulus

Three models for the shear modulus (μ) have been tested in our simulations. The first has been associated with the Mechanical Threshold Stress (MTS) model and we call it the MTS shear model. The second is the model used by Steinberg-Cochran-Guinan and we call it the SCG shear model while the third is a model developed by Nadal and Le Poac that we call the NP shear model.

3.3.1 MTS Shear Modulus Model

The simplest model is of the form suggested by Varshni [89] (Chen and Gray [25])

$$\mu(T) = \mu_0 - \frac{D}{exp(T_0/T) - 1} \tag{6}$$

where μ_0 is the shear modulus at 0K, and D, T_0 are material constants.

3.3.2 SCG Shear Modulus Model

The Steinberg-Cochran-Guinan (SCG) shear modulus model (Steinberg et al. [81], Zocher et al. [101]) is pressure dependent and has the form

$$\mu(p,T) = \mu_0 + \frac{\partial \mu}{\partial p}\frac{p}{\eta^{1/3}} + \frac{\partial \mu}{\partial T}(T - 300); \quad \eta = \rho/\rho_0 \tag{7}$$

where, μ_0 is the shear modulus at the reference state(T = 300 K, p = 0, η = 1), p is the pressure, and T is the temperature. When the temperature is above T_m, the shear modulus is instantaneously set to zero in this model.

3.3.3 NP Shear Modulus Model

A modified version of the SCG model has been developed by Nadal and Le Poac [64] that attempts to capture the sudden drop in the shear modulus close to the melting temperature in a smooth manner. The Nadal-LePoac (NP) shear modulus model has the form

$$\mu(p,T) = \frac{1}{\mathcal{J}(\hat{T})}\left[\left(\mu_0 + \frac{\partial \mu}{\partial p}\frac{p}{\eta^{1/3}}\right)(1-\hat{T}) + \frac{\rho}{Cm}\, k_b\, T\right]; \quad C := \frac{(6\pi^2)^{2/3}}{3} f^2 \tag{8}$$

where

$$\mathcal{J}(\hat{T}) := 1 + \exp\left[-\frac{1+1/\zeta}{1+\zeta/(1-\hat{T})}\right] \quad \text{for} \quad \hat{T} := \frac{T}{T_m} \in [0, 1+\zeta], \tag{9}$$

μ_0 is the shear modulus at 0 K and ambient pressure, ζ is a material parameter, k_b is the Boltzmann constant, m is the atomic mass, and f is the Lindemann constant.

3.4 Flow Stress

We have explored five temperature and strain rate dependent models that can be used to compute the flow stress:

(1) the Johnson-Cook (JC) model
(2) the Steinberg-Cochran-Guinan-Lund (SCG) model.
(3) the Zerilli-Armstrong (ZA) model.
(4) the Mechanical Threshold Stress (MTS) model.
(5) the Preston-Tonks-Wallace (PTW) model.

3.4.1 JC Flow Stress Model

The Johnson-Cook (JC) model (Johnson and Cook [49]) is purely empirical and gives the following relation for the flow stress (σ_y)

$$\sigma_y(\epsilon_p, \dot{\epsilon}_p, T) = [A + B(\epsilon_p)^n] \left[1 + C \ln(\dot{\epsilon}_p^*)\right] [1 - (T^*)^m] \tag{10}$$

where ϵ_p is the equivalent plastic strain, $\dot{\epsilon}_p$ is the plastic strain rate, A, B, C, n, m are material constants,

$$\dot{\epsilon}_p^* = \frac{\dot{\epsilon}_p}{\dot{\epsilon}_{p0}}; \quad T^* = \frac{(T - T_0)}{(T_m - T_0)}\,, \tag{11}$$

$\dot{\epsilon}_{p0}$ is a user defined plastic strain rate, T_0 is a reference temperature, and T_m is the melt temperature. For conditions where $T^* < 0$, we assume that $m = 1$.

3.4.2 SCG Flow Stress Model

The Steinberg-Cochran-Guinan-Lund (SCG) model is a semi-empirical model that was developed by Steinberg et al. [81] for high strain rate situations and extended to low strain rates and bcc materials by Steinberg and Lund [82]. The flow stress in this model is given by

$$\sigma_y(\epsilon_p, \dot{\epsilon}_p, T) = [\sigma_a f(\epsilon_p) + \sigma_t(\dot{\epsilon}_p, T)] \frac{\mu(p, T)}{\mu_0} \tag{12}$$

where σ_a is the athermal component of the flow stress, $f(\epsilon_p)$ is a function that represents strain hardening, σ_t is the thermally activated component of the flow stress,

$\mu(p,T)$ is the shear modulus, and μ_0 is the shear modulus at standard temperature and pressure. The strain hardening function has the form

$$f(\epsilon_p) = [1 + \beta(\epsilon_p + \epsilon_{pi})]^n; \quad \sigma_a f(\epsilon_p) \leq \sigma_{\max} \tag{13}$$

where β, n are work hardening parameters, and ϵ_{pi} is the initial equivalent plastic strain. The thermal component σ_t is computed using a bisection algorithm from the following equation (based on the work of Hoge and Mukherjee [46])

$$\dot{\epsilon}_p = \left[\frac{1}{C_1}\exp\left[\frac{2U_k}{k_b\,T}\left(1 - \frac{\sigma_t}{\sigma_p}\right)^2\right] + \frac{C_2}{\sigma_t}\right]^{-1}; \quad \sigma_t \leq \sigma_p \tag{14}$$

where $2U_k$ is the energy to form a kink-pair in a dislocation segment of length L_d, k_b is the Boltzmann constant, σ_p is the Peierls stress. The constants C_1, C_2 are given by the relations

$$C_1 := \frac{\rho_d L_d a b^2 \nu}{2w^2}; \quad C_2 := \frac{D}{\rho_d b^2} \tag{15}$$

where ρ_d is the dislocation density, L_d is the length of a dislocation segment, a is the distance between Peierls valleys, b is the magnitude of the Burgers' vector, ν is the Debye frequency, w is the width of a kink loop, and D is the drag coefficient.

3.4.3 ZA Flow Stress Model

The Zerilli-Armstrong (ZA) model (Zerilli and Armstrong [99, 100], Zerilli [98]) is based on simplified dislocation mechanics. The general form of the equation for the flow stress is

$$\sigma_y(\epsilon_p, \dot{\epsilon}_p, T) = \sigma_a + B\exp(-\beta(\dot{\epsilon}_p)T) + B_0\sqrt{\epsilon_p}\exp(-\alpha(\dot{\epsilon}_p)T) \tag{16}$$

where σ_a is the athermal component of the flow stress given by

$$\sigma_a := \sigma_g + \frac{k_h}{\sqrt{l}} + K\epsilon_p^n, \tag{17}$$

σ_g is the contribution due to solutes and initial dislocation density, k_h is the microstructural stress intensity, l is the average grain diameter, K is zero for fcc materials, B, B_0 are material constants. The functional forms of the exponents α and β are

$$\alpha = \alpha_0 - \alpha_1\ln(\dot{\epsilon}_p); \quad \beta = \beta_0 - \beta_1\ln(\dot{\epsilon}_p); \tag{18}$$

where $\alpha_0, \alpha_1, \beta_0, \beta_1$ are material parameters that depend on the type of material (fcc, bcc, hcp, alloys). The Zerilli-Armstrong model has been modified by Abed and Voyiadjis [1] for better performance at high temperatures. However, we have not used the modified equations in our computations.

3.4.4 MTS Flow Stress Model

The Mechanical Threshold Stress (MTS) model (Follansbee and Kocks [32], Goto et al. [35], Kocks [55]) gives the following form for the flow stress

$$\sigma_y(\epsilon_p, \dot{\epsilon}_p, T) = \sigma_a + (S_i\sigma_i + S_e\sigma_e)\frac{\mu(p,T)}{\mu_0} \tag{19}$$

where σ_a is the athermal component of mechanical threshold stress, μ_0 is the shear modulus at 0 K and ambient pressure, σ_i is the component of the flow stress due to intrinsic barriers to thermally activated dislocation motion and dislocation-dislocation interactions, σ_e is the component of the flow stress due to microstructural evolution with increasing deformation (strain hardening), (S_i, S_e) are temperature and strain rate dependent scaling factors. The scaling factors take the Arrhenius form

$$S_i = \left[1 - \left(\frac{k_b\, T}{g_{0i} b^3 \mu(p,T)} \ln\frac{\dot{\epsilon}_{p0i}}{\dot{\epsilon}_p}\right)^{1/q_i}\right]^{1/p_i} \tag{20}$$

$$S_e = \left[1 - \left(\frac{k_b\, T}{g_{0e} b^3 \mu(p,T)} \ln\frac{\dot{\epsilon}_{p0e}}{\dot{\epsilon}_p}\right)^{1/q_e}\right]^{1/p_e} \tag{21}$$

where k_b is the Boltzmann constant, b is the magnitude of the Burgers' vector, (g_{0i}, g_{0e}) are normalized activation energies, $(\dot{\epsilon}_{p0i}, \dot{\epsilon}_{p0e})$ are constant reference strain rates, and (q_i, p_i, q_e, p_e) are constants. The strain hardening component of the mechanical threshold stress (σ_e) is given by a modified Voce law

$$\frac{d\sigma_e}{d\epsilon_p} = \theta(\sigma_e) \tag{22}$$

where

$$\theta(\sigma_e) = \theta_0[1 - F(\sigma_e)] + \theta_{IV} F(\sigma_e) \tag{23}$$

$$\theta_0 = a_0 + a_1 \ln\dot{\epsilon}_p + a_2\sqrt{\dot{\epsilon}_p} - a_3 T \tag{24}$$

$$F(\sigma_e) = \frac{\tanh\left(\alpha\dfrac{\sigma_e}{\sigma_{es}}\right)}{\tanh(\alpha)} \tag{25}$$

$$\ln\left(\frac{\sigma_{es}}{\sigma_{0es}}\right) = \left(\frac{kT}{g_{0es} b^3 \mu(p,T)}\right) \ln\left(\frac{\dot{\epsilon}_p}{\dot{\epsilon}_{p0es}}\right) \tag{26}$$

and θ_0 is the hardening due to dislocation accumulation, θ_{IV} is the contribution due to stage-IV hardening, $(a_0, a_1, a_2, a_3, \alpha)$ are constants, σ_{es} is the stress at zero strain hardening rate, σ_{0es} is the saturation threshold stress for deformation at 0 K, g_{0es} is a constant, and $\dot{\epsilon}_{p0es}$ is the maximum strain rate. Note that the maximum strain rate is usually limited to about 10^7/s.

3.4.5 PTW Flow Stress Model

The Preston-Tonks-Wallace (PTW) model (Preston et al. [72]) attempts to provide a model for the flow stress for extreme strain rates (up to 10^{11}/s) and temperatures up to melt. The flow stress is given by

$$\sigma_y(\epsilon_p, \dot{\epsilon}_p, T) = \begin{cases} 2\left[\tau_s + \alpha \ln\left[1 - \varphi \exp\left(-\beta - \dfrac{\theta \epsilon_p}{\alpha\varphi}\right)\right]\right]\mu(p,T) & \text{thermal regime} \\ 2\tau_s \mu(p,T) & \text{shock regime} \end{cases} \tag{27}$$

with

$$\alpha := \frac{s_0 - \tau_y}{d}; \quad \beta := \frac{\tau_s - \tau_y}{\alpha}; \quad \varphi := \exp(\beta) - 1 \tag{28}$$

where τ_s is a normalized work-hardening saturation stress, s_0 is the value of τ_s at 0K, τ_y is a normalized yield stress, θ is the hardening constant in the Voce hardening law, and d is a dimensionless material parameter that modifies the Voce hardening law. The saturation stress and the yield stress are given by

$$\tau_s = \max\left\{ s_0 - (s_0 - s_\infty)\text{erf}\left[\kappa \hat{T} \ln\left(\frac{\gamma\dot{\xi}}{\dot{\epsilon}_p}\right)\right], s_0\left(\frac{\dot{\epsilon}_p}{\gamma\dot{\xi}}\right)^{s_1}\right\} \tag{29}$$

$$\tau_y = \max\left\{ y_0 - (y_0 - y_\infty)\text{erf}\left[\kappa \hat{T} \ln\left(\frac{\gamma\dot{\xi}}{\dot{\epsilon}_p}\right)\right], \min\left\{ y_1\left(\frac{\dot{\epsilon}_p}{\gamma\dot{\xi}}\right)^{y_2}, s_0\left(\frac{\dot{\epsilon}_p}{\gamma\dot{\xi}}\right)^{s_1}\right\}\right\} \tag{30}$$

where s_∞ is the value of τ_s close to the melt temperature, (y_0, y_∞) are the values of τ_y at 0K and close to melt, respectively, (κ, γ) are material constants, $\hat{T} = T/T_m$, (s_1, y_1, y_2) are material parameters for the high strain rate regime, and

$$\dot{\xi} = \frac{1}{2}\left(\frac{4\pi\rho}{3M}\right)^{1/3}\left(\frac{\mu(p,T)}{\rho}\right)^{1/2} \tag{31}$$

where ρ is the density, and M is the atomic mass.

3.5 Adiabatic Heating and Specific Heat

A part of the plastic work done is converted into heat and used to update the temperature of a particle. The increase in temperature (ΔT) due to an increment in plastic strain ($\Delta\epsilon_p$) is given by the equation

$$\Delta T = \frac{\chi \sigma_y}{\rho C_p}\Delta\epsilon_p \tag{32}$$

where χ is the Taylor-Quinney coefficient, and C_p is the specific heat. The value of the Taylor-Quinney coefficient is taken to be 0.9 in all our simulations (see

Ravichandran et al. [76] for more details on the variation of χ with strain and strain rate).

A relation for the dependence of C_p upon temperature is used for the steel (Lederman et al. [56]).

$$C_p = \begin{cases} A_1 + B_1\, t + C_1\, |t|^{-\alpha} & \text{if } T < T_c \\ A_2 + B_2\, t + C_2\, t^{-\alpha'} & \text{if } T > T_c \end{cases} \tag{33}$$

$$t = \frac{T}{T_c} - 1 \tag{34}$$

where T_c is the critical temperature at which the phase transformation from the α to the γ phase takes place, and $A_1, A_2, B_1, B_2, \alpha, \alpha'$ are constants.

The heat generated at a material point is conducted away at the end of a time step using the transient heat equation. The effect of conduction on material point temperature is negligible (but non-zero) for the high strain-rate problems simulated using Uintah.

4 MATERIALS

Though the primary metal of interest in the UINTAH simulations is 4340 steel, we discuss simulations of the deformation of three metals in this paper - high purity copper, 6061-T6 aluminum alloy, and 4340 steel alloy. The copper and aluminum alloy are face-centered cubic (fcc) materials while the 4340 steel alloy is body-centered cubic (bcc). The interstitials and solutes play a significant role in the plastic deformation of these alloys.

4.1 Copper

We have considered oxygen-free high conductivity (OFHC) copper and electrolytic tough pitch (ETP) copper - both under initial annealed conditions. Copper shows significant strain hardening, strain-rate sensitivity, and temperature dependence of plastic flow behavior. In addition, a large amount of experimental data is available for this material in the open literature. Hence it is invaluable for testing the accuracy of plasticity models and validating codes that simulate plasticity.

4.1.1 Specific heat of copper

The specific heat is used in the computation of the rate of increase of temperature due to plastic work (which feeds into the transient heat equation) and in the esti-

mation of the change in internal energy required by the Mie-Grüneisen equation of state. A constant specific heat (usually assumed to be 414 J/kg-K) is not appropriate at temperatures below 250 K and temperatures above 700 K, as can be seen from Figure 2.

A cubic curve was fit to the data for temperatures lower than 270 K. A linear curve was fit to the data for temperatures greater than 270 K. The specific heat predicted by the resulting model is shown by a solid line in Figure 2. The specific heat (C_p) versus temperature (T) model used in our copper simulations is given below. The units of C_p are J/kg-K.

$$C_p = \begin{cases} 0.0000416\,T^3 - 0.027\,T^2 + 6.21\,T - 142.6 & \text{for } T < 270\text{K} \\ 0.1009\,T + 358.4 & \text{for } T \geq 270\text{K} \end{cases} \tag{35}$$

4.1.2 Equation of state of copper

The Mie-Grüneisen equation of state is used to compute the volumetric part of the Cauchy stress tensor. The bulk speed of sound (C_0) and the slope of the linear fit to the Hugoniot (S_α) for copper have been obtained from Mitchell and Nellis [63]. The values of these parameters are 3933 m/s and 1.5, respectively. The value of the Grüneisen gamma (Γ_0) has been obtained from MacDonald and MacDonald [59]. We have chosen to use a value of 1.99 which is the value of Γ_0 at 100 K. An value of 2.12 can be used as an alternative for temperatures of 700 K and higher.

Figure 3 shows plots of the pressure predicted by the Mie-Grüneisen equation of state (continuous lines) at three different temperatures. The reference temperature

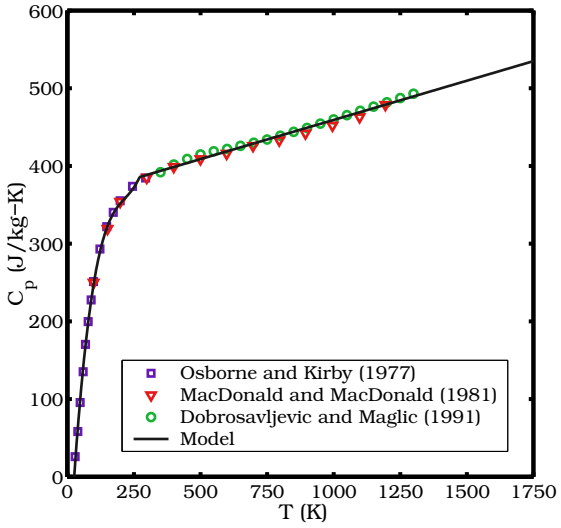

Fig. 2. Variation of the specific heat of copper with temperature. The solid line shows the values predicted by the model. Symbols show experimental data from Osborne and Kirby [69], MacDonald and MacDonald [59], and Dobrosavljevic and Maglic [30].

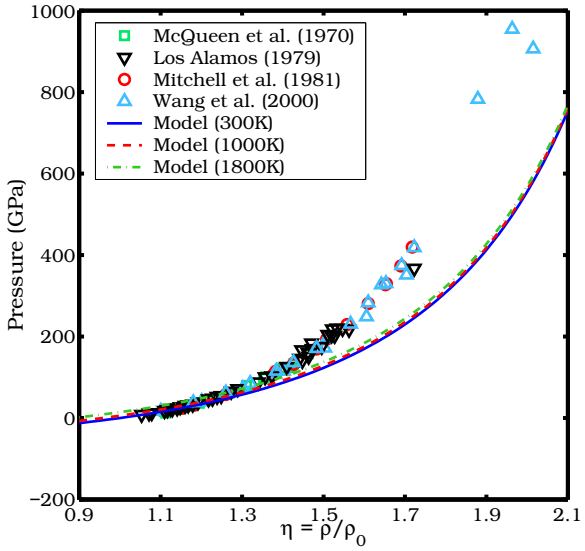

Fig. 3. The pressure predicted by the Mie-Grüneisen equation of state for copper as a function of density. The continuous lines show the values predicted by the model for three temperatures. The symbols show experimental data obtained from McQueen et al. [62], Marsh [60], Mitchell and Nellis [63], and Wang et al. [92]. The original sources of the experimental data can be found in the above citations.

for these calculations is 300 K. The predictions of the model are compared with pressures obtained from shock Hugoniot data. The model equation of state performs well for compressions less than 1.3 and the pressures are underestimated at higher compression. Since we do not achieve compressions greater than 1.2 in our simulations, the model that we have used is acceptable.

4.1.3 Melting temperature of copper

A melting temperature model is used to determine the pressure-dependent melting temperature of copper. The melting temperature is used to determine both the value of the shear modulus close to melting and as a flag which determines when a particle switches from solid to liquid state. Figure 4 shows a comparison of two melting temperature models - the Steinberg-Cochran-Guinan (SCG) model and the Burakovsky-Preston-Silbar (BPS) model. The melting curves predicted by the models are shown as continuous curves. Experimental data presented by Burakovsky et al. [22] are shown as open circles.

Table 1 shows the parameters used in the melting temperature models of copper. The parameter T_{m0} used in the SCG model has been obtained from Guinan and Steinberg [38]. The value of Γ_0 is from MacDonald and MacDonald [59] and the value of a has been chosen so as to fit the experimental data. The values of the initial bulk and shear moduli, and their derivatives that are used in the BPS model have been obtained from Guinan and Steinberg [38]. The remaining parameters for the BPS model are from Burakovsky and Preston [21] and Burakovsky et al. [23].

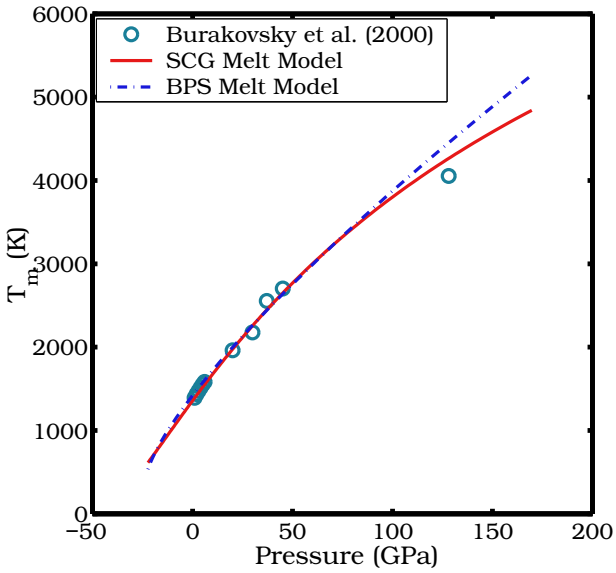

Fig. 4. The melting temperature of copper as a function of pressure. The lines show values predicted by the SCG and BPS models. The open circles show experimental data obtained from Burakovsky et al. [22]. The original sources of the experimental data can be found in the above citation.

An initial density ρ_0 of 8930 kg/m^3 has been used in the model calculations.

Both models predict the melting temperature quite accurately for pressures below 50 GPa. The SCG model appears to predict melting temperatures that are close to experimental values at higher pressures. However, the data at those pressures are sparse and should probably be augmented before conclusions regarding the models can be made. In any case, the pressures observed in our computations are usually less than 100 GPa and hence either of the models would suffice. We have chosen to use the SCG model for our copper simulations because the model is more computationally efficient.

Table 1
Parameters used in melting temperature models for 4340 steel.

Steinberg-Cochran-Guinan (SCG) model		
T_{m0} (K)	Γ_0	a
1356.5	1.99	1.5

Burakovsky-Preston-Silbar (BPS) model										
K_0 (GPa)	$K_0^{'}$	μ_0 (GPa)	$\mu_0^{'}$	κ	z	$b^2\rho_c(T_m)$	α	λ	v_{WS}	a (nm)
137	5.48	47.7	1.4	1.25	12	0.64	2.9	1.41	$a^3/4$	3.6147

4.1.4 Shear modulus of copper

The shear modulus of copper decreases with temperature and is also pressure-dependent. For high temperature simulations, using the room temperature value of shear modulus may lead to inaccuracies in radial return algorithms for elastic-plastic simulations. If the pressure-dependence of the shear modulus is neglected, modeling errors can accumulate for simulations involving shocks.

The shear modulus model that has been associated with the MTS plasticity model (Chen and Gray [25], Goto et al. [34]) is referred to as the MTS shear modulus model in this work. The shortcoming of this model is that it does not include any pressure-dependence of the shear modulus and is probably not applicable for high pressure applications.

The SCG shear modulus model has been used in conjunction with the SCG plasticity model and includes both temperature- and pressure-dependence. The NP shear modulus model is similar to the SCG model except for the temperature-dependent part and the smooth transition to zero shear modulus at melt. However, the SCG and NP shear modulus models do not reflect the flattening of the curve at low temperatures that is observed in experiments.

Figure 5(a) shows the shear modulus predicted by the MTS shear modulus model at zero hydrostatic pressure. The symbols show experimental data from Overton and Gaffney [70] and Nadal and Le Poac [64]. The parameters used in the model are given in Table 2. It can be seen that the model fits the low temperature data quite well. The shear moduli predicted by the SCG and NP shear models are shown in Figure 5(b) and Figure 5(c), respectively. The SCG shear model predicts slightly different moduli than the NP model at different values of compression. Both models fit the experimental data quite well except at very low temperatures (at which the MTS model performs best). We have not be able to validate the pressure dependence of the shear modulus at high temperatures due to lack of experimental data. An initial density of 8930 kg/m^3 has been used in the model calculations.

4.1.5 Yield stress of copper

In this section, we discuss the yield stresses of copper predicted by the five flow stress models for one-dimensional tension and compression tests. The high rate tests have been simulated with the explicit Material Point Method [84] and the stress update algorithm discussed in Appendix B. The quasistatic tests have been simulated with a fully implicit version of the Material Point Method (Guilkey and Weiss [37]) with an implicit stress update (Simo and Hughes [80]). Heat conduction is performed at all strain rates. However, as expected, we obtain nearly isothermal conditions quasistatic tests and nearly adiabatic conditions for high strain rate tests.

Experimental data for annealed OFHC copper from [66] (p. 241-242) and [72] are

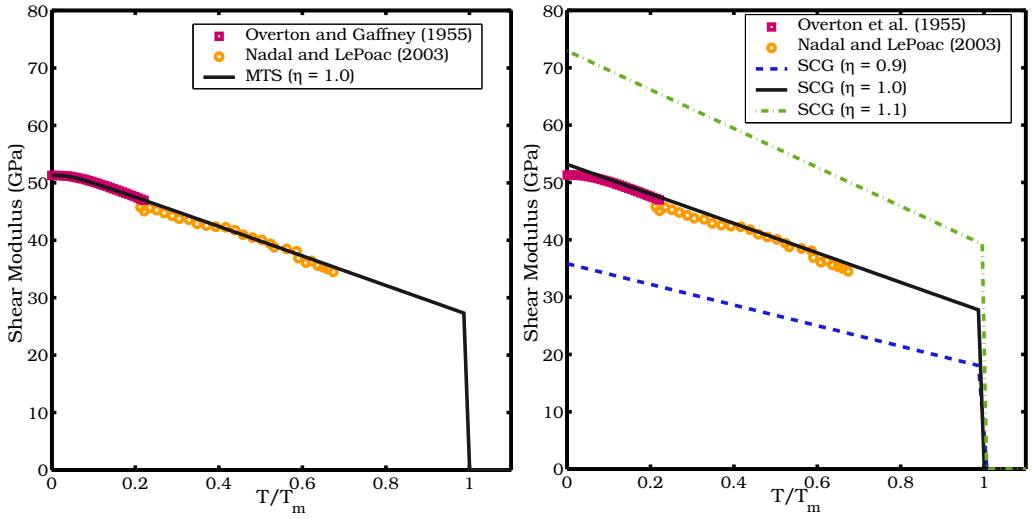

(a) MTS Shear Model

(b) SCG Shear Model

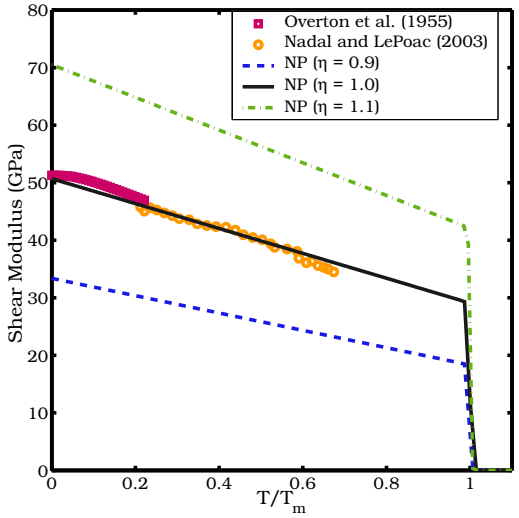

(c) NP Shear Model

Fig. 5. Shear modulus of copper as a function of temperature and pressure. The experimental data are from Overton and Gaffney [70] and Nadal and Le Poac [64]. The lines show values of the shear modulus at different compressions ($\eta = \rho/\rho_0$).

compared with the predicted values of yield stress. The data are presented in form of true stress versus true strain. Note that detailed verification has been performed to confirm the correct implementation of the models withing the UINTAH code. Also note that the high strain rate experimental data are suspect for strains less than 0.1. This is because the initial strain rate fluctuates substantially in Kolsky-Hopkinson bar experiments.

4.1.5.1 Johnson-Cook Model. For the one-dimensional simulations using the Johnson-Cook model, we use the following submodels: the Mie-Grüneisen equa-

Table 2
Parameters used in shear modulus models for copper.

MTS shear modulus model				
μ_0 (GPa)	D (GPa)	T_0 (K)		
51.3	3.0	165		
SCG shear modulus model				
μ_0 (GPa)	$\partial\mu/\partial p$	$\partial\mu/\partial T$ (GPa/K)		
47.7	1.3356	0.018126		
NP shear modulus model				
μ_0 (GPa)	$\partial\mu/\partial p$	ζ	C	m (amu)
50.7	1.3356	0.04	0.057	63.55

Table 3
Parameters used in the Johnson-Cook model for copper.

A (MPa)	B (MPa)	C	n	m	$\dot{\epsilon}_{p0}$ (/s)	T_0 (K)	T_m (K)
90	292	0.025	0.31	1.09	1.0	294	1356

tion of state, the specific heat model for copper, the Nadal-LePoac shear modulus model, and the Steinberg-Cochran-Guinan melting temperature model. The Johnson-Cook model is independent of pressure. Hence, the predicted yield stress is the same in compression and tension. The use of a variable specific heat model leads to a reduced yield stress at low temperature (77 K) for high strain rates. However, the effect is relatively small. At high temperatures, the effect of a high specific heat is to reduce the rate of increase of temperature with increase in plastic strain. This effect is also small. The temperature dependence of the shear modulus does not affect the yield stress. However, it has an effect on the plastic strain rate which is smaller than experimental error.

The solid lines in Figures 6(a) and (b) show predicted values of the yield stress for various strain rates and temperatures. The symbols show the experimental data. The Johnson-Cook model overestimates the initial yield stress for the quasistatic (0.1/s strain rate), room temperature (296 K), test. The rate of hardening is underestimated by the model for the room temperature test at 8000/s. The strain-rate dependence of the yield stress is underestimated at high temperature (see the data at 1173 K in Figure 6(a)). For the tests at a strain rate of 4000/s (Figure 6(b)), the yield stress is consistently underestimated by the Johnson-Cook model. The parameters used for the Johnson-Cook model are from Johnson and Cook [50]. These parameters are listed in Table 3.

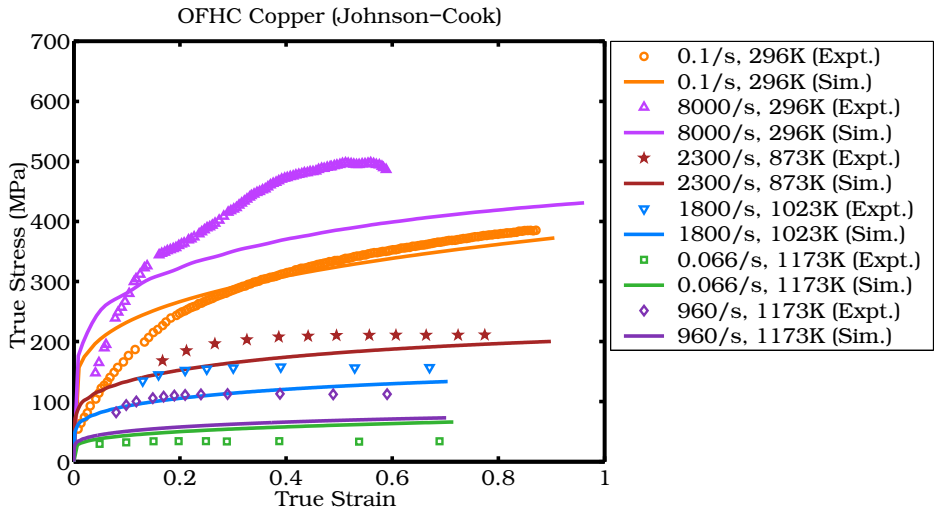

(a) Various strain rates.

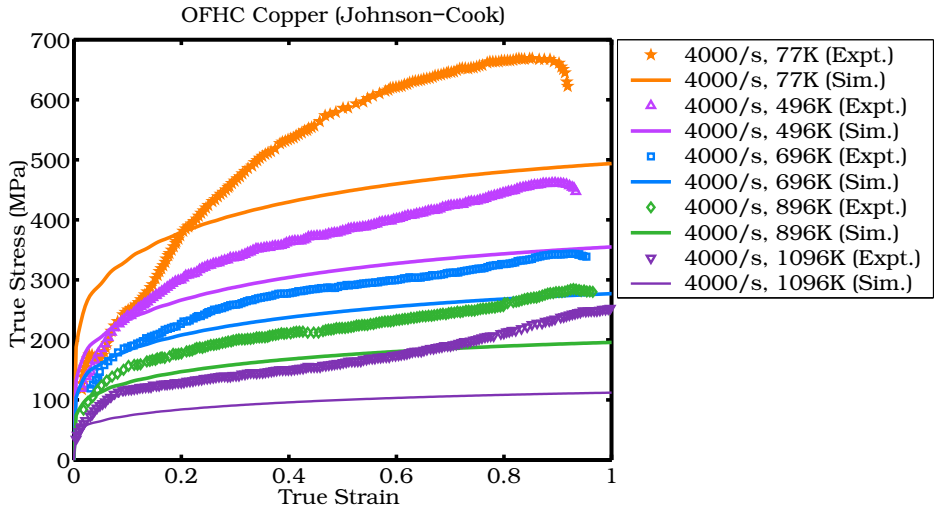

(b) Various temperatures.

Fig. 6. Predicted values of yield stress from the Johnson-Cook model. The experimental data at 873 K, 1023 K, and 1173 K are from Samanta [78] and represent compression tests. The remaining experimental data are from tension tests in Nemat-Nasser [66]. The solid lines are the predicted values.

4.1.5.2 Steinberg-Cochran-Guinan-Lund Model. We have used the Steinberg-Cochran-Guinan (SCG) shear modulus model for the one-dimensional simulations that use the Steinberg-Cochran-Guinan-Lund (SCGL) flow stress model. We could alternatively have used the Nadal-LePoac shear modulus model. However, we use the former to point out a problem with the assumption of the equivalence of the dependence on temperature of the shear modulus and the yield stress that is used by the SCGL flow stress model. The remaining models are the same as those used in conjunction with the Johnson-Cook flow stress model. A bisection algorithm is used to determine the thermally activated part of the flow stress for low strain rate conditions (less than 1000/s).

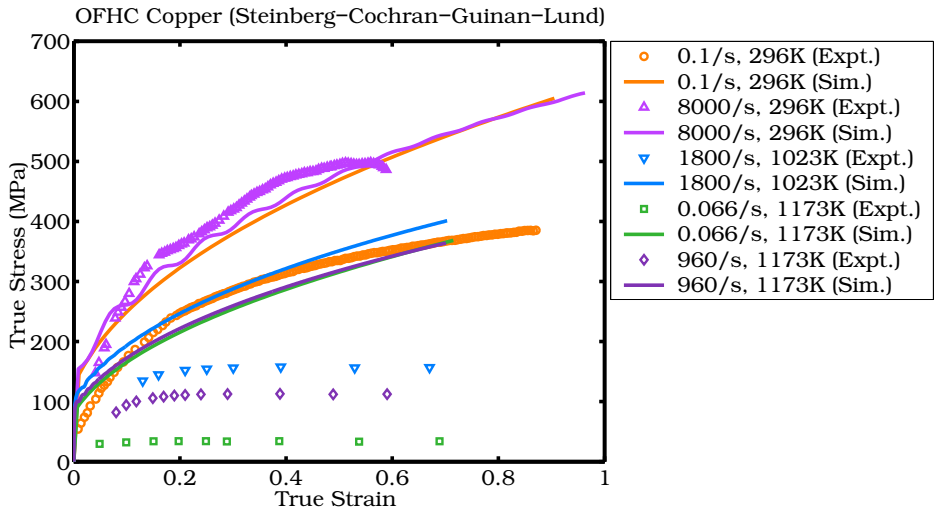

(a) Various strain rates.

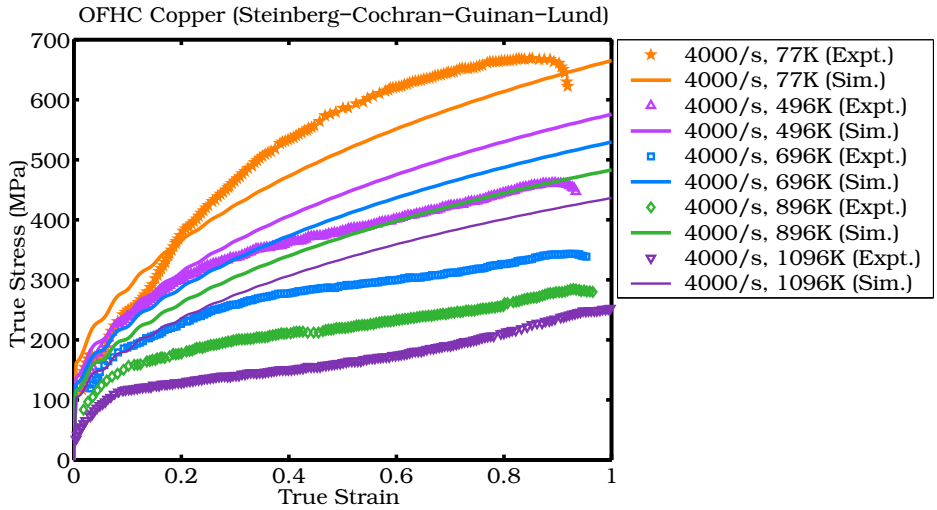

(b) Various temperatures.

Fig. 7. Predicted values of yield stress from the Steinberg-Cochran-Guinan-Lund model. Please see the caption of Figure 6 for the sources of the experimental data.

The solid lines in Figures 7(a) and (b) show the flow stresses predicted by the SCGL model. Clearly, the softening associated with increasing temperature is underestimated by the SCGL model. The parameters used in the SCGL model of OFHC copper are listed in Table 4.

Table 4
Parameters used in the Steinberg-Cochran-Guinan-Lund model for copper. The parameters for the athermal part of the SCGL model are from Steinberg et al. [81]. The parameters for the thermally activated part of the model are from a number of sources. The estimate for the Peierls stress is based on Hobart [45].

σ_a (MPa)	$\sigma_{\max}$ (MPa)	β	ϵ_{pi} (/s)	n	C_1 (/s)	U_k (eV)	σ_p (MPa)	C_2 (MPa-s)
125	640	36	0.0	0.45	0.71×10^6	0.31	20	0.012

As we see from Figure 7(a), at 296 K, the quasistatic yield stress is overestimated by around 50%; and the yield stress at 8000/s is predicted reasonably well. However, at 1023 K, the yield stress for 1800/s is overestimated by 70% at small strains to more than 150% at large strains. At 1173 K, the quasistatic yield stress is overestimated by 400% at small strains to 1000% at large strains. The high strain rate (960/s) yield stress is overestimated by 100% at small strains and by almost 200% at large strains.

For the tests at 4000/s shown in Figure 7(b), the SCGL modes performs progressive worse with increasing temperature. However, the errors are contained to around 100%.

Overall, at low temperatures, the high strain rate predictions from the SCGL model match the experimental data best. This is not surprising since the original model by Steinberg et al. [81] (SCG) was rate independent and designed for high strain rate applications. However, the low strain rate extension by Steinberg and Lund [82] does not lead to good predictions of the yield stress of OFHC copper at low temperatures.

The high temperature response of the SCGL model is dominated by the shear modulus model; in particular, the derivative of the shear modulus with respect to temperature. From Figure 5(b) we can see that a value of -0.018126 GPa/K for $\partial\mu/\partial T$ matches the experimental data quite well. Steinberg et al. [81] assume that the values of $(\partial\sigma_y/\partial T)/\sigma_{y0}$ and $(\partial\mu/\partial T)/\mu_0$ (-3.8$\times$10-4 /K) are comparable. That does not appear to be the case for OFHC copper.

If we extract the yield stresses at a strain of 0.2 from the experimental data shown in Figure 7(b), we get the following values of temperature and yield stress for a strain rate of 4000/s: (77 K, 380 MPa); (496 K, 300 MPa); (696 K, 230 MPa); (896 K, 180 MPa); (1096 K, 130 MPa). A straight line fit to the data shows that the value of $\partial\sigma_y/\partial T$ is -0.25 MPa/K. The yield stress at 300 K can be calculated from the fit to be approximately 330 MPa. This gives a value of -7.6$\times$10$^{-}4$ /K for $(\partial\sigma_y/\partial T)/\sigma_{y0}$; approximately double the slope of the shear modulus versus temperature curve. Hence, a shear modulus derived from a shear modulus model cannot be used as a multiplier to the yield stress in equation (12). Instead, the original form of the SCG model (Steinberg et al. [81]) must be used, with the term $(\partial\mu/\partial T)/\mu_0$ replaced by $(\partial\sigma_y/\partial T)/\sigma_{y0}$ in the expression for yield stress.

Figures 8(a) and (b) show the predicted yield stresses from the modified SCGL model. These plots show that there is a considerable improvement in the prediction of the temperature dependence of yield stress if the value of $(\partial\sigma_y/\partial T)/\sigma_{y0}$ is used instead of $(\partial\mu/\partial T)/\mu_0$. However, the strain rate dependence of OFHC copper continues to be poorly modeled by the SCGL model.

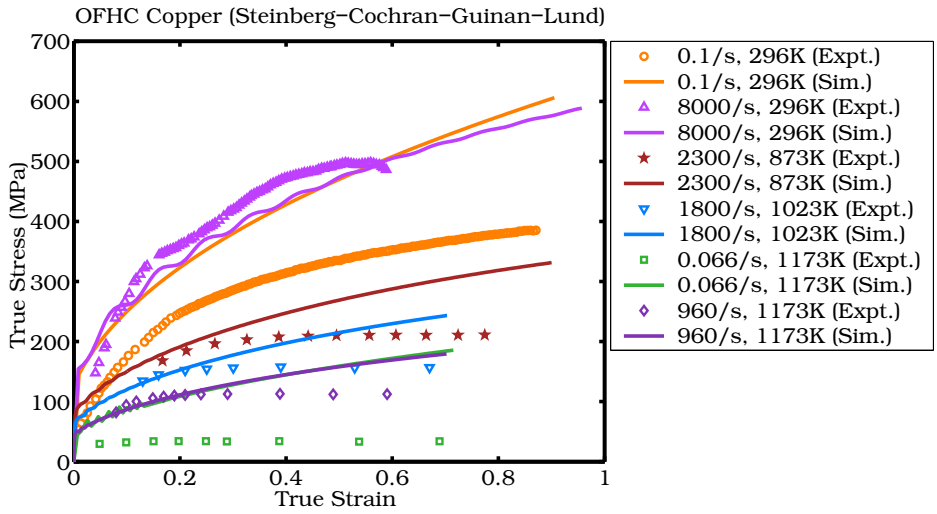

(a) Various strain rates.

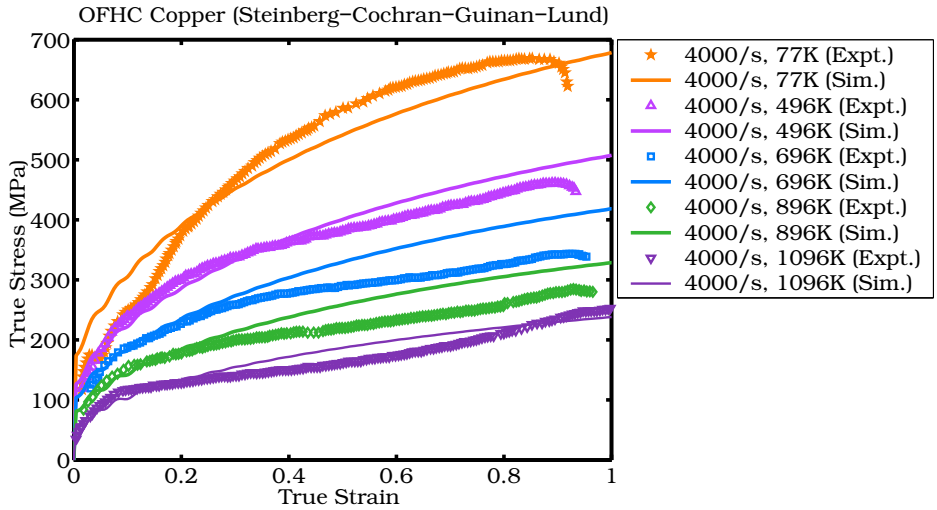

(b) Various temperatures.

Fig. 8. Predicted values of yield stress from the modified Steinberg-Cochran-Guinan-Lund model. Please see the caption of Figure 6 for the sources of the experimental data.

4.1.5.3 Zerilli-Armstrong Model. In contrast to the Johnson-Cook and the Steinberg-Cochran-Guinan models, the Zerilli-Armstrong (ZA) model for yield stress is based on dislocation mechanics and hence has some physical basis. We have used the Nadal-LePoac shear modulus model in conjunction with our simulations that use the ZA flow stress model.

Figures 9(a) and (b) show the yield stresses predicted by the ZA model. As in the previous sections, the symbols in the plots represent experimental data while the solid lines represented the computed stress-strain curves. The parameters used for the Zerilli-Armstrong model have been obtained from Zerilli and Armstrong [99] and are listed in Table 5.

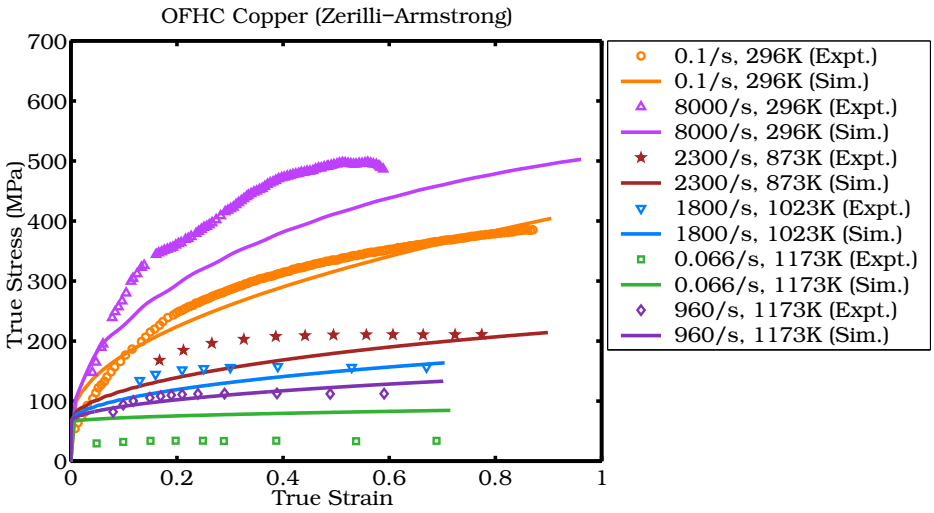

(a) Various strain rates.

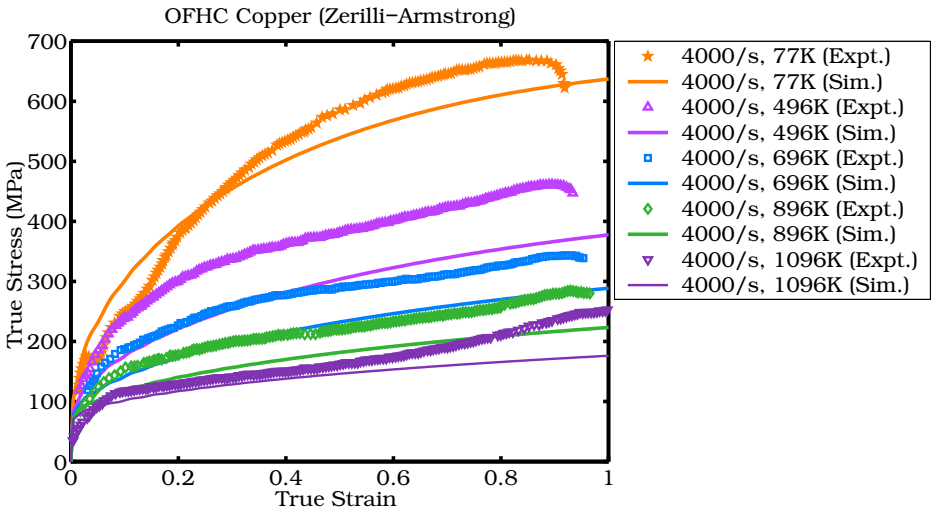

(b) Various temperatures.

Fig. 9. Predicted values of yield stress from the Zerilli-Armstrong model. Please see the caption of Figure 6 for the sources of the experimental data.

Table 5
Parameters used in the Zerilli-Armstrong model for copper (Zerilli and Armstrong [99]).

σ_g (MPa)	k_h (MPa-mm$^{1/2}$)	l (mm)	K (MPa)	n	
46.5	5.0	0.073	0.0	0.5	
B (MPa)	β_0 (/K)	β_1 (s/K)	B_0 (MPa)	α_0 (/K)	α_1 (s/K)
0.0	0.0	0.0	890	0.0028	0.000115

From Figure 9(a), we can see that the ZA model predicts the quasistatic, room temperature yield stress quite accurately. However, the room temperature yield stress at 8000/s is underestimated. The initial yield stress is overestimated at high temperatures; as are the saturation stresses.

Stress-strain curves at 4000/s are shown in Figure 9(b). In this case, the ZA model predicts reasonable initial yield stresses. However, the decrease in yield stress with increasing temperature is overestimated. We notice that the predicted yield stress at 496 K overlaps the experimental data for 696 K, while the predicted stress at 696 K overlaps the experimental data at 896 K.

4.1.5.4 Mechanical Threshold Stress Model. The Mechanical Threshold Stress (MTS) model is different from the three previous models in that the internal variable that evolves in time is a stress (σ_e). The value of the internal variable is calculated for each value of plastic strain by integrating equation (22) along a constant temperature and strain rate path. A unconditionally stable and second-order accurate midpoint integration scheme has been used to determine the value of σ_e. Alternatively, an incremental update of the internal variable could be done using quantities from the previous timestep. The integration of the evolution equation is no longer along a constant temperature and strain rate path in that case. We have found that two alternatives give us similar values of σ_e in the simulations that we have performed. The incremental update of the value of σ_e is considerably faster than the full update along a constant temperature and strain rate path.

We have used the pressure-independent MTS shear modulus model in the simulations that use the MTS flow stress model. The reason for this choice is that the parameters of the model have been fit with such a shear modulus model. If the shear modulus model is changed, certain parameters of the model will have to be changed to reflect the difference. The SCG melting temperature model, the variable specific heat model, and the Mie-Grüneisen equation of state for copper have been used; as has been done with the previous models.

Figures 10(a) and (b) show the experimental values of yield stress for OFHC copper versus those computed with the MTS model. The solid lines show the computed stresses. The symbols represent the experimental data. The parameters used in the MTS model have been obtained from Follansbee and Kocks [32] and are shown in Table 6.

From Figure 10(a), we can see that the yield stress predicted by the MTS model almost exactly matches the experimental data at 296 K for a strain rate of 0.1/s. The yield stress for the test conducted at 296 K and at 8000/s is underestimated by the MTS model. The MTS model predicts reasonably good values of yield stress for the test at 1023 K and 1800/s. However, saturation appears earlier in the experimental stress-strain curve than predicted by the MTS model. The same is true for the test

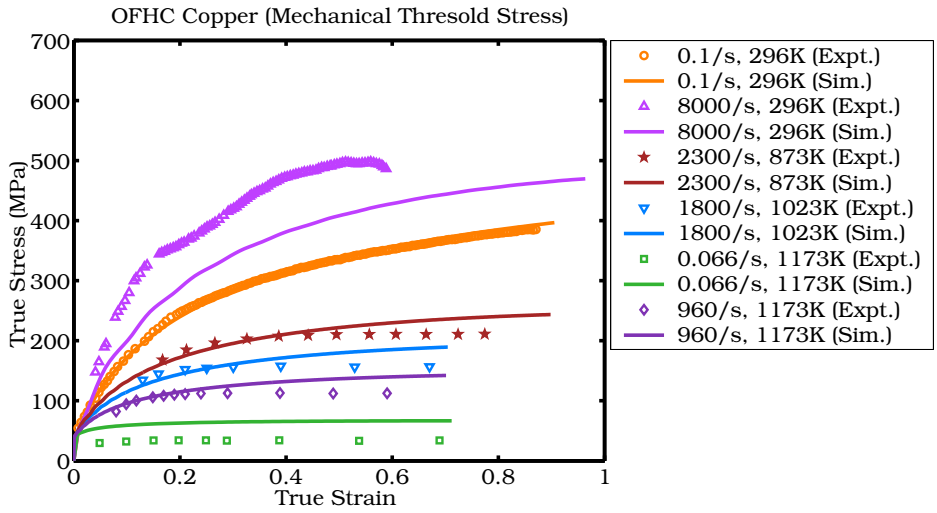

(a) Various strain rates.

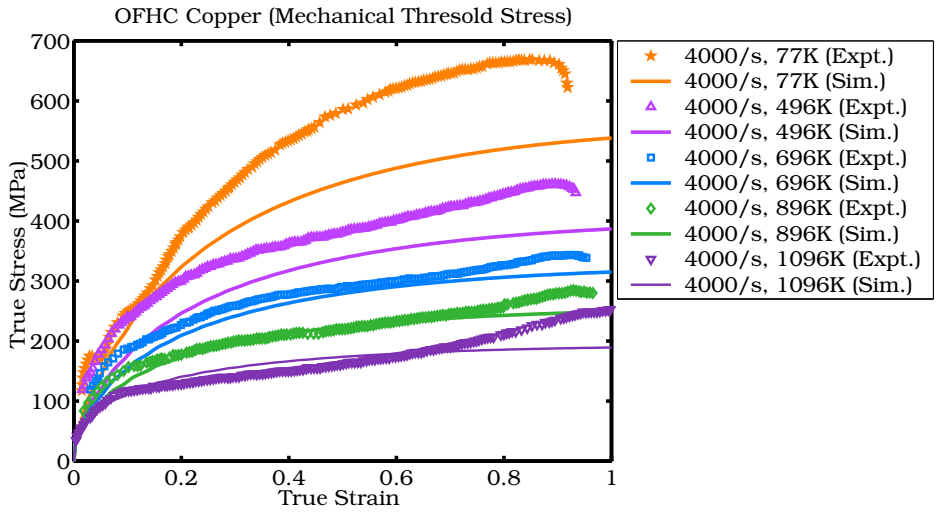

(b) Various temperatures.

Fig. 10. Predicted values of yield stress from the Mechanical Threshold Stress model. Please see the caption of Figure 6 for the sources of the experimental data.

Table 6
Parameters used in the Mechanical Threshold Stress model for copper (Follansbee and Kocks [32]).

σ_a (MPa)	b (nm)	σ_i (MPa)	g_{0i}	$\dot{\epsilon}_{p0i}$ (/s)	p_i	q_i
40	0.256	0	1	1	1	1
g_{0e}	$\dot{\epsilon}_{p0e}$ (/s)	p_e	q_e	σ_{0es} (MPa)	g_{0es}	$\dot{\epsilon}_{p0es}$ (/s)
1.6	1.0×10^7	2/3	1	770	0.2625	1.0×10^7
α	a_0 (MPa)	a_1 (MPa-log(s))	a_2 (MPa-s$^{1/2}$)	a_3 (MPa/K)	θ_{IV} (MPa)	
2	2390	12	1.696	0	0	

at 873 at 2300 /s. The yield stress predicted by the MTS model for the quasistatic test at 1173 K is is higher than that observed experimentally. However, the higher rate test at the same temperature matches the experiments quite well except for a higher amount of strain hardening at large strains.

The variation of yield stress with temperature at a strain rate of 4000/s is shown in Figure 10(b). From the figure, we can see that the yield stress is underestimated by the MTS model at 77K. However, the predictions improve with increase in temperature. The MTS model predicts the yield stress quite accurately at 696K, 896 K, and 1096 K. From the experimental data we can observe a certain amount of stage III or stage IV hardening. This effect is not captured by the MTS model; probably because of early saturation of the amount of hardening.

4.1.5.5 Preston-Tonks-Wallace Model. The Preston-Tonks-Wallace (PTW) model attempts to provide a single approach to model both thermally activated glide and overdriven shock regimes. The overdriven shock regime includes strain rates greater than 10^7. The PTW model, therefore, extends the possibility of modeling plasticity beyond the range of validity of the MTS model. We have not conducted a simulations of overdriven shocks in this paper. However, the PTW model explicitly accounts for the rapid increase in yield stress at strain rates above 1000 /s. Hence the model is a good candidate for the range of strain rates and temperatures of interest to us. We use the Nadal-LePoac shear modulus model in all simulations involving the PTW yield stress model.

Experimental yield stresses and those predicted by the PTW model are shown in Figures 11(a) and (b). The solid lines in the figure are the predicted values while the symbols represent experimental data. The model parameters used in the simulations are shown in Table 7.

From Figure 11(a) we can see that the predicted yield stress at 0.1/s and 296 K matches the experimental data quite well. The error in the predicted yield stress at 296 K and 8000/s is also smaller than that for the MTS flow stress model. The experimental data at 873 K, 1023 K, and 1173 K are were used by Preston et al. [72] to fit the model parameters. Hence it is not surprising that the predicted yield stresses match the experimental data better than any other model.

The temperature dependent yield stresses at 4000/s are shown in Figure 11(b). In this case, the predicted values at 77 K are lower than the experimental values. However, for higher temperatures, the predicted values match the experimental data quite well for strains less than 0.4. At higher strains, the predicted yield stress saturates while the experimental data continues to show a significant amount of hardening. The PTW model predicts better values of yield stress for the compression tests while the MTS model performs better for the tension tests.

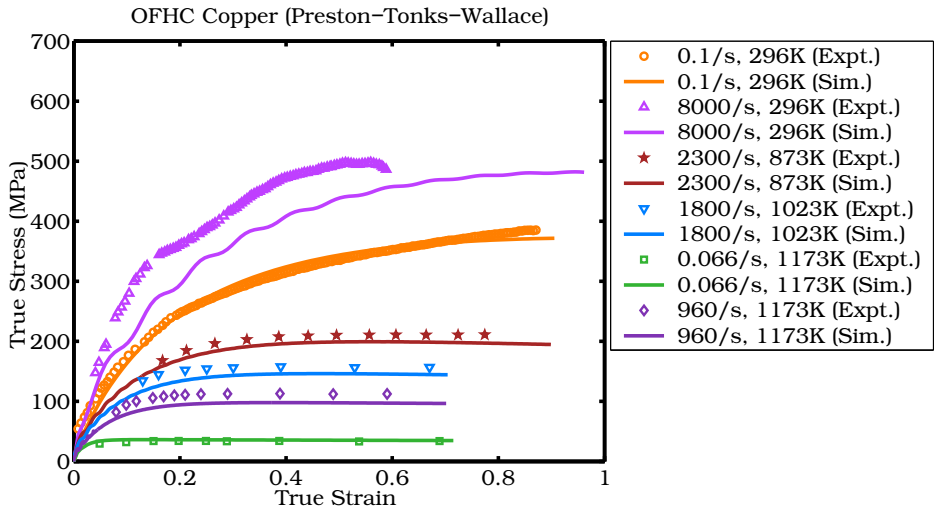

(a) Various strain rates.

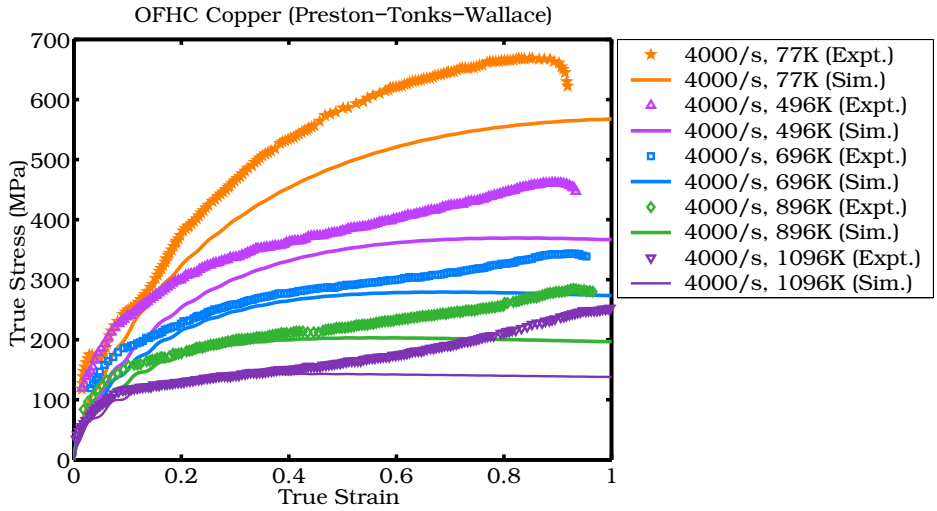

(b) Various temperatures.

Fig. 11. Predicted values of yield stress from the Preston-Tonks-Wallace model. Please see the caption of Figure 6 for the sources of the experimental data.

Table 7
Parameters used in the Preston-Tonks-Wallace yield stress model for copper (Preston et al. [72]).

s_0	s_∞	y_0	y_∞	d	κ	γ	θ
0.0085	0.00055	0.0001	0.0001	2	0.11	0.00001	0.025
M (amu)	s_1	y_1	y_2				
63.546	0.25	0.094	0.575				

4.1.5.6 Comparisons between the various flow stress models. In this section, we use the difference between the predicted and the experimental values of the flow stress as a metric to compare the various flow stress models. First, we show the difference between the predicted and the experimental values of yield stress in the form of plots of error in true stress versus true strain. The error in the true strain is calculated as shown in equation 36.

$$\text{Error}_{\sigma} = \left(\frac{\sigma_{\text{predicted}}}{\sigma_{\text{expt.}}} - 1 \right) \times 100 \tag{36}$$

Figures 12(a) and (b) show the percentage difference between the values of yield stress predicted by the Johnson-Cook model and the experimental data. If we ignore the high strain rate data for strains less than 0.1, it is observed that the difference between the predicted and the experimental values is around 20% to 50% (with the largest errors at high temperatures). The quasistatic, room-temperature prediction shows large errors at low strains. However, at larger strains, the quasistatic predictions are within 5% of experiment. The errors in the predicted values for the test at 0.066 /s and 1173 K are quite large (almost 100% at large strains). This indicates that the Johnson-Cook model severely overestimates yield stresses low strain rates and high temperatures. A recalibration of the model parameters is needed before it can be used to simulate such conditions.

Differences between the predicted and the experimental values for the Steinberg-Cochran-Guinan-Lund model are shown in Figures 12(c) and (d). The best fit to the experimental data is obtained for a strain rate of 8000 /s at room temperature. The quasistatic test at the same temperature overestimates the yield stress by 50%. The error in the predicted value of yield stress at 1173 K and 960 /s is small at a strain of 0.2 and increases to 50% at a strain of 0.6. In comparison, the quasistatic yield stress at that temperature is overestimated by 150% to 450%. Clearly, the SCGL model is not appropriate (even with the modification by Steinberg and Lund) for quasistatic problems. The high strain rate (4000 /s) predictions are considerably better and the error varies from 10% to 20%.

The Zerilli-Armstrong model errors are shown in Figures 12(e) and (f). In this case, the room temperature, quasistatic, predicted yield stresses are within 10% of the experimental values. The high temperature, quasistatic, yield stresses are however quite different from the experimental values - 120% to 160%. The room temperature, high strain rate, predictions differ by 10% to 20% from experiment. Similar ranges of errors are observed for the high temperature data at various strain rates. An average error of around 20% is observed for the tests conducted at 4000/s.

Figures 13(a) and (b) show the errors in the yield stresses predicted by the Mechanical Threshold Stress model. At room temperature and quasistatic conditions, the error in the yield stress predicted by the MTS model is close to zero. The quasistatic, high temperature, yield stress is overestimated by around 100%. The high

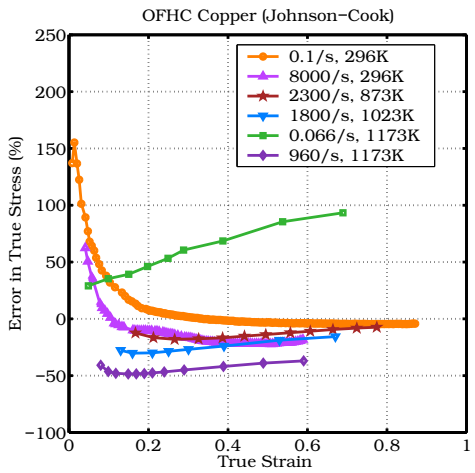

(a) Various strain rates.

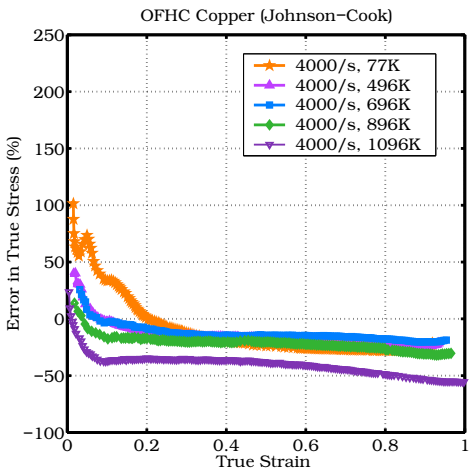

(b) Various temperatures.

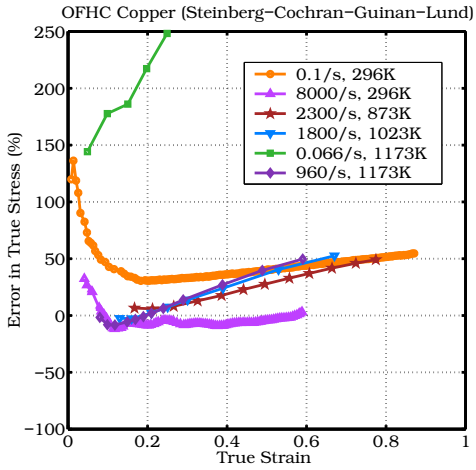

(c) Various strain rates.

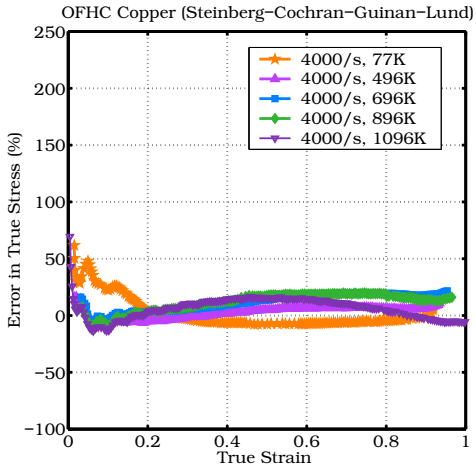

(d) Various temperatures.

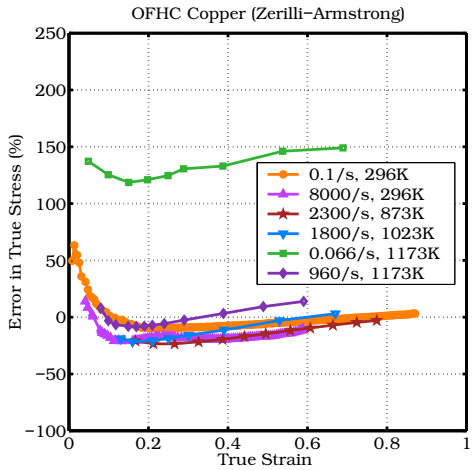

(e) Various strain rates.

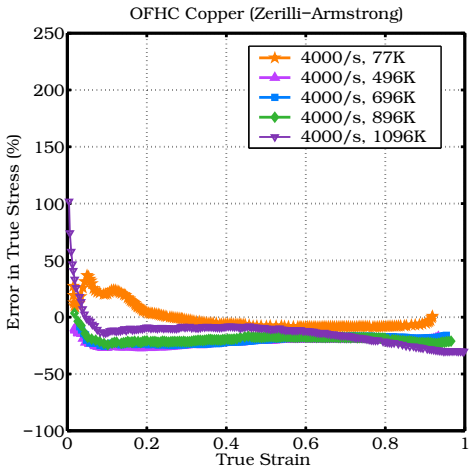

(f) Various temperatures.

Fig. 12. Difference between the predicted values of yield stress and the experimental data as a percentage of the experimental values for the Johnson-Cook, Steinberg-Cochran-Guinan-Lund, and Zerilli-Armstrong models.

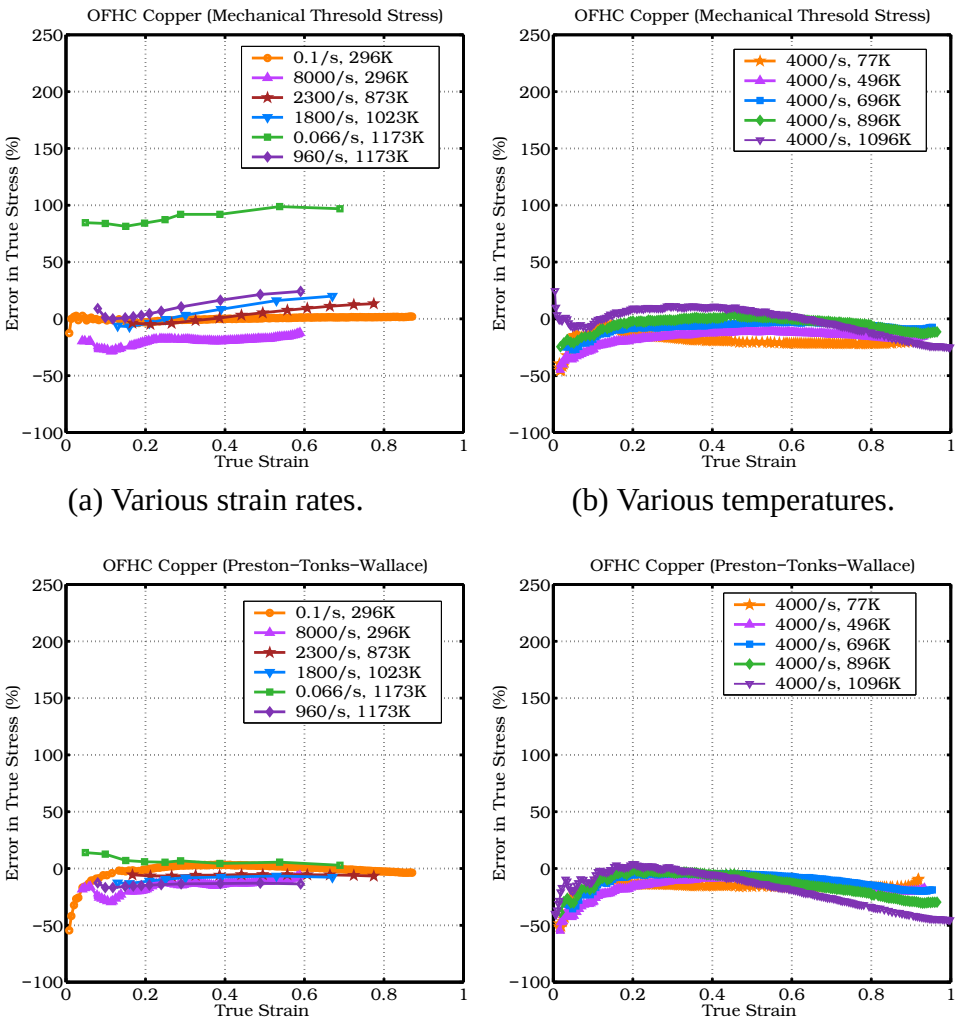

(a) Various strain rates. (b) Various temperatures.

(c) Various strain rates. (d) Various temperatures.

Fig. 13. Difference between the predicted values of yield stress and the experimental data as a percentage of the experimental values for the Mechanical Threshold Stress and Preston-Tonks-Wallace models.

strain rate yield stress at 296 K is underestimated by around 20%. For the high temperature compression tests at 960 /s, 1800 /s, and 2300 /s, the error in the predicted values is around 5% at small strains and increases to about 20% at large strains. The error in the predicted stresses for a strain rate of 4000/s and various temperatures varies between 5% to 20%.

The Preston-Tonks-Wallace predicts the yield stresses for the quasistatic and the compression tests the best, with errors ranging between 1% to 10% (see Figure 13(c)). For the tension tests at 4000 /s (Figure 13(d)), the average error is around 15% for strains less than 0.5. For larger strains, the error increases because of premature saturation of the yield stress.

To quantify these errors and as an aid in determining the best model for the range

of conditions under consideration, we have listed some error statistics in Tables 8 and 9. Only true strains greater than 0.1 have been considered in the generation of these statistics.

The statistics in Tables 8 and 9 show that none of the models consistently performs better than the other models. To simplify these statistics, we can consider as a metric the absolute mean error plus one standard deviation of the error. A comparison of this "maximum" absolute error metric for various sets of conditions might allow for a better quantification of the range of applicability of each model. Some such comparisons are shown in Table 10. The quantities shown in the table are the average of the "maximum" absolute (MA) errors for the set of tests that satisfy the conditions listed in the table.

From Table 10 we observe that the least average MA error for all the tests is 17% while the greatest average MA error is 64%. The PTW model performs best while the SCGL model performs worst. In order of increasing error, the models may be arranged as PTW, MTS, ZA, JC, and SCGL. Considering only the tension tests, the MTS model performs best with an average MA error of 14%. The Johnson-Cook model does the worst at 25% error. For the compression tests, the PTW model does best with an error of 10% compared to the next best, the MTS model with a 35% error. The SCGL error shows an average MA error of 126% for these tests. For the high strain rate tests, the MTS model performs better than the PTW model with an average MA error of 15% (compared to 18% for PTW). The low strain rate tests are predicted best by the PTW model (5 %) and worst by the SCGL model (219 %). Note that this average error is based on two tests at 296 K and 1173 K and may not be representative for intermediate temperatures. The PTW model shows an average MA error of 16% for the high temperature tests compared to 27% for the MTS model. The SCGL model again performs the worst. Finally, the low temperature tests ($<$ 800 K) are predicted best by the PTW model. The other models also perform reasonably well under these conditions.

From the above comparisons, the Preston-Tonks-Wallace and the Mechanical Threshold Stress models clearly stand out as the ones that are reasonably accurate over a large range of strain rates and temperatures. A caveat regarding such a conclusion that the parameters of the models can be changed to give a better fit to the experimental data that we have used for our comparisons. However, it is more likely that an user of such models in computational codes will use parameters that are already available in the literature. The implicit assumption is that published parameters provide the best possible fit to experimental data. Our aim here has been to compare the models under a specific condition - where the parameters are known and unchanged. Of course, better statistics can be generated if the number of one-dimensional tests is increased. Instead, to further quantify the range of applicability of the models, we perform a similar comparison with Taylor impact test data.

Table 8
Comparison of the error in the yield stress predicted by the five flow stress models at various strain rates and temperatures.

Temp. (K)	Strain Rate (/s)	Error	JC (%)	SCGL (%)	ZA (%)	MTS (%)	PTW (%)
296	0.1	Max.	32	55	3	2	3
		Min.	-4	31	-10	-4	-6
		Mean	0.2	41	-4	0.2	0.5
		Median	-3	41	-5	0.6	1.1
		Std. Dev.	6	7	4	1.3	2.3
296	8000	Max.	1.1	3	-10	-12	-6
		Min.	-22	-12	-21	-29	-29
		Mean	-17	-6	-17	-19	-14
		Median	-20	-7	-18	-18	-13
		Std. Dev.	6	3	2	3	4
873	2300	Max.	-7	49	-3	13	-5
		Min.	-18	6	-24	-5	-7
		Mean	-13	26	-15	4	-6
		Median	-13	25	-16	4	-6
		Std. Dev.	4	16	7	7	0.5
1023	1800	Max.	-16	53	3	20	-7
		Min.	-30	-3	-22	-7	-13
		Mean	-25	17	-13	4	-10
		Median	-27	11	-17	1.5	-9
		Std. Dev.	5	21	9	10	2
1173	0.066	Max.	93	440	149	99	7
		Min.	39	186	119	81	3
		Mean	64	297	132	90	5
		Median	61	275	131	92	6
		Std. Dev.	20	93	12	6	1.4
1173	960	Max.	-37	50	14	24	-13
		Min.	-49	-8	-8	-0.1	-17
		Mean	-45	12	-2	9	-15
		Median	-47	4	-6	6	-14
		Std. Dev.	4	20	8	9	1

Table 9
Comparison of the error in the yield stress predicted by the five flow stress models for a strain rate of 4000/s.

Temp. (K)	Strain Rate (/s)	Error	JC (%)	SCGL (%)	ZA (%)	MTS (%)	PTW (%)
77	4000	Max.	34	26	24	-5	-8
		Min.	-28	-8	-9	-22	-17
		Mean	-14	-8	-2	-18	-15
		Median	-21	-4	-6	-19	-15
		Std. Dev.	16	9	9	5	2
496	4000	Max.	-2	11	-17	-11	-8
		Min.	-24	-7	-27	-26	-29
		Mean	-17	3	-22	-15	-14
		Median	-17	5	-21	-14	-13
		Std. Dev.	5	5	3	3	5
696	4000	Max.	-2	22	-16	-3	-4
		Min.	-20	-2	-25	-16	-20
		Mean	-14	13	-20	-6	-9
		Median	-15	15	-19	-6	-7
		Std. Dev.	4	7	3	3	5
896	4000	Max.	-16	20	-17	3	-2
		Min.	-32	-9	-24	-15	-30
		Mean	-23	13	-20	-3	-13
		Median	-21	16	-20	-2	-11
		Std. Dev.	4	7	2	5	9
1096	4000	Max.	-35	17	-8	12	4
		Min.	-56	-13	-30	-25	-45
		Mean	-42	7	-15	-1.4	-18
		Median	-39	9	-12	3	-15
		Std. Dev.	7	8	7	12	16

4.2 Aluminum Alloy

The aluminum alloy 6061-T6 is relatively strain-rate insensitive and strain hardening is small. The yield stress is quite sensitive to temperature and hence this material

Table 10
Comparison of average "maximum" absolute (MA) errors in yield stresses predicted by the five flow stress models for various conditions.

Condition	Average MA Error (%)				
	JC	SCGL	ZA	MTS	PTW
All Tests	36	64	33	23	17
Tension Tests	25	20	19	14	18
Compression Tests	45	126	50	35	10
High Strain Rate ($\geq$ 100 /s)	29	22	20	15	18
Low Strain Rate ($<$ 100 /s)	45	219	76	49	5
High Temperature ($\geq$ 800 K)	43	90	40	27	16
Low Temperature ($<$ 800 K)	20	20	17	15	14

provides an excellent tool for validating temperature effects in plasticity models. A large set of experiments at high rates have been performed on this material - particularly flyer plate experiments. However, under shock loading conditions both 6061-T6 and OFHC copper show a dramatic increase in the strain rate dependence of yield stress (Lesuer et al. [57], Preston et al. [72]).

Details of the validation of the models for 6061-T6 aluminum alloy can be found in Bhawalkar [19].

4.3 Steel

The high-strength low-alloy (HSLA) 4340 steel is a material of interest in the UINTAH simulations. The yield stress of this material can vary dramatically depending on the heat treatment that it has undergone. Hence, purely empirical plasticity models require to be recalibrated for different levels of hardness of this material. However, we have assumed a constant hardness (Rockwell C 30 - 40) for all the simulations in this work.

4.3.1 Melting Temperature Model for 4340 Steel

Figure 14 shows a comparison of the predictions from the SCG (Equation 3) and BPS (Equation 4) models with experimental data for iron from Burakovsky et al. [22] (includes data from Williams et al. [96] and Yoo et al. [97]). The BPS model performs better at high pressures, but both models are within experimental variability below 100 GPa. The parameters used in the models are shown in Table 11. The bulk and shear moduli and their derivatives for iron have been obtained from Guinan and Steinberg [38]. The parameters for the BPS model at zero pressure

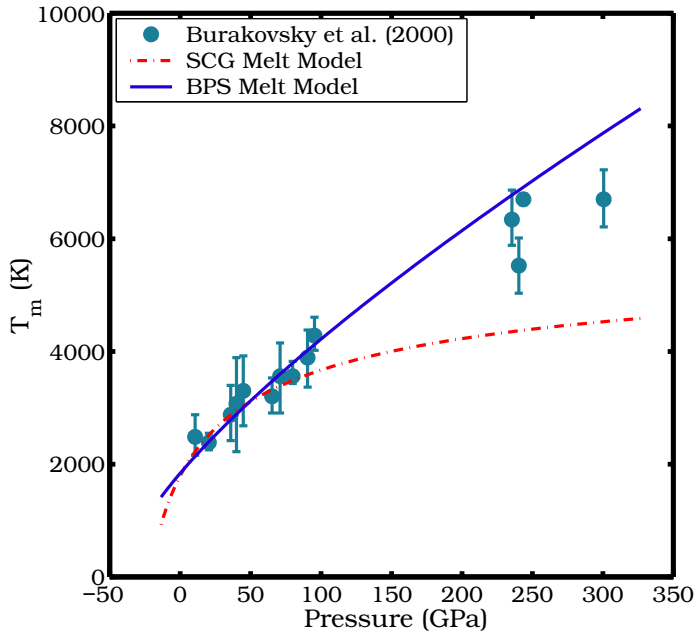

Fig. 14. Comparison of experimental data and model predictions of melting temperature for 4340 steel as a function of pressure.

have been obtained from Burakovsky and Preston [21] and Burakovsky et al. [23], and the lattice constant (a) has been taken from Jansen et al. [48]. The SCG model parameters have been obtained from Gust [40]. An initial density ρ_0 of 7830 kg/m^3 has been used in the model calculations.

4.3.2 Specific Heat Model for 4340 Steel

The constants for the specific heat model (equation 33) were fit with a least squares technique using experimental data for iron (Wallace et al. [90], Shacklette [79]) and AISI 3040 steel ([42]). The constants used in the simulations are shown in Table 12. The variation of specific heat with temperature that is predicted by the model is compared to the experimental data in Figure 15. The transition from the bcc α phase to the fcc γ phase is clearly visible in the figure. However, we do not

Table 11
Parameters used in melting temperature models for 4340 steel.

Steinberg-Cochran-Guinan (SCG) model		
$T_{m0}(K)$	Γ_0	a
1793	1.67	1.67

Burakovsky-Preston-Silbar (BPS) model										
K_0 (GPa)	$K_0^{'}$	μ_0 (GPa)	$\mu_0^{'}$	κ	z	$b^2\rho_c(T_m)$	α	λ	v_{WS} (Å^3)	a (Å)
166	5.29	81.9	1.8	1	8	0.78	2.9	1.30	$a^3/2$	2.865

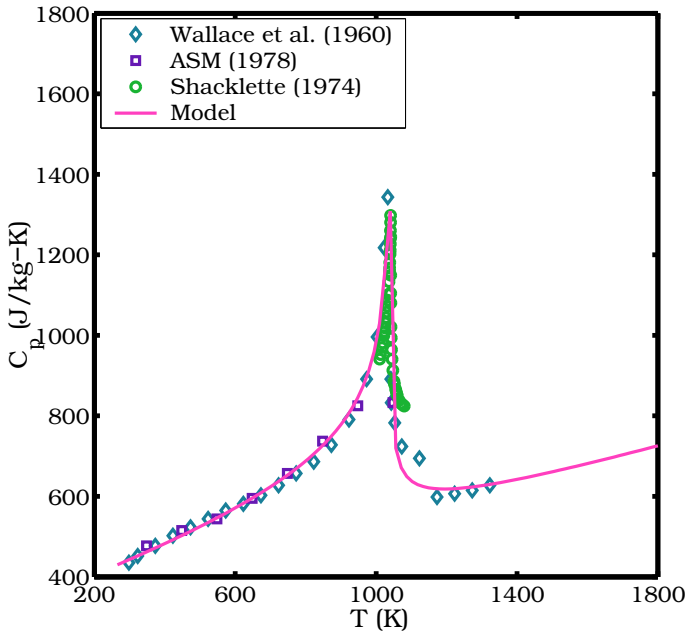

Fig. 15. Comparison of experimental data and model prediction of specific heat for 4340 steel as a function of temperature.

consider such a phase change in the melting temperature model and assume that the iron remains bcc at all pressures.

4.3.3 Equation of State for 4340 Steel

The pressure in the steel is calculated using the Mie-Grüneisen equation of state (equation 1) assuming a linear Hugoniot relation. The Grüneisen gamma (Γ_0) is assumed to be a constant over the regime of interest. The specific heat at constant volume is assumed to be the same as that at constant pressure and is calculated using equation (33). Table 13 shows the parameters used in the pressure calculation. The bulk speed of sound and the linear Hugoniot slope coefficient have been obtained from Brown et al. [20] for iron. The Grüneisen gamma value has been interpolated from the values given by Gust et al. [41]. An initial temperature (T_0) of 300 K and an initial density of 7830 kg/m^3 have been used in the model calculations.

Figure 16 compares model predictions with experimental data for iron (Bancroft et al. [5], McQueen et al. [62], Barker and Hollenbach [15]), mild steel (Katz et al. [54]), 300 series stainless steels (McQueen et al. [62]), and for AISI 4340 steel

Table 12
Constants used in specific heat model for 4340 steel.

T_c (K)	A_1 (J/kg-K)	B_1 (J/kg-K)	C_1 (J/kg-K)	α	A_2 (J/kg-K)	B_2 (J/kg-K)	C_2 (J/kg-K)	α'
1040	190.14	-273.75	418.30	0.20	465.21	267.52	58.16	0.35

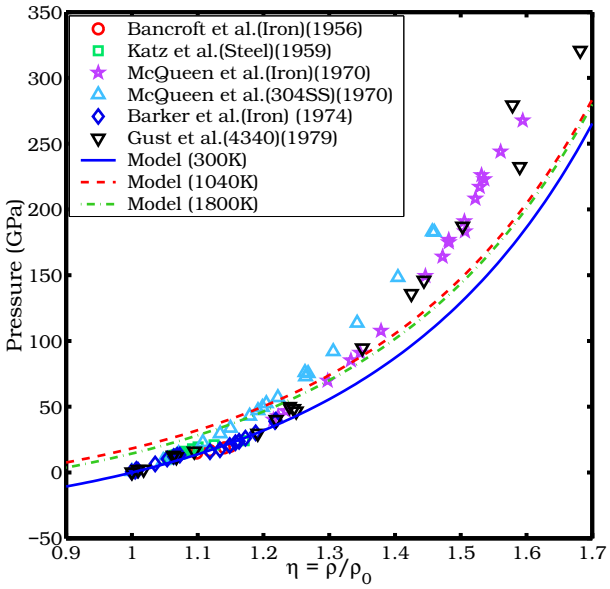

Fig. 16. Comparison of experimental data with model predictions of equation of state for 4340 steel.

(Gust et al. [41]). The high pressure experimental data are not along isotherms and show the temperature increase due to compression. The equation of state provides a reasonable match to the experimental data at compressions below 1.2 which is reasonable for the simulations of interest in this paper. Improved equations of state should be used for overdriven shocks.

4.3.4 Shear Modulus Models for 4340 Steel

To determine the model best suited to determine the dependence of the shear modulus on temperature and pressure, we have compared experimental data on AISI 1010 steel and SAE 304 stainless steel (Fukuhara and Sanpei [33]) to the predictions of the models discussed in Section 3.3.

The parameters used in the shear modulus models are shown in Table 14. The parameters for the MTS model have been obtained from a least square fit to the data at a compression of 1. The values of μ_0 and $\partial\mu/\partial p$ for the SCG model are from Guinan and Steinberg [38]. The derivative with respect to temperature has been chosen so as to fit the data at a compression of 1. The NP shear model parameters μ_0 and C have also been chosen to fit the data. A value of 0.57 for C is suggested by Nadal and Le Poac [64]. However, this value leads to a higher value of μ at high

Table 13
Constants used in the Mie-Grüneisen equation of state for 4340 steel.

C_0 (m/s)	S_α	Γ_0
3935	1.578	1.69

Table 14
Parameters used in shear modulus models for 4340 steel.

MTS shear modulus model				
μ_0 (GPa)	D (GPa)	T_0 (K)		
85.0	10.0	298		
SCG shear modulus model				
μ_0 (GPa)	$\partial\mu/\partial p$	$\partial\mu/\partial T$ (GPa/K)		
81.9	1.8	0.0387		
NP shear modulus model				
μ_0 (GPa)	$\partial\mu/\partial p$	ζ	C	m (amu)
90.0	1.8	0.04	0.080	55.947

temperatures.

Figure 17 shows the performance of the three models for three values of compression. The melting temperature is determined using the BPS model discussed earlier. The initial density is taken to be 7830 kg/m^3. The MTS model shows no pressure dependence of the shear modulus unless the melting temperature is computed as a function of pressure. However, the model behaves well at low temperatures for $\eta = 1$. Both the SCG and NP shear modulus models are pressure dependent and provide a good fit to the data. We have used the NP shear modulus model for subsequent calculations for 4340 steel because of its smooth transition to zero modulus at melt.

Details of the validation of the Johnson-Cook and the Mechanical Threshold Stress models of 4340 steel can be found in Banerjee [10].

5 TAYLOR TEST SIMULATIONS

The attractiveness of the Taylor impact test arises because of the simplicity and inexpensiveness of the test. A flat-ended cylinder is fired on a target at a relatively high velocity and the final deformed shape is measured. The drawback of this test is that intermediate states of the cylinder are relatively difficult to measure.

In this section, we compare the deformed profiles of simulated Taylor cylinders with experimental profiles. The experimental profiles were scanned at a high resolution and digitized using XFig (Sutanthavibul et al. [85]). The digitized curves were aligned with a grid and scaled to units of length using cues from the digitized images and their axes (if any were provided). We get errors of around 2% in the digitized profile during this procedure.

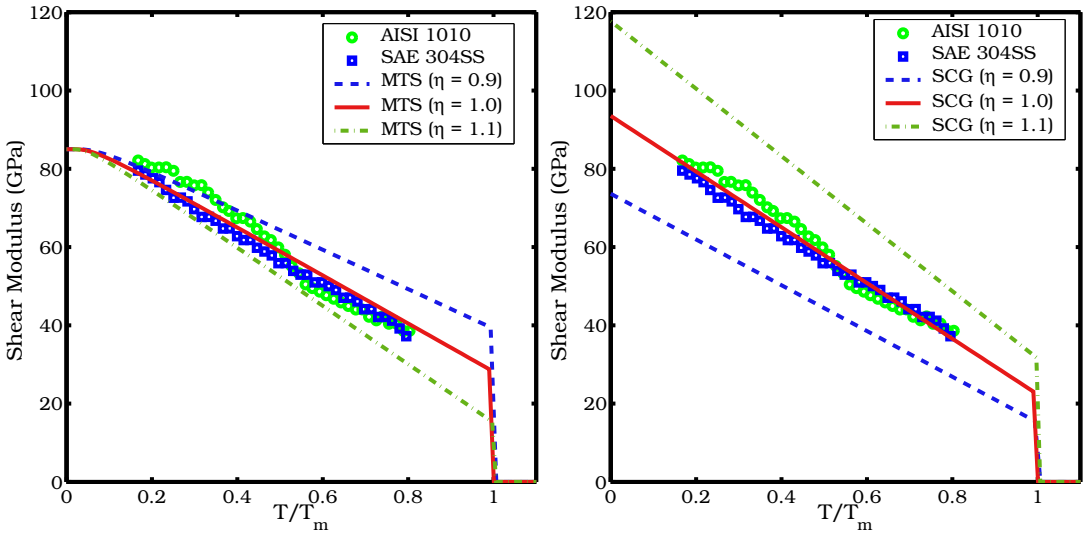

(a) MTS Shear Model

(b) SCG Shear Model

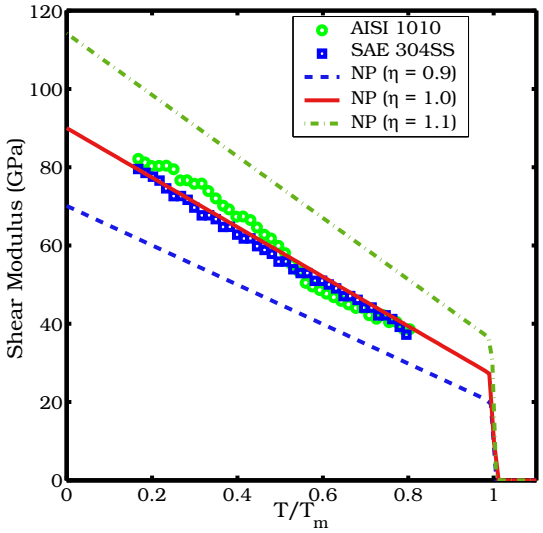

(c) NP Shear Model

Fig. 17. Comparison of experimental data with model predictions of shear modulus for 4340 steel.

We have used the Material Point Method for our simulations within the parallel UINTAH code. The computations were performed for a quarter of the cylinder. We have used 8 material points per cell (64 material points per cell for simulations at 1235 K), a 8 point interpolation from material points to grid, and a cell spacing of 0.3 mm. A cell spacing of 0.15 mm gives essentially the same final deformed profile. The anvil is modeled as a rigid material. Contact between the cylinder and the anvil is assumed to be frictionless.

Our simulations were run for 150 μs - 200 μs depending on the problem. These times were sufficient for the cylinders to rebound from the anvil and to stop undergoing further plastic deformation. However, small elastic deformations continue to persist as the stress waves reflect from the surfaces of the cylinder.

We have performed a systematic and extensive set of verification and validation tests to determine the accuracy of the Material Point Method and its implementation within UINTAH (Banerjee [9, 7, 8, 12, 10]). A number of materials and conditions have been explored in the process. We are, therefore, reasonably confident in the results of our simulations.

Figures 18(a) shows an experiment that involves very large deformations and frictional contact between the Taylor cylinder and the anvil. The material is mild steel. To determine if our algorithm could be used to simulate such large deformations, we ran a Taylor impact test on the problem geometry using the Johnson-Cook plasticity model for 4340 steel. Figure 18(b) shows the predicted profile overlaid on the experimental profile.

The simulated and experimental profiles are remarkably close to each other. Interestingly, the experiment also shows that the tips of the "mushroom" have broken off. We did not simulate any fracture and hence we do not see that effect. Note that the mushrooming of the end appears to be strongly dependent on the coefficient of friction between the cylinder and the anvil. If there is no friction, then the mushrooming effect is much smaller and the radius of curvature of deformed end of the cylinder is considerably larger. None of the more recent Taylor tests (that we use to compare the five flow stress models) show the amount of mushrooming seen in Figure 18(a). It is for this reason that we have chosen to use frictionless contact in our Taylor impact simulations.

5.1 Validation Metrics

The validation metrics that we consider in this paper are based on the final shape of the cylinder though other metrics may be considered if measurements of these are made during the course of an impact test. We note that the Taylor test could also be used to validate simulations of dynamic fracture though we do not address that issue in this paper.

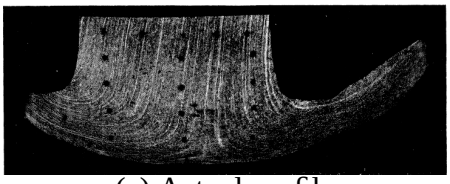

(a) Actual profile.

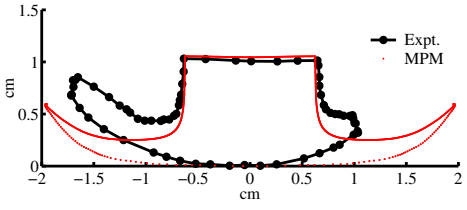

(b) Computed vs. actual profile.

Fig. 18. Comparison of experimental vs. computed shapes. L_0 = 25.37 mm , D_0 = 12.7 mm, V_0 = 652.3 m/s. The experimental profile is from Carrington and Gayler [24] (plate 1, figure 3).

There is a large literature on the systematic verification and validation of computational codes (see Oberkampf et al. [68], Babuska and Oden [4] and references therein). It has been suggested that validation metrics be developed that can be used to compare experimental data and simulation results. The metrics discussed in this paper are intended to be a step in that direction but are certainly not comprehensive.

The most common metric used in the literature is the "view-graph norm" (Oberkampf et al. [68]) where a plot of the simulated deformed configuration is superimposed on the experimental data and a visual judgement of accuracy is made. Examples can be found in Wilkins and Guinan [95], Johnson and Cook [49]. There is value to this approach and we present some of our data in this form. However, when the number of Taylor tests is large, it is not possible to present sectional/plan views for all the tests and numerical metrics are preferable. We believe that a representative set of geometrical metrics can provide information that can be used for quantitative comparisons between simulation and experiment.

Some metrics that have been used to compare Taylor impact tests are:

(1) The final length of the deformed cylinder (L_f) (Wilkins and Guinan [95], Gust [40], Jones and Gillis [53], Johnson and Holmquist [51], House et al. [47]).
(2) The diameter of the mushroomed end of the cylinder (D_f) (Johnson and Holmquist [51], House et al. [47]).
(3) The length of the elastic zone in the cylinder (X_f) (Jones and Gillis [53], House et al. [47]).
(4) The bulge at a given distance from the deformed end (W_f) (Johnson and Holmquist [51]).

Contours of plastic strain have also been presented in a number of works on Taylor impact. However, we do not find such contours to be particularly useful in comparing simulations with experiments. We note that contours of plastic strain are useful when the results of simulations with two different numerical techniques are compared.

We consider some additional geometrical metrics that can be compared with experimental data. These metrics can act as a substitute for detailed pointwise geometrical comparisons between two Taylor test profiles. We also consider metrics such as the time at which the cylinder rebounds from the anvil and the surface temperature profile; both of which can be measured during the course of an experiment. The additional geometric metrics that we compute in our simulations are:

(1) The final length of a axial line on the surface of the cylinder (L_{af}).
(2) The area of the cross-sectional profile of the deformed cylinder (A_f).
(3) The volume of the deformed cylinder (V_f).
(4) The location of the centroid of the deformed cylinder in terms of a orthonormal basis with origin at deformed end (C_{xf}, C_{yf}).
(5) The moments of inertia of the cross section of the deformed cylinder about

the basal plane (I_{xf}) and an axial plane (I_{yf}).

Higher order moments should also be computed so that we can dispense with arbitrary measures such as W_f.

Figure 19 shows the metrics that we have used to compare deformed Taylor cylinder profiles in this work. The numerical formulas used to compute the area, volume, centroid, and moments of inertia are given in Appendix C.

5.2 Taylor impact experiments on copper

Figure 20 shows the ratio of the final lengths of Taylor cylinders to their initial lengths (L_f/L_0) for a number of Taylor impact tests. These ratios have been plotted as a function of the sum of the initial kinetic energy density and the initial internal energy density (relative to a fixed temperature of 294 K). The internal energy density has been added to shift the data according to temperature. The plot indicates the following:

(1) The ratio (L_f/L_0) is essentially independent of the initial length and diameter of the cylinder.
(2) There is a linear relationship between the ratio (L_f/L_0) and the initial kinetic energy density.
(3) As temperature increases, the absolute value of the slope of this line increases.
(4) The deformation of OFHC (Oxygen Free High Conductivity) cannot be distinguished from that of ETP (Electrolytic Tough Pitch) copper from this plot.

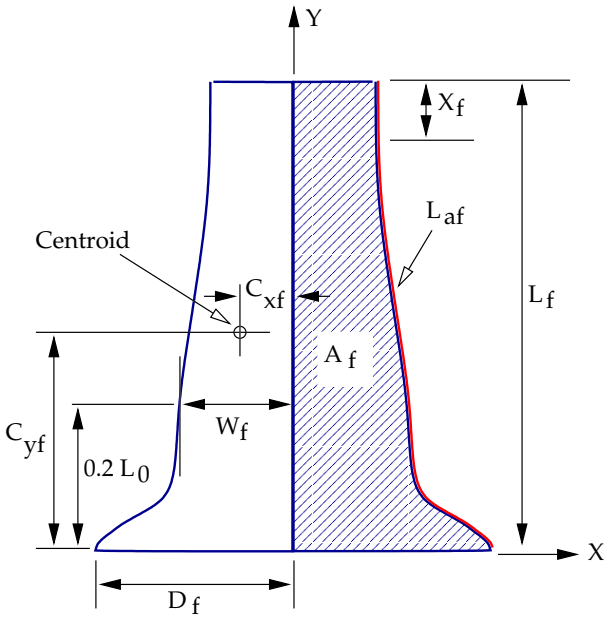

Fig. 19. Geometrical metrics used to compare profiles of Taylor impact specimens.

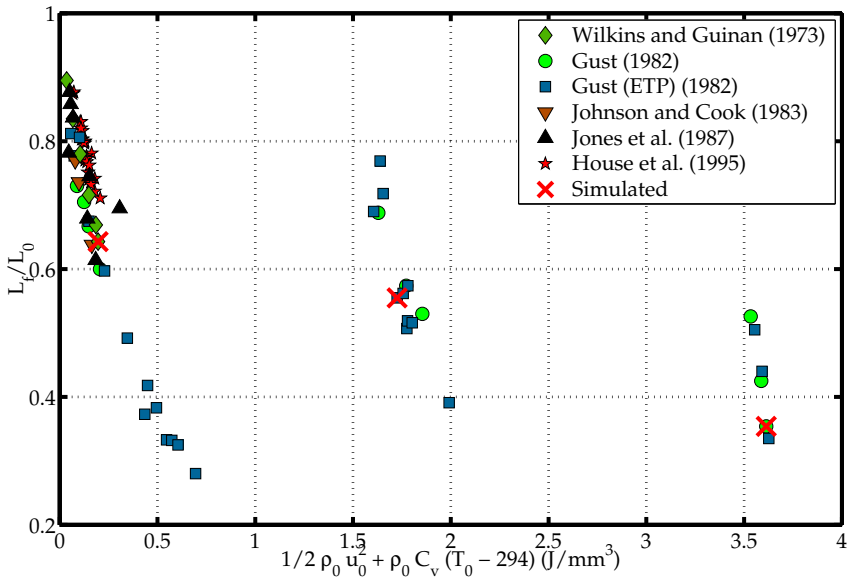

Fig. 20. Ratio of final length to initial length of copper Taylor cylinders for various conditions. The data are from Wilkins and Guinan [95], Gust [40], Johnson and Cook [49], Jones and Gillis [53] and House et al. [47].

We have chosen to do detailed comparisons between experiment and simulation for the three tests marked with crosses on the figure. These tests represent situations in which fracture has not been observed in the cylinders and cover the range of temperatures of interest to us.

The ratio of the diameter of the deformed end to the original diameter (D_f/D_0) for some of these tests is plotted as a function of the energy density in Figure 21. A linear relation similar to that for the length is observed.

The length of the elastic zone at the end of the test is difficult to determine (especially for high strain rate and high temperature tests) and may not be a suitable metric for these conditions. This can be seen from the amount of variability in this metric shown in Figure 22.

Finally, the volume of the cylinder should be preserved during the Taylor test if isochoric plasticity holds. This metric can be used to determine the error in digitization of the profile of the cylinder if we assume isochoric behavior. Figure 23 shows the ratio of the final volume to the initial volume (V_f/V_0) as a function of the energy density. We can see that the volume is preserved for three of the tests but not for the rest. It may be possible to attribute the difference to errors in measurement. One error in the experiments may be quantified with this metric.

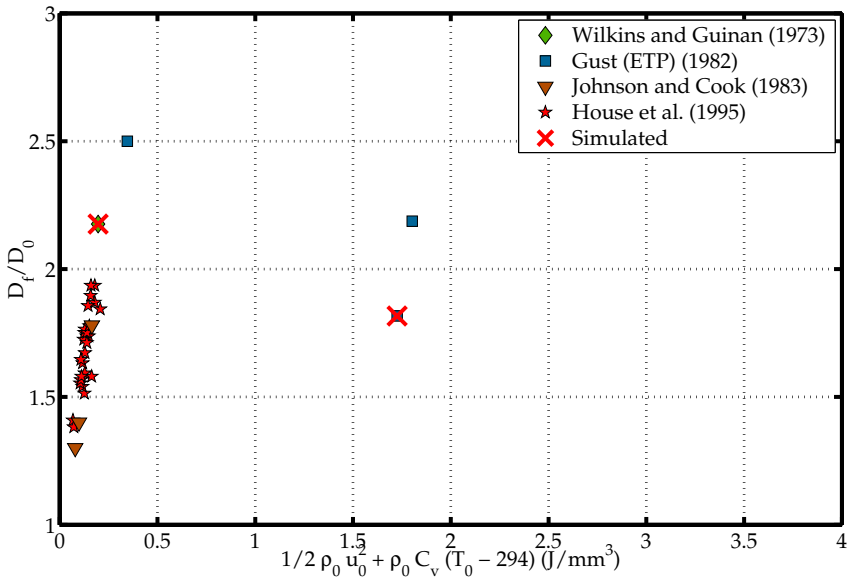

Fig. 21. Ratio of final length to initial length of copper Taylor cylinders for various conditions. The data are from Wilkins and Guinan [95], Gust [40], Johnson and Cook [49] and House et al. [47].

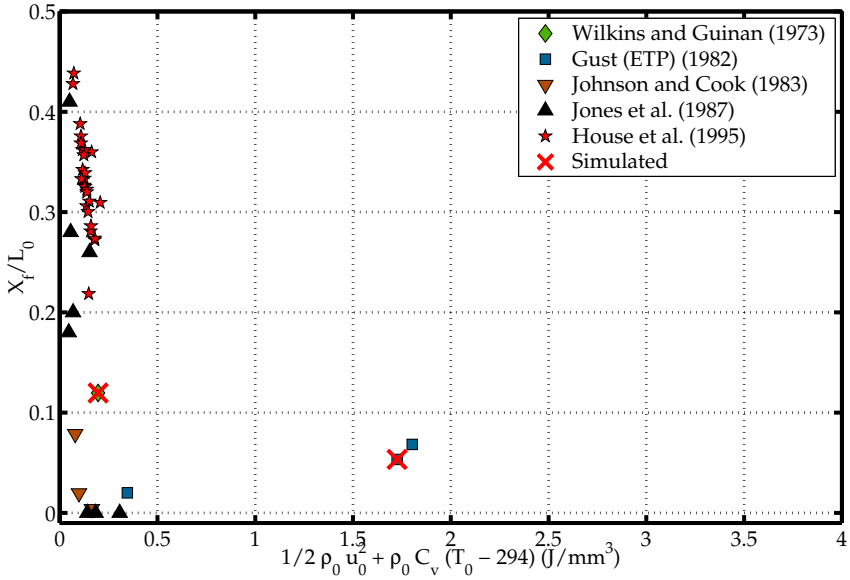

Fig. 22. Ratio of the length of the elastic zone to initial length of copper Taylor cylinders for various conditions. The data are from Wilkins and Guinan [95], Gust [40], Johnson and Cook [49] and House et al. [47].

5.3 Taylor impact simulations of copper

In this section we present results from simulations of three Taylor tests on copper, compute validation metrics, and compare these metrics with experimental data. Table 15 shows the initial dimensions, velocity, and temperature of the specimens

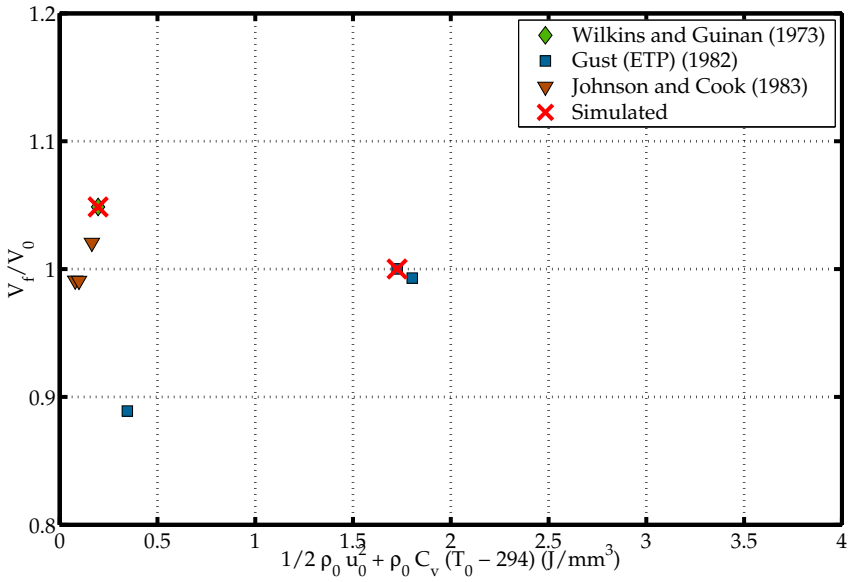

Fig. 23. Ratio of the final volume to initial volume of copper Taylor cylinders for various conditions. The data are from Wilkins and Guinan [95], Gust [40] and Johnson and Cook [49].

Table 15
Initial data for copper simulations.

Test	Material	Initial Length (L_0 mm)	Initial Diameter (D_0 mm)	Initial Velocity (V_0 m/s)	Initial Temperature (T_0 K)	Source
Cu-1	OFHC Cu	23.47	7.62	210	298	Wilkins and Guinan [95]
Cu-2	ETP Cu	30	6.00	188	718	Gust [40]
Cu-3	ETP Cu	30	6.00	178	1235	Gust [40]

that we have simulated. All specimens were annealed before testing.

5.3.1 Test Cu-1

Figures 24(a), (b), (c), (d), and (e) show the experimental profiles and the profiles computed by the JC, SCGL, ZA, MTS, and PTW models, respectively, for test Cu-1. The Johnson-Cook model gives the best match to the experimental data at this temperature (room temperature) if we consider the final length and the final mushroom diameter. All the other models underestimate the mushroom diameter but predict the final length quite well. The MTS model slightly underestimates the final length.

The time at which the cylinder loses all its kinetic energy (as predicted by the models) is shown in the energy plot of Figure 25. The predicted times vary from

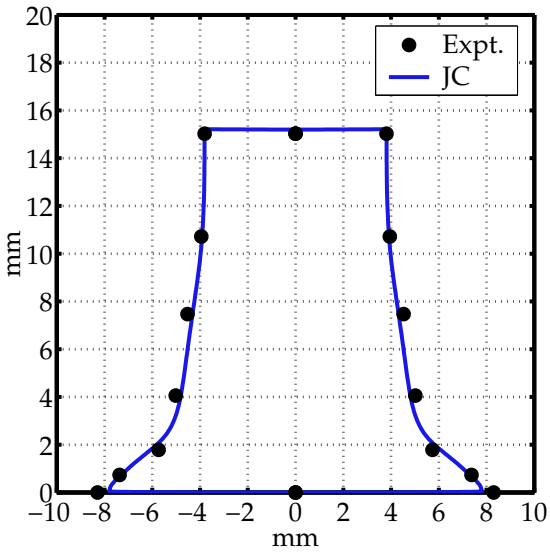

(a) Johnson-Cook.

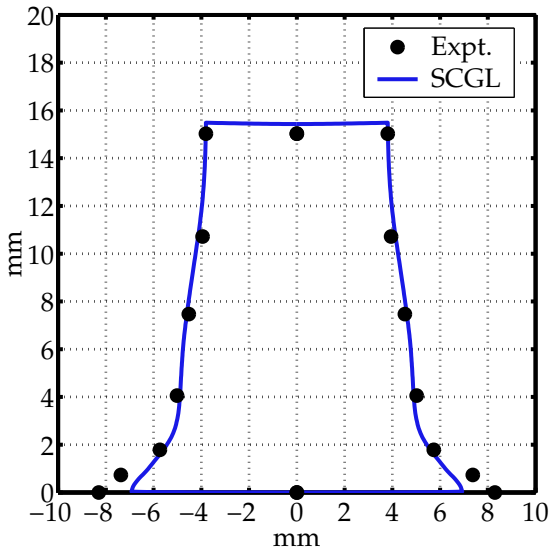

(b) Steinberg-Cochran-Guinan-Lund.

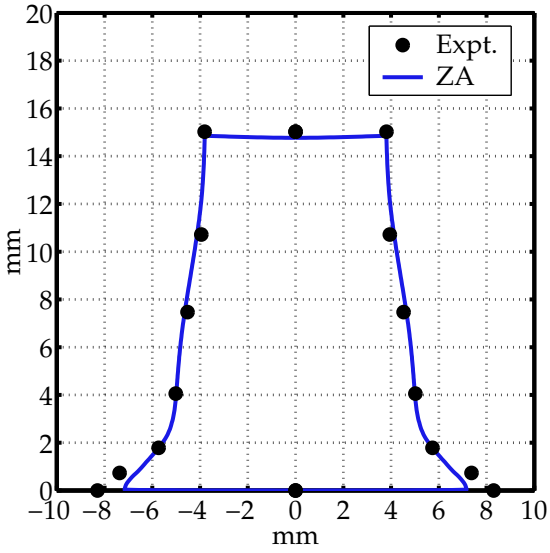

(c) Zerilli-Armstrong

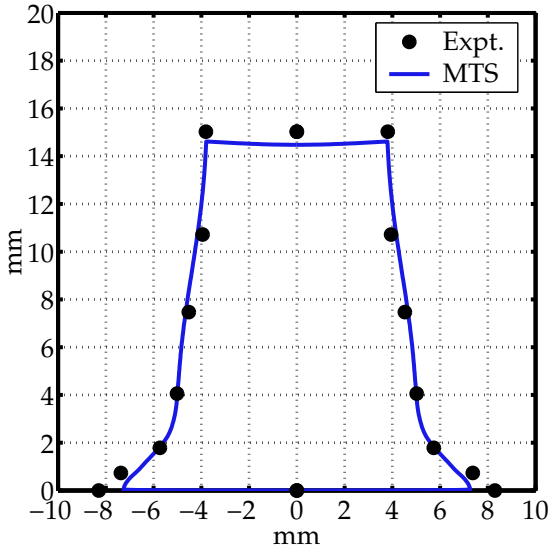

(d) Mechanical Threshold Stress.

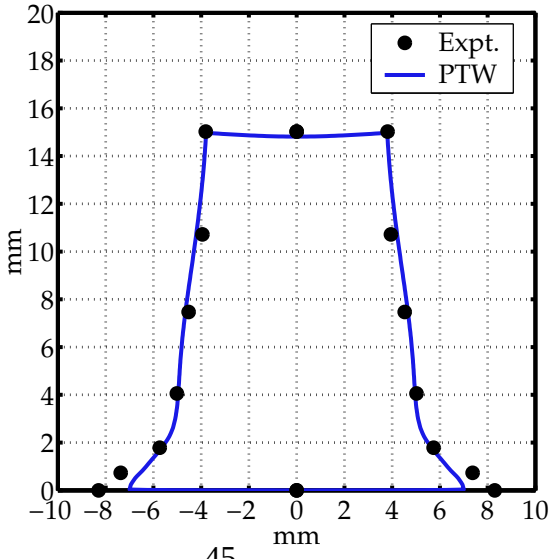

(e) Preston-Tonks-Wallace.

Fig. 24. Computed versus experimental profiles for Taylor test Cu-1.

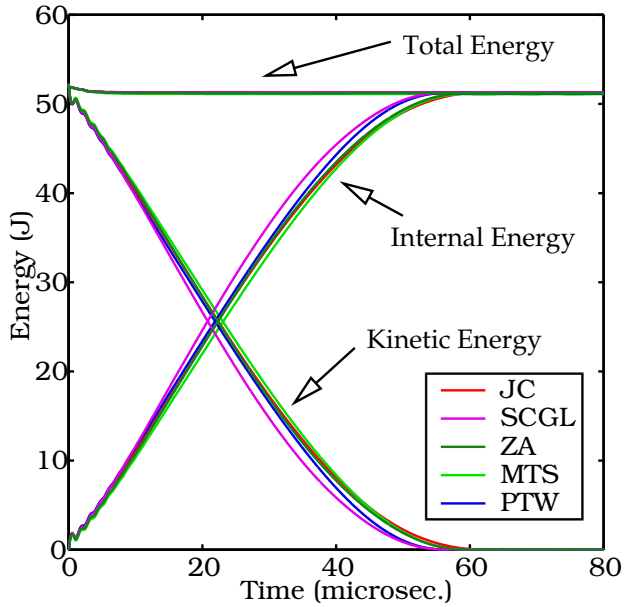

Fig. 25. Energy a function of time predicted by the five models for Taylor test Cu-1.

approximately 55 micro secs to 60 micro secs but are essentially the same for all the models. The total energy is conserved relatively well. The slight initial dissipation is the result of the artificial viscosity in the numerical algorithm that is used to damp out initial oscillations.

From Figure 23 we can see that the final volume of the cylinder for test Cu-1 is around 5% larger than the initial volume. We assume that this error is due to errors in digitization. In that case, we have errors of +1% for measures of length and errors of +2% for measures of area in the experimental profile. Moments of inertia of areas are expected to have errors of around 7%.

The error metrics for test Cu-1 are shown in Figure 26. The final length (L_f) is predicted to within 3% of the experimental value by all the models. The Johnson-Cook and Preston-Tonks-Wallace models show the least error.

The length of the deformed surface of the cylinder (L_{af}) is predicted best by the Johnson-Cook and Steinberg-Cochran-Guinan-Lund models. The other models underestimate the length by more than 5%.

The final mushroom diameter (D_f) is underestimated by 5% to 15%. The Johnson-Cook model does the best for this metric, followed by the Mechanical Threshold Stress model.

The width of the bulge (W_f) is underestimated by the Johnson-Cook and SCGL models and accurately predicted by the ZA, MTS, and PTW models.

The length of the elastic zone (X_f) is predicted to be zero by the SCGL, ZA, MTS, and PTW models and 1.5 mm by the Johnson-Cook model. Further, an accurate

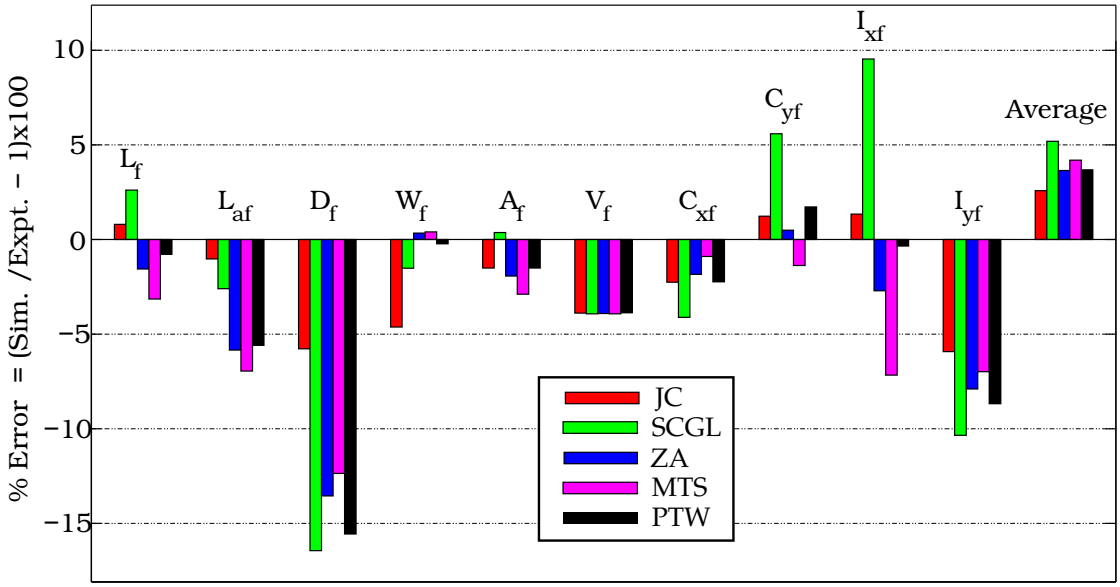

Fig. 26. Comparison of error metrics for the five models for Taylor test Cu-1.

estimate of the length of the zone cannot be made from the experimental profile for test Cu-1. Therefore we do not consider this metric of utility in our comparisons for this test.

From Figure 26 we see that the predicted area of the profile (A_f) is within 3% of the experimental value for all the models. The SCGL model shows the least error in this metric. If we decrease the experimental area by 2% (in accordance with the assumed error in digitization), the Johnson-Cook and PTW models show the least error in this metric.

The predicted final volume of the cylinder is around 0.8% larger than the initial volume showing that volume is not preserved accurately by our stress update algorithm. The error in digitization is around 5%. That gives us a uniform error of 5% between the experimental and computed volume (V_f) as can be seen in Figure 26.

The locations of the centroids (C_{xf}, C_{yf}) provide further geometric information about the shapes of the profiles. These are the first order moments of the area. The computed values are within 2% of experiment except for the MTS model which shows errors of -4% for C_{xf} and +6% for C_{yf}.

The second moments of the area are shown as I_{xf} and I_{yf} in Figure 26. The error in I_{xf} tracks and accentuates the error in L_f while the error in I_{yf} tracks the error in D_f. The width of the bulge is included in this metric and it can be used the replace metrics such as L_f, D_f, and W_f for the purpose of comparison. We notice this tracking behavior when the overall errors are small but not otherwise.

We have also plotted the arithmetic mean of the absolute value of the errors in each of the metrics to get an idea about which model performs best. The average error

is the least (2.5%) for the Johnson-Cook model, followed by the ZA and PTW models (3.5%). The MTS model shows an average error of 4% while the SCGL model shows the largest error (5%). If we subtract the digitization error from the experimental values, these errors decrease and lie in the range of 2% to 3%.

In summary, all the models predict profiles that are within the range of experimental variation for the test at room temperature. Additional simulations at higher strain rates (not presented in this work) have confirmed that all the models do well for room temperature simulations for strain rates ranging from 500 /s to 8000 /s. We suggest that the simplest model should be used for such simulations and our recommendation is the Zerilli-Armstrong model for copper.

As the next sections show, the above conclusion does not hold for high temperature simulations.

5.3.2 Test Cu-2

Figures 27(a), (b), (c), (d), and (e) show the experimental profiles and the profiles computed by the JC, SCGL, ZA, MTS, and PTW models, respectively, for test Cu-2 at 718 K. In this case, the Johnson-Cook model predicts the final length well but overestimates the mushroom diameter. The SCGL model overestimates the length but predicts the mushroom diameter well. The ZA model predicts the overall profile remarkably well except for the mushroom diameter. The MTS model slightly overestimates both the final length and the mushroom diameter. The PTW model also performs similarly, except that the error is slightly larger than that for the MTS model.

The energy plot for test Cu-2 is shown in Figure 28. In this case, the time of impact predicted by the JC and ZA models is around 100 micro secs while that predicted by the SCGL, MTS, and PTW models is around 90 micro secs.

From Figure 23 we see that the deformed volume computed from the digitized profile is almost exactly equal to the initial volume for test Cu-2. The digitization error can be neglected in this case. The error metrics for test Cu-2 are shown in Figure 29.

The least error in the predicted final length (L_f) is for the ZA model followed by the JC model. The SCGL model shows the largest error in this metric (7%). The MTS and PTW models overestimate the final length by around 6%.

The value of L_{af} is predicted to within 2% of the experimental value by the ZA model. The corresponding errors in the other models vary from 6% (MTS) to 9% (SCGL).

The mushroom diameter is overestimated by all models. The JC model overesti-

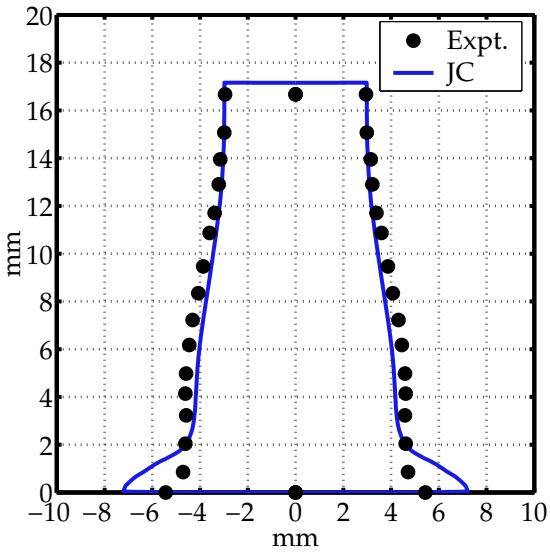

(a) Johnson-Cook.

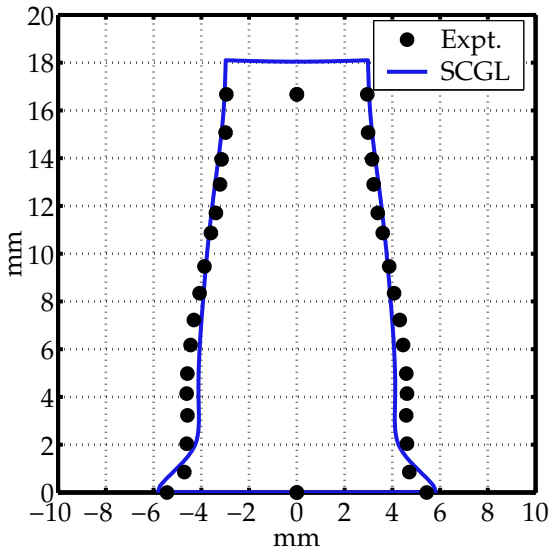

(b) Steinberg-Cochran-Guinan-Lund.

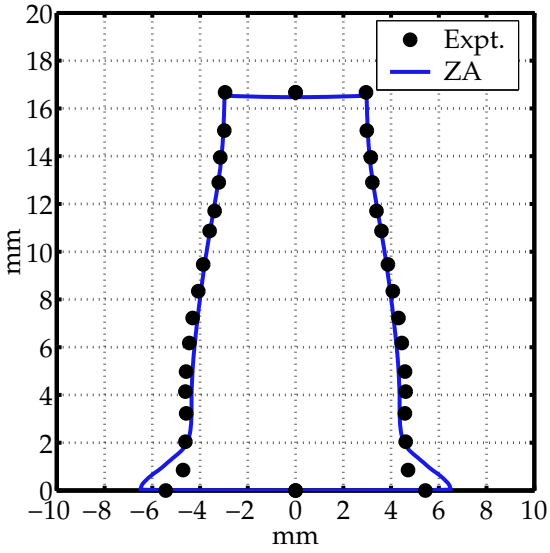

(c) Zerilli-Armstrong

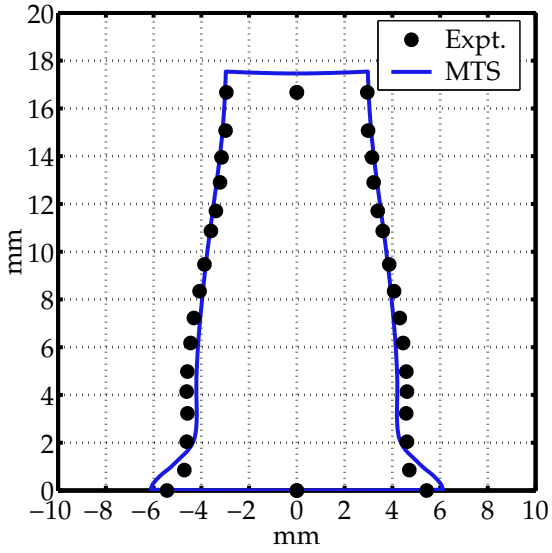

(d) Mechanical Threshold Stress.

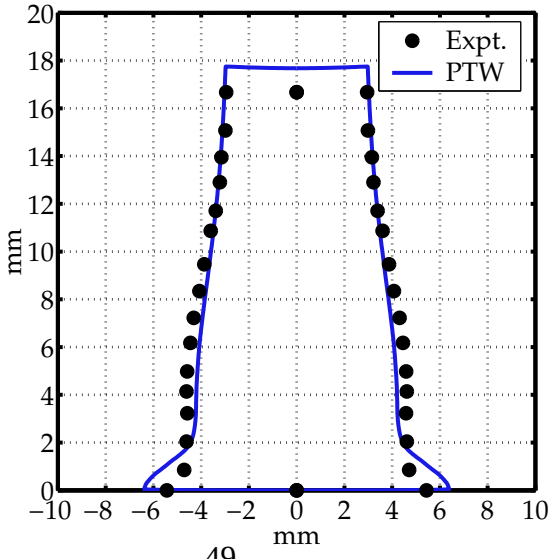

(e) Preston-Tonks-Wallace.

Fig. 27. Computed versus experimental profiles for Taylor test Cu-2.

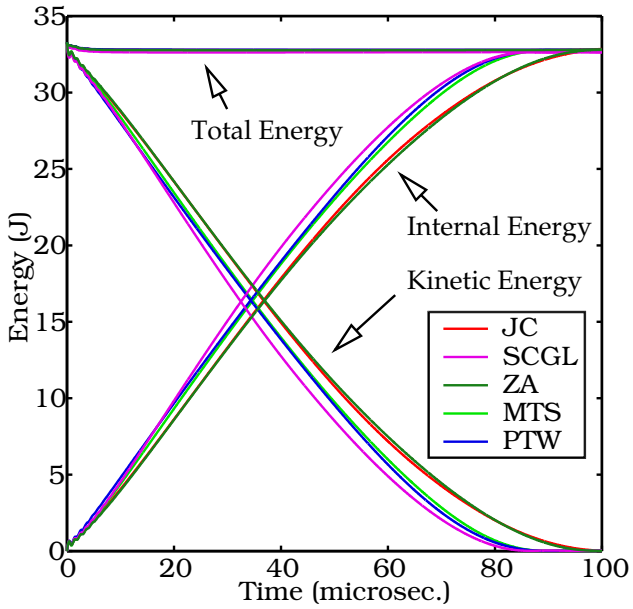

Fig. 28. Energy a function of time predicted by the five models for Taylor test Cu-2.

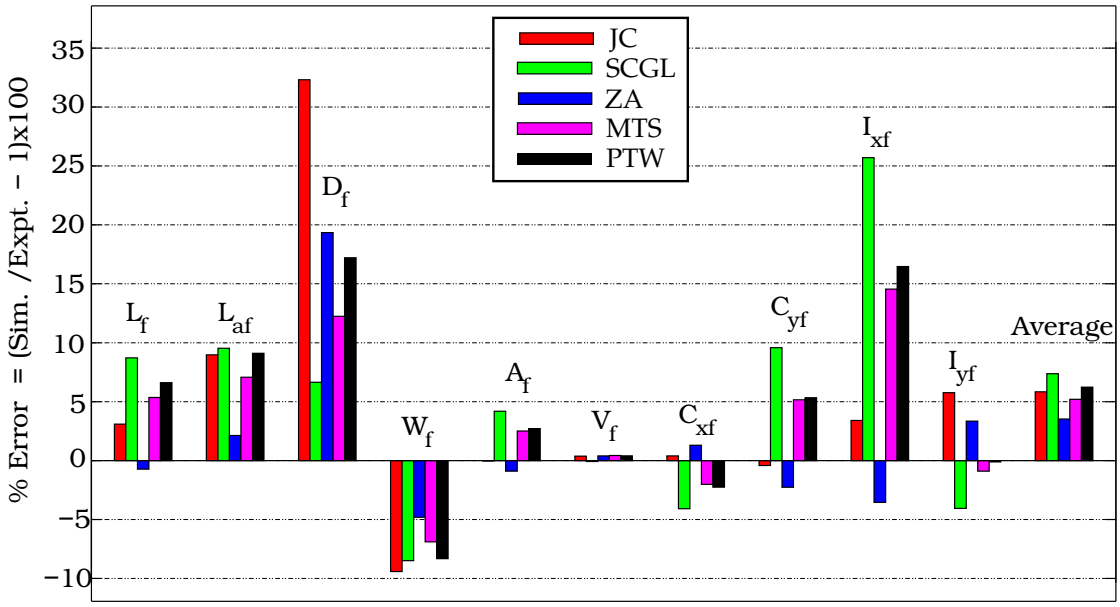

Fig. 29. Comparison of error metrics for the five models for Taylor test Cu-2.

mates this metric by more than 30%. The ZA and PTW models overestimate D_f by 17% to 19%. The MTS model overestimates D_f by 12%. The SCGL model does best with an error of 7%.

The width of the bulge is underestimated by all the models with errors varying between 5% (ZA) tp 9% (JC).

The final area (A_f) is predicted almost exactly by the JC model. The ZA model underestimates the area by 1% while the errors in the other models vary from 2%

to 4%. The error in the final volume is less than 1% for all the models.

The location of the centroid is predicted best by the Johnson-Cook model followed by the ZA model. Both the MTS and PTW models underestimate C_{xf} by 2% and overestimate C_{yf} by 5%. The SCGL model shows the largest error for this metric.

For the second order moments I_{xf}, the smallest error is for the Johnson-Cook model followed by the ZA model. The largest errors are from the SCGL model. The MTS and PTW models overestimate this metric my 15%. The PTW model predicts I_{yf} the best, followed by the MTS model showing that the overall shape of the profile is best predicted by these models. The Johnson-Cook and SCGL models show the largest errors in this metric.

On average, the ZA model performs best for test Cu-2 at 718 K with an average error of 4%. The MTS model shows an average error of 5% while the JC and PTW models show errors of approximately 6%. The SCGL model, with an average error of approximately 7%, does the worst.

5.3.3 Test Cu-3

Figures 30(a), (b), (c), (d), and (e) show the the profiles computed by the JC, SCGL, ZA, MTS, and PTW models, respectively, and the final length of the cylinder for test Cu-3 at 1235 K. The full profile of the cylinder was not available for this test. The Johnson-Cook model fails to predict a the deformation of the cylinder at this temperature and the material appears to flow along the plane of impact. The SCGL model predicts a reasonably close value of the final length. However, the low strain rate part of the SCGL model behaves in an unstable manner at some levels of discretization for this test and should ideally be discarded in high strain rate simulations. The ZA model overestimates the final length as does the MTS model. The PTW model predicts a final length that is closer to experiment but does not show the bulge that is characteristic of hardening. This can be seen from the tendency of the model to saturate prematurely as discussed in the section on one-dimensional tests.

The energy plot for test Cu-3 is shown in Figure 31. For this test, the JC model predicts a time of impact greater than 250 micro secs while the rest of the models predict values between 120 micro secs and 130 micro secs. The reason for the anomalous behavior of the JC model is that the rate dependence of the yield stress at high temperature is severely underestimated by the JC model. The nominal strain rate is around 5000/s for this test at which the yield stress should be considerably higher than the 50 MPa that is computed by the JC model.

We do not have the final profile of the sample for this test and hence cannot compare any metrics other than the final length. The final length is predicted most accurately by the SCGL model with an error of 10%, followed by the PTW model (error 15%)

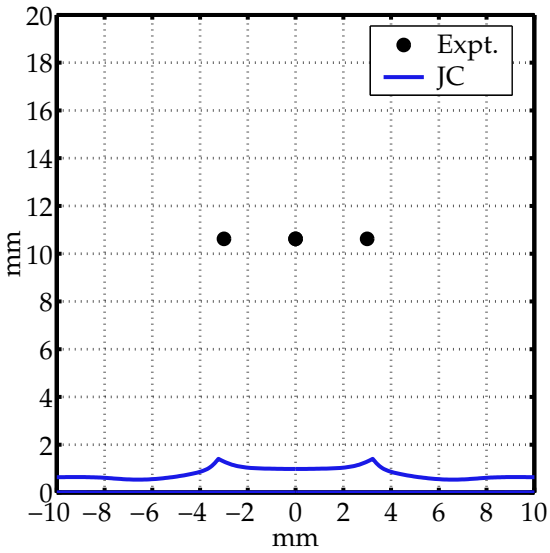

(a) Johnson-Cook.

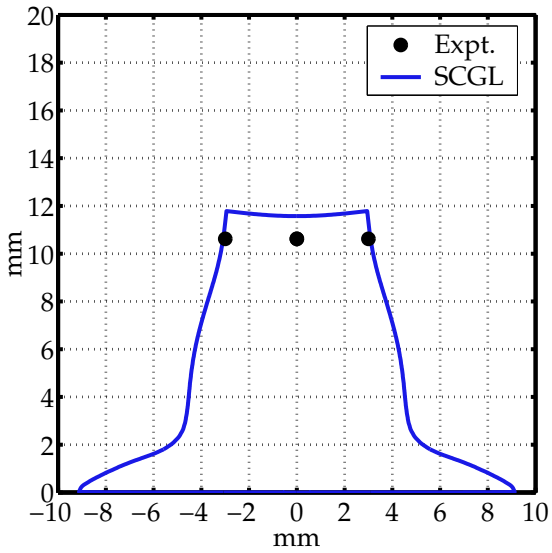

(b) Steinberg-Cochran-Guinan-Lund.

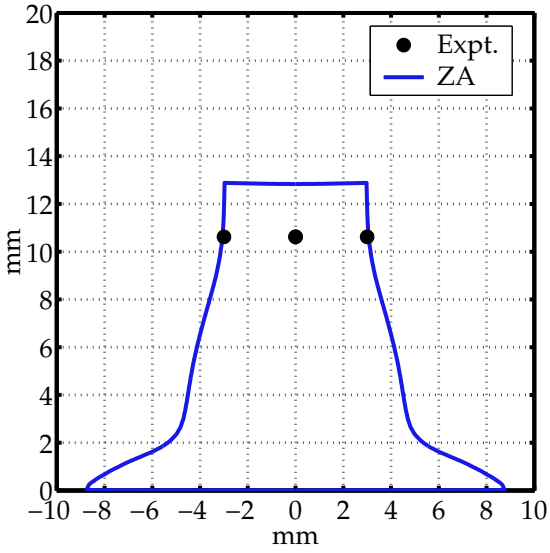

(c) Zerilli-Armstrong

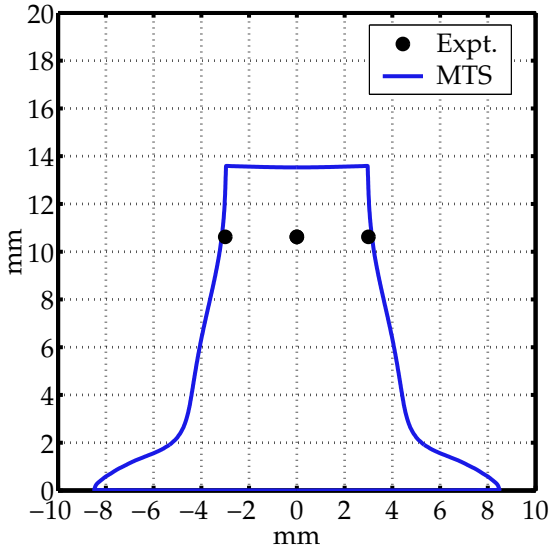

(d) Mechanical Threshold Stress.

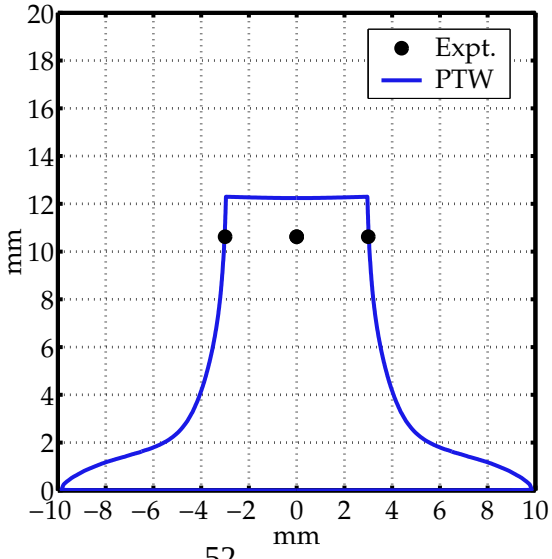

(e) Preston-Tonks-Wallace.

Fig. 30. Computed versus experimental profiles for Taylor test Cu-3.

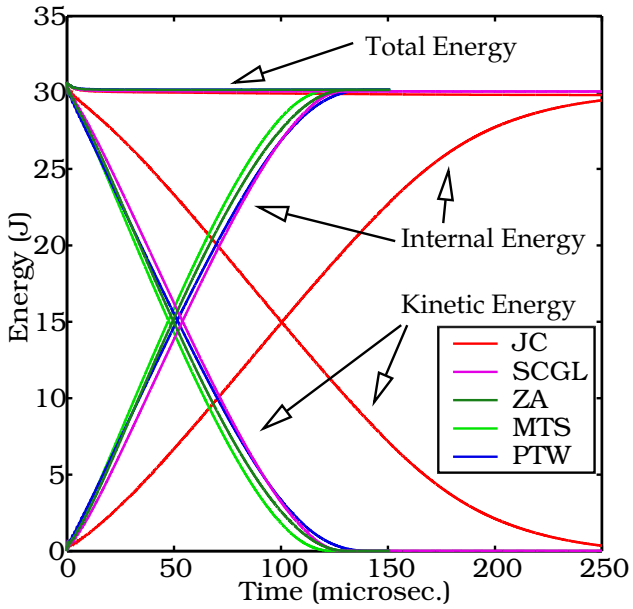

Fig. 31. Energy a function of time predicted by the five models for Taylor test Cu-3.

and the ZA model (error 20%). The Johnson-Cook model shown an error of more than 90%.

These three sets of tests show that the performance of the models deteriorates with increasing temperature. However, on average all the models predict reasonably accurate profiles for the Taylor impact tests. The choice of the model should therefore be dictated by the required computational efficiency and the conditions expected during simulations.

5.3.4 Other Taylor impact tests

We have also performed some more Taylor impact tests on copper to explore the effect of strain rate and friction, and for comparisons with MPM and FEM Some of these tests are discussed below.

Table 16 shows the initial dimensions, velocity, and temperature of the specimens (along with the type of copper used and the source of the data) that we have simulated and compared with experimental data. Not all the models have been used in what follows. For brevity, we do not present results from all the tests.

5.3.4.1 Performance of plasticity models at room temperature. Comparisons between the computed and experimental profiles of annealed copper specimen Cu-I are shown in Figure 32. For this test, the MTS model clearly performs better than the Johnson-Cook model in predicting the final length, mushroom diameter, and the overall profile. The bulge is slightly underestimated by the MTS model. This

test reflects what we have observed before, that is, at room temperature both the Johnson-Cook and the MTS model give good estimates of high strain rate plastic deformation.

5.3.4.2 Performance of plasticity models at high temperatures. At higher temperatures, the response of the plasticity models is quite different. Comparisons between the computed and experimental profiles of ETP copper specimen Cu-F are shown in Figure 33(a), (b), and (c). Those for specimen Cu-G are shown in Figure 33(d), (e), and (f). The parameters used for these models in these runs are those given by Gust [40] and Zocher et al. [101].

From the figures, we observe that the JC model does relatively well in predicting the overall profile at 718 K and 727 K. The MTS model overestimates the length and underestimates the mushroom diameter. The SCGL model does better than the JC model in predicting the final length but underestimates the diameter.

5.3.4.3 Effect of friction at the impact surface. If frictional contact at the impact surface is simulated, the final shapes of the specimens Cu-F and Cu-G are as shown in Figure 34. We have assume a coefficient of friction of 0.0002 between the Taylor cylinder and the anvil.

In this case, the edge of the deformed surface tends to curl away from the anvil. This effect is not observed for the zero friction contact case in the previous section. We are not sure whether the effect is truly physical or due to the effect of incorrectly computed normals at the corners of the cylinder. Incorrect normals could cause a fictitious upward force to be created that tends to push the edges away from the anvil. However, this effect is excepted to be small. The second effect that is observed is that the deformation of the end is smaller because of friction.

The final lengths of the samples do not appear to be affected significantly by friction and we see the same behavior as in Figure 33.

5.3.4.4 Comparisons with FEM. To determine how our MPM simulations compare with FEM simulations we have run two high temperature ETP copper impact tests using LS-DYNA (with the coupled structural-thermal option). Figure 35 shows the final deformed shapes for the two cases from the MPM and FEM simulations using Johnson-Cook plasticity.

The FEM simulations overestimate the final length. We were unable to refine the mesh further without serious spurious modes being generated. We believe the FEM simulations will be able to match the MPM simulations with further mesh refinement and adaptive remeshing near the base of the cylinder.

Table 16
Initial data for copper simulations. OFHC = oxygen free high conductivity. ETP = electrolytic tough pitch.

Case	Material	Initial Length (L_0 mm)	Initial Diameter (D_0 mm)	Initial Velocity (V_0 m/s)	Initial Temperature (T_0 K)	Source
Cu-A	OFHC Cu	23.47	7.62	210	298	Wilkins and Guinan [95]
Cu-B	OFHC Cu	25.4	7.62	130	298	Johnson and Cook [49]
Cu-C	OFHC Cu	25.4	7.62	146	298	Johnson and Cook [49]
Cu-D	OFHC Cu	25.4	7.62	190	298	Johnson and Cook [49]
Cu-E	ETP Cu	30	6.00	277	295	Gust [40]
Cu-F	ETP Cu	30	6.00	188	718	Gust [40]
Cu-G	ETP Cu	30	6.00	211	727	Gust [40]
Cu-H	ETP Cu	30	6.00	178	1235	Gust [40]
Cu-I	OFHC Cu	50.8	7.62	177	298	Zocher et al. [101]

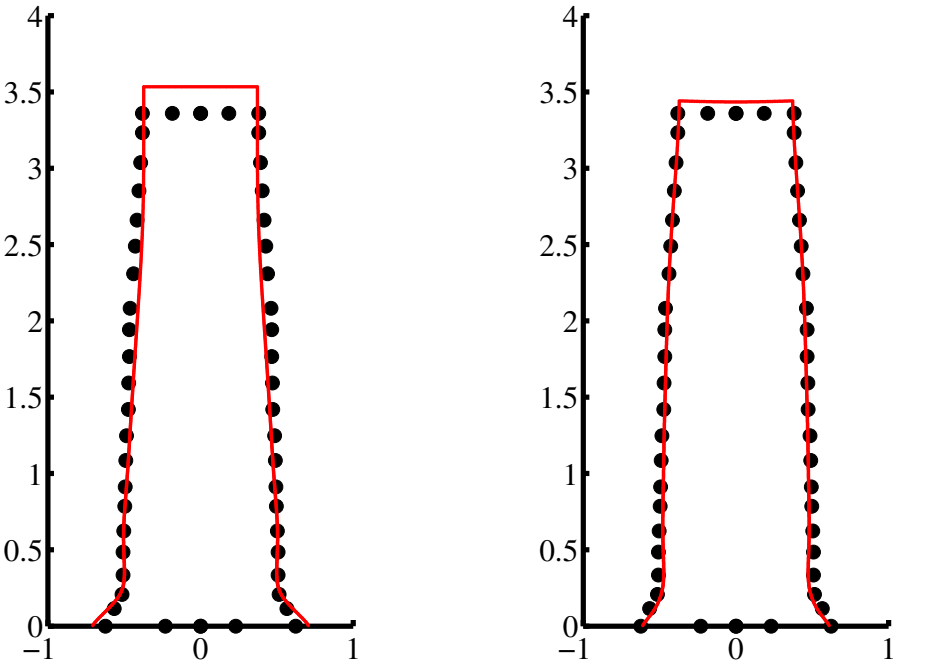

(a) Johnson-Cook. (b) Mechanical Threshold Stress.

Fig. 32. Comparison of experimental and computed shapes of annealed copper cylinder Cu-I using the Johnson-Cook and Mechanical Threshold Stress plasticity models. The axes are shown in cm units. The circles represent experimental data. The solid lines represent the simulated profiles.

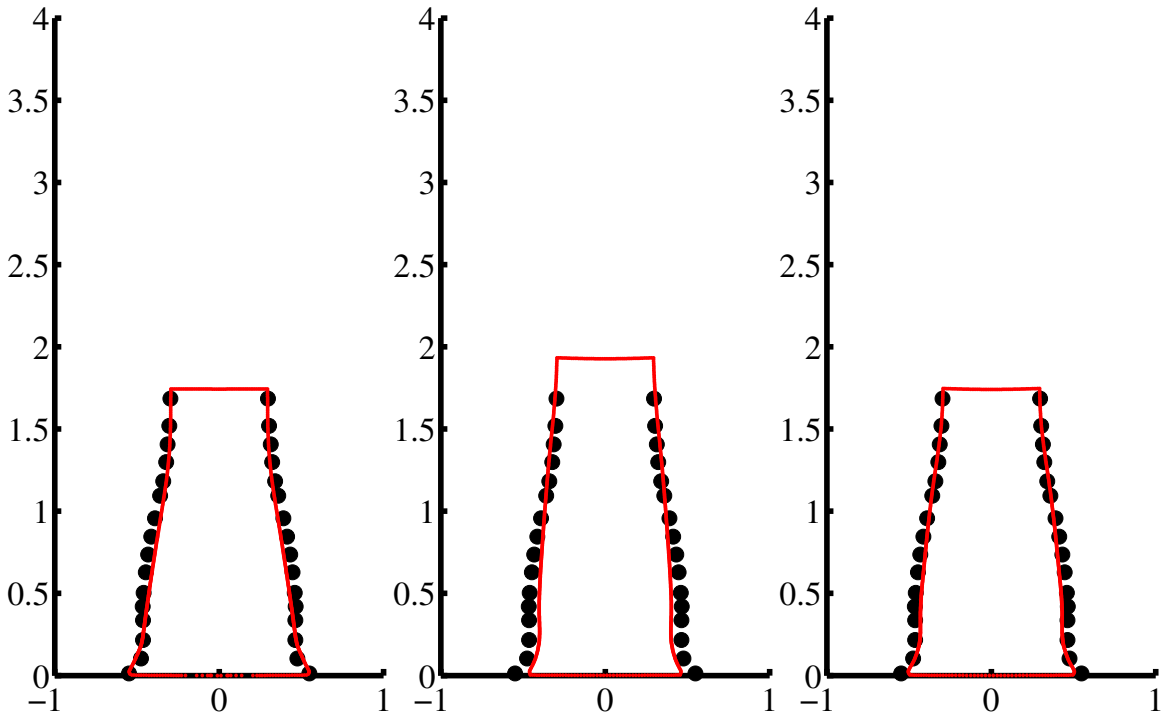

(a) JC (Cu-F) (b) MTS (Cu-F) (c) SCGL (Cu-F)

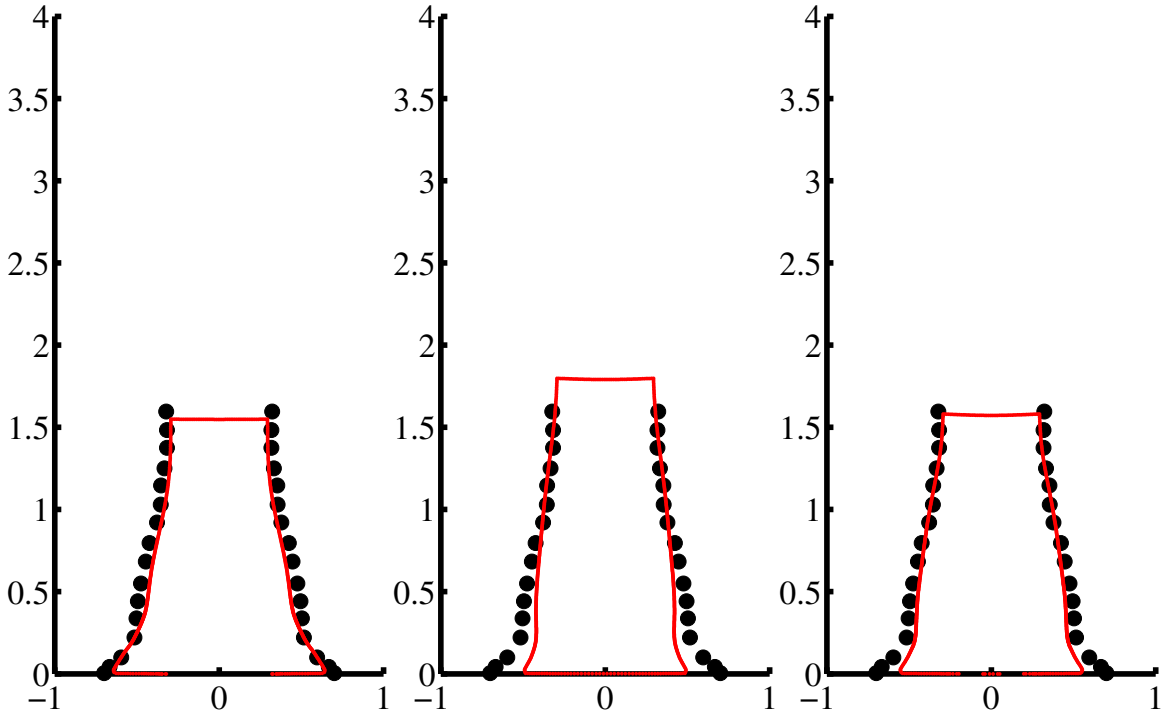

(d) JC (Cu-G) (e) MTS (Cu-G) (f) SCGL (Cu-G)

Fig. 33. Comparison of experimental and computed shapes of ETP copper cylinders Cu-F and Cu-G using the Johnson-Cook (JC), Mechanical Threshold Stress (MTS), and Steinberg-Cochran-Guinan-Lund (SCGL) plasticity models. The axes are shown in cm units. The circles represent experimental data. The solid lines represent the simulated profiles.

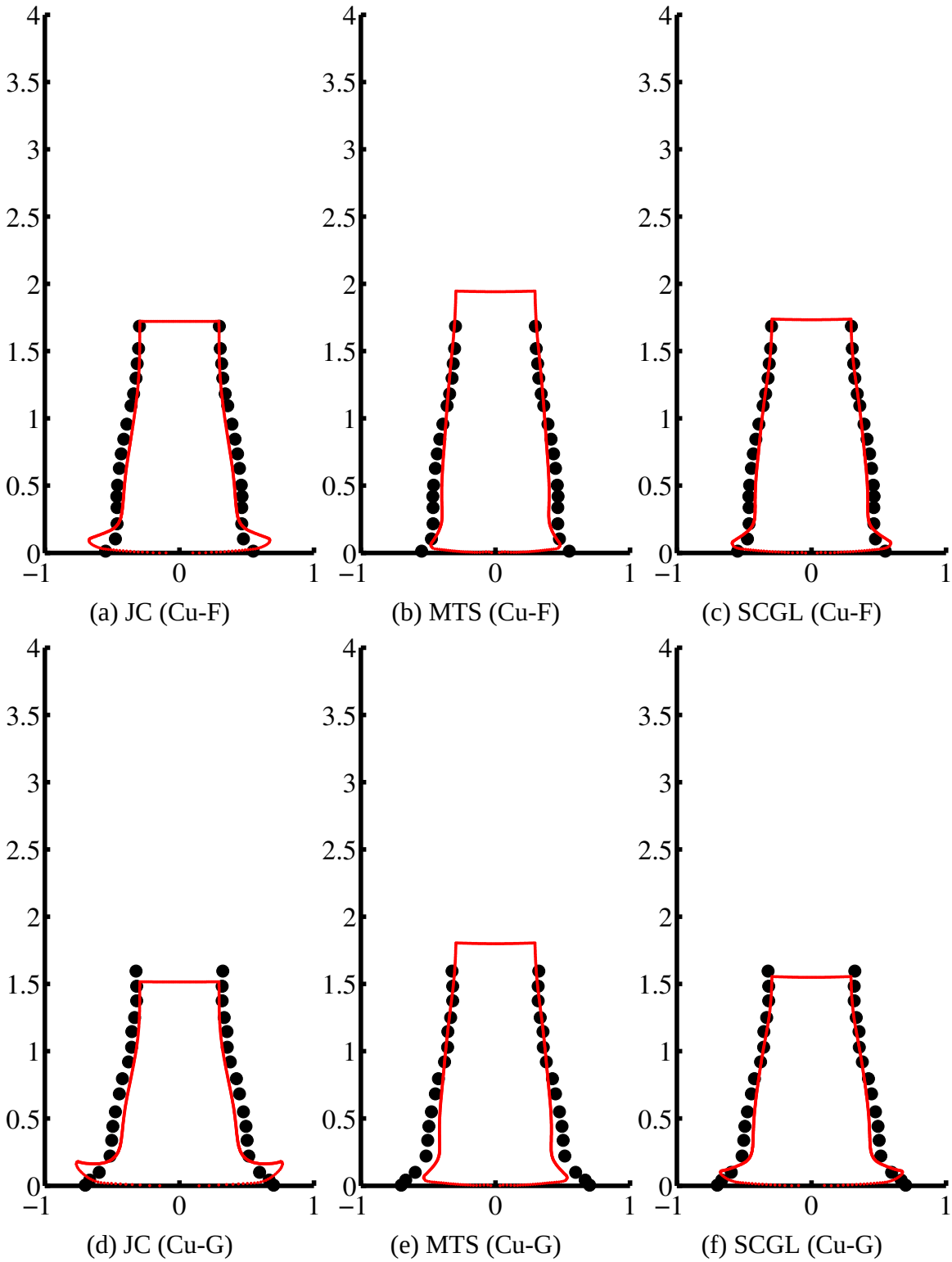

Fig. 34. Effect of frictional contact between the cylinder and the anvil. Comparison of experimental and computed shapes of ETP copper cylinders Cu-F and Cu-G using the Johnson-Cook (JC), Mechanical Threshold Stress (MTS), and Steinberg-Cochran-Guinan-Lund (SCGL) plasticity models. The axes are shown in cm units. The circles represent experimental data. The solid lines represent the simulated profiles.

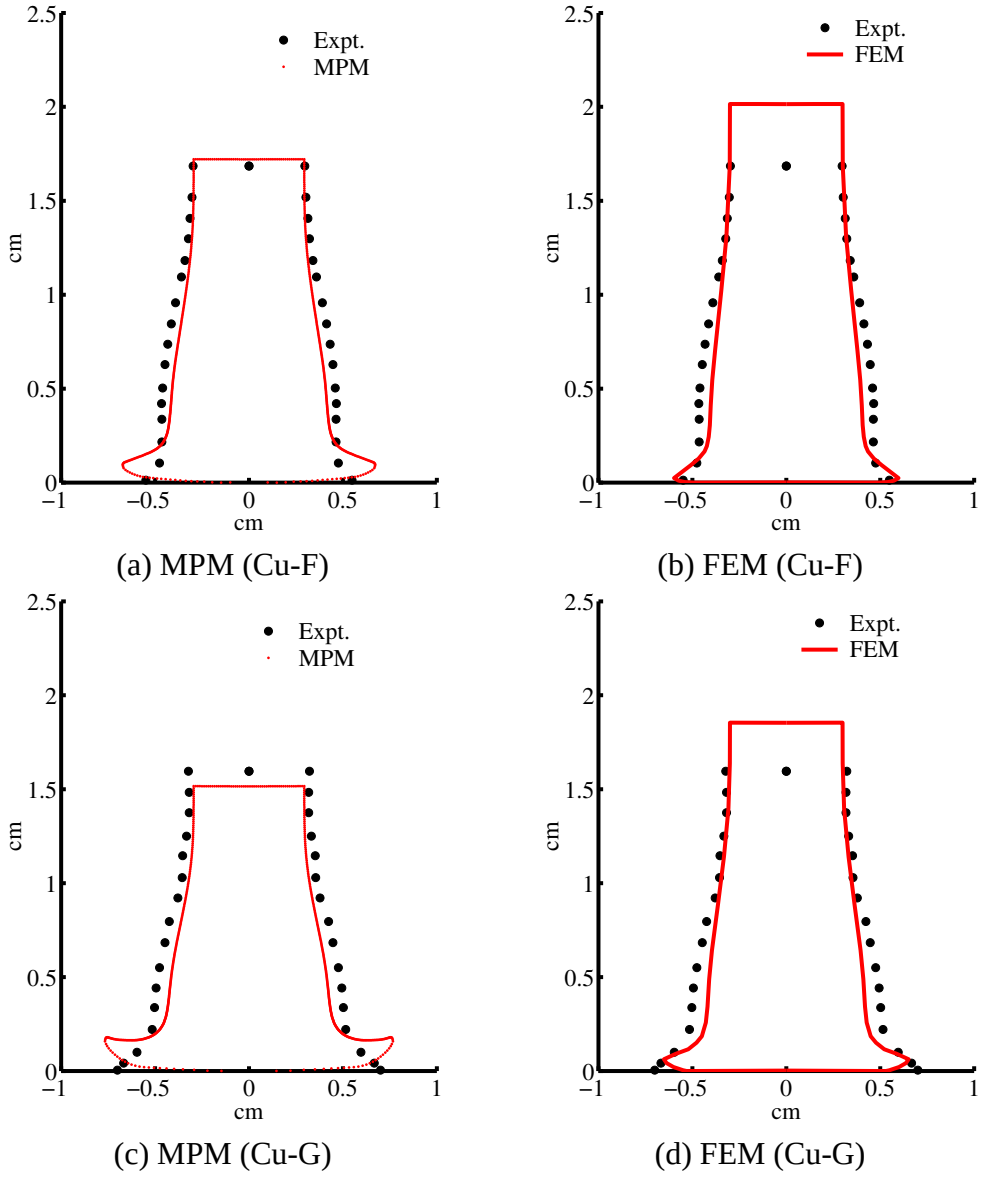

(a) MPM (Cu-F) (b) FEM (Cu-F)

(c) MPM (Cu-G) (d) FEM (Cu-G)

Fig. 35. Comparison of experimental and computed shapes of ETP copper cylinders Cu-F and Cu-G using MPM and FEM. The axes are in cm. The circles represent experimental data. The solid lines represent the simulated profiles.

Interestingly, the FEM simulations also show a turned up edge at the base. This indicates that the effect that we discussed in the previous section may be real and not an artifact of the contact algorithm.

5.3.4.5 Effect of mesh refinement. Simulations of impact case Cu-I with increasing mesh refinement are shown in Figure 36(a) (with friction) and in Figure 36(b) (without friction). The coarse mesh has a grid spacing of 0.64 mm, the medium mesh has a grid spacing of 0.32 mm, and the fine mesh has a spacing of

0.16 mm. The number of particles per grid cell is 27 and a 27 node GIMP interpolation is used to move information from particles to the grid and vice versa.

We can see that the final length is predicted correctly by the coarse mesh but not the mushroom diameter. The Medium and fine meshes predict the same final lengths and mushroom diameters. We take this to mean that we have arrived at a converged solution with the medium mesh. This is the mesh size that we have used for all our computations. We have observed the same behavior for simulations at 718 K and 727 K. However, a finer mesh is needed to obtain the converged solution at 1235 K.

5.4 Taylor tests on 6061-T6 aluminum alloy

In this section we present the results from Taylor tests on 6061-T6 aluminum specimens for different initial temperatures and impact velocities. We have chosen to study this material as it is a well characterized face centered cubic material that has been utilized by Chhabildas et al. [26] for the validation of high velocity impacts that formed the basis of the second stage of our validation simulations.

5.4.1 Taylor impact experiments on 6061-T6 Al

Figure 37 shows the ratio of the final lengths of Taylor cylinders to their initial lengths (L_f/L_0) for a number of Taylor impact tests. These ratios have been plotted as a function of the sum of the initial kinetic energy density and the initial internal energy density (relative to a fixed temperature of 294 K). The internal energy density has been added to shift the data according to temperature. The plot indicates the following:

(1) The ratio (L_f/L_0) is essentially independent of the initial length and diameter of the cylinder.
(2) There is a linear relationship between the ratio (L_f/L_0) and the initial kinetic energy density.
(3) As temperature increases, the absolute value of the slope of this line increases.

We have chosen to do detailed comparisons between experiment and simulation for the three tests marked with crosses on the figure. These tests represent situations in which fracture has not been observed in the cylinders and cover the range of temperatures of interest to us.

The ratio of the diameter of the deformed end to the original diameter (D_f/D_0) for some of these tests is plotted as a function of the energy density in Figure 38. A linear relation similar to that for the length is observed.

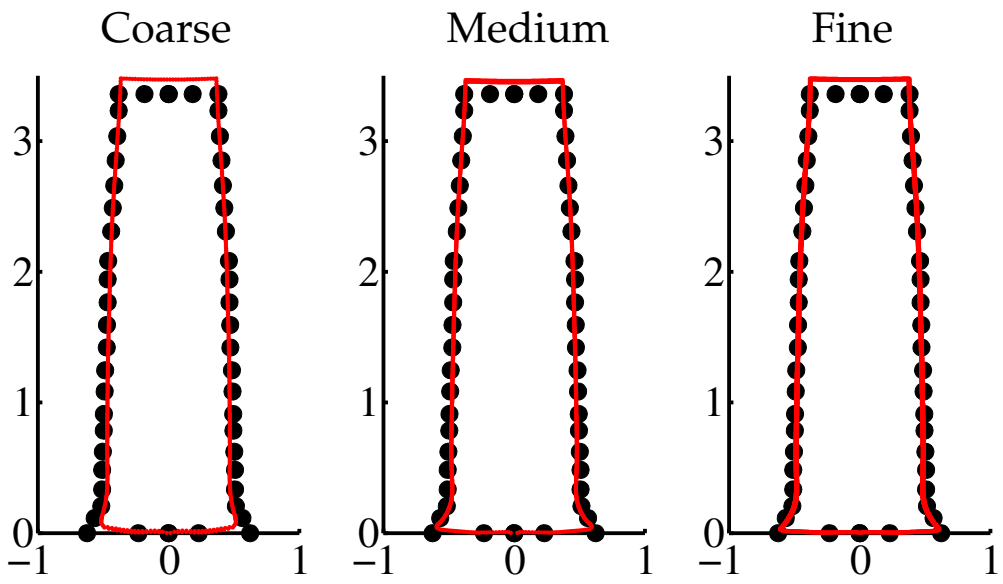

(a) With friction.

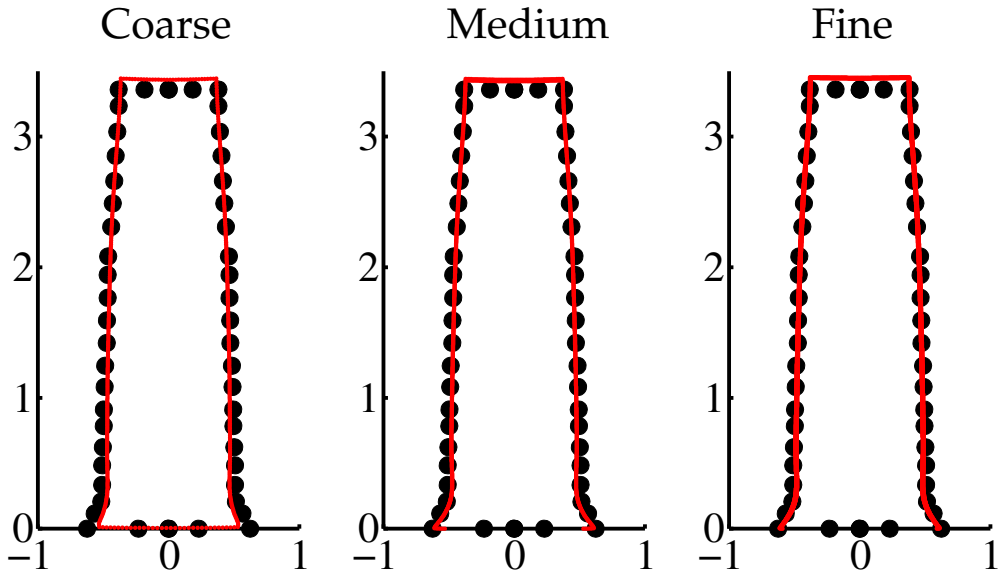

(b) Without friction.

Fig. 36. Effect of mesh refinement. Comparison of experimental and computed shapes of OFHC copper cylinder Cu-I using the Mechanical Threshold Stress (MTS) model. The axes are in cm. The circles represent experimental data. The solid lines represent the simulated profiles.

The length of the elastic zone at the end of the test is difficult to determine (especially for high strain rate and high temperature tests) and may not be a suitable metric for these conditions. This can be seen from the amount of variability in this metric shown in Figure 39.

Finally, the volume of the cylinder should be preserved during the Taylor test if isochoric plasticity holds. This metric can be used to determine the error in digitization of the profile of the cylinder if we assume isochoric behavior. Figure 40 shows the ratio of the final volume to the initial volume (V_f/V_0) as a function of the energy density. The volume is not preserved in any of the experiments. We attribute this error of 5% in the final volume to errors during the digitization of the profiles.

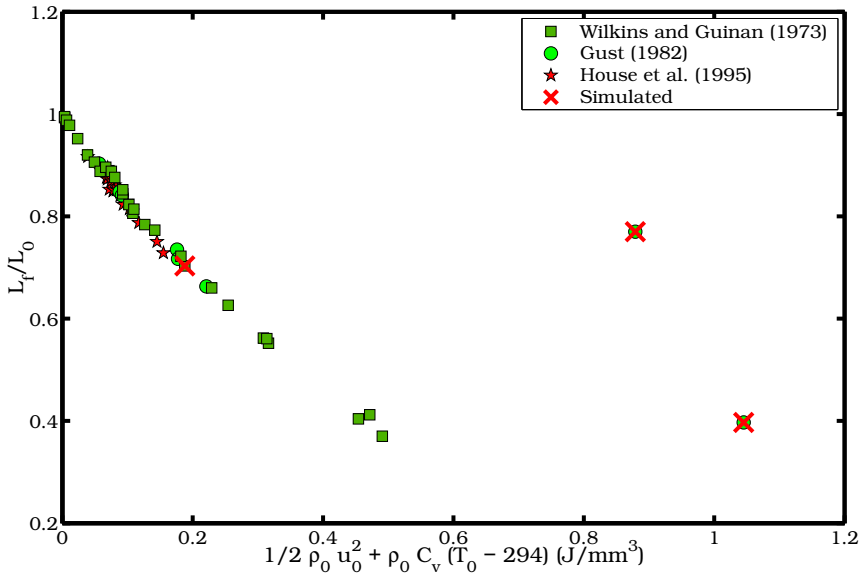

Fig. 37. Ratio of final length to initial length of 6061-T6 aluminum alloy Taylor cylinders for various conditions. The data are from Wilkins and Guinan [95], Gust [40], and House et al. [47].

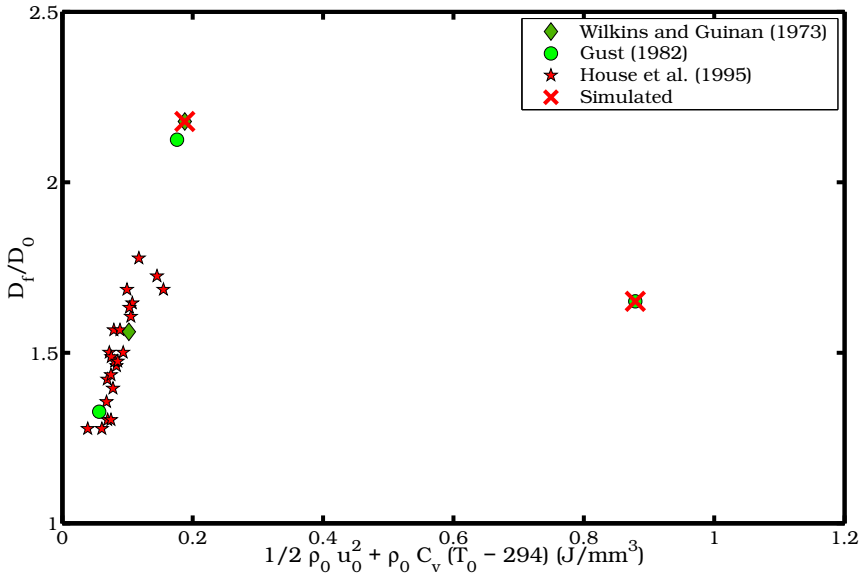

Fig. 38. Ratio of final length to initial length of 6061-T6 aluminum alloy Taylor cylinders for various conditions. The data are from Wilkins and Guinan [95], Gust [40], and House et al. [47].

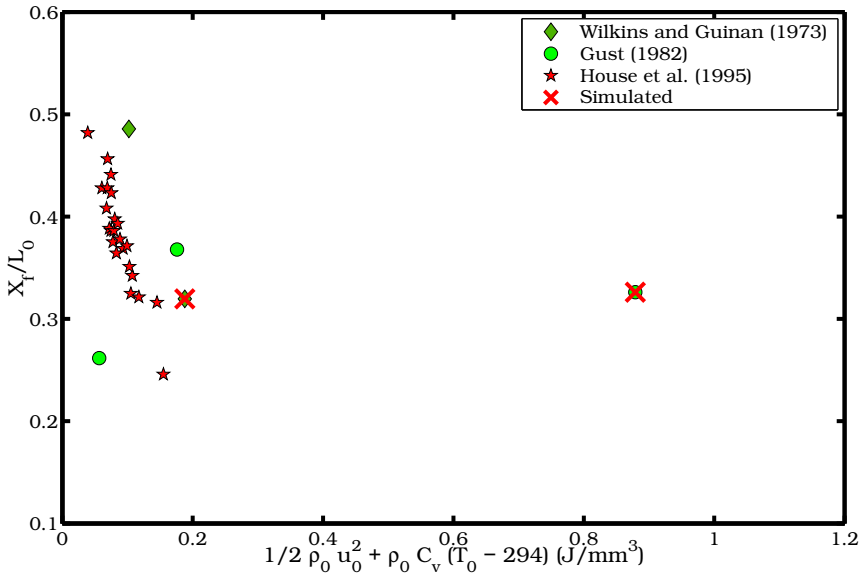

Fig. 39. Ratio of the length of the elastic zone to initial length of 6061-T6 aluminum alloy Taylor cylinders for various conditions. The data are from Wilkins and Guinan [95], Gust [40], and House et al. [47].

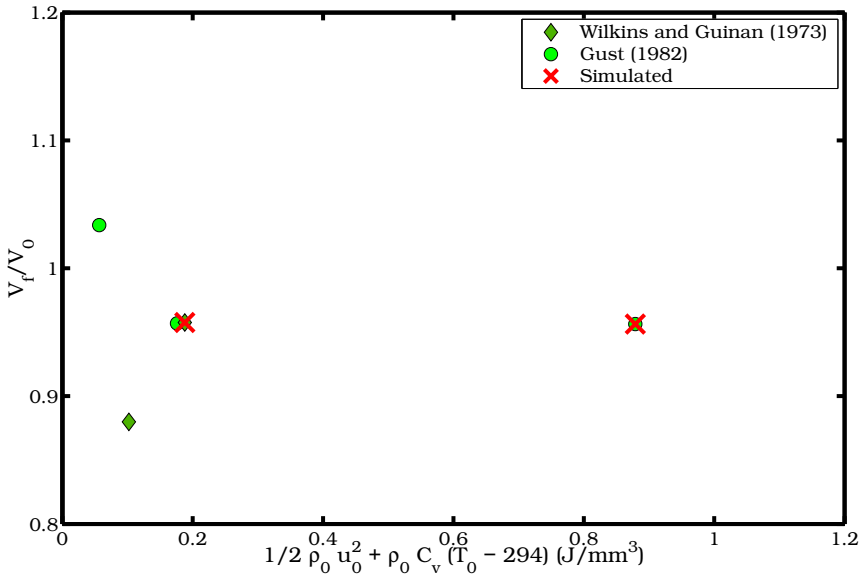

Fig. 40. Ratio of the final volume to initial volume of 6061-T6 aluminum alloy Taylor cylinders for various conditions. The data are from Wilkins and Guinan [95] and Gust [40].

Detailed comparisons have been provided for the tests marked with crosses in figures shown in this section. We have also simulated a few other tests, the details of which are not discussed in the interest of brevity.

Table 17
Initial data for 6061-T6 aluminum simulations.

Case	Material	Initial Length (L_0 mm)	Initial Diameter (D_0 mm)	Initial Velocity (V_0 m/s)	Initial Temperature (T_0 K)	Source
Al-A	6061-T6 Al	23.47	7.62	373	298	Wilkins and Guinan [95]
Al-B	6061-T6 Al	23.47	7.62	603	298	Wilkins and Guinan [95]
Al-C	6061-T6 Al	46.94	7.62	275	298	Wilkins and Guinan [95]
Al-D	6061-T6 Al	46.94	7.62	484	298	Wilkins and Guinan [95]
Al-E	6061-T6 Al	30	6.00	200	295	Gust [40]
Al-F	6061-T6 Al	30	6.00	358	295	Gust [40]
Al-G	6061-T6 Al	30	6.00	194	635	Gust [40]
Al-H	6061-T6 Al	30	6.00	354	655	Gust [40]

5.4.2 Taylor impact simulations of 6061-T6 Al

Table 17 shows the initial dimensions, velocity, and temperature of the specimens (along with the type of copper used and the source of the data) that we have simulated and compared with experimental data.

5.4.2.1 Comparison of plasticity models at room temperature. Comparisons between the computed and experimental profiles of 6061T6 aluminum alloy specimen Al-A are shown in Figure 41(a), (b), and (c). Those for specimen Al-C are shown in Figure 41(d), (e), and (f).

For the short cylinder, the final length is predicted accurately by all three models. However, the final mushroom diameter is underestimated by all the models. The difference in the predicted shapes is small and all the models do equally well.

For the long cylinder, the final length is underestimated by all three models while the mushroom diameter and the bulge are predicted accurately by all three. Once again, there is no significant difference between the three models.

If frictional contact at the impact surface is included, the final shapes of the specimens Al-A and Al-C are as shown in Figure 42.

The same final length as in the no friction case is predicted by all three models. However, the diameter of the mushroomed end is closer to the experimental value for cylinder Al-A. The Johnson-Cook model shows the largest value of the mushroom diameter while the MTS model predicts the smallest value. However, both values are larger than that for the simulations without friction. The turned-up ends

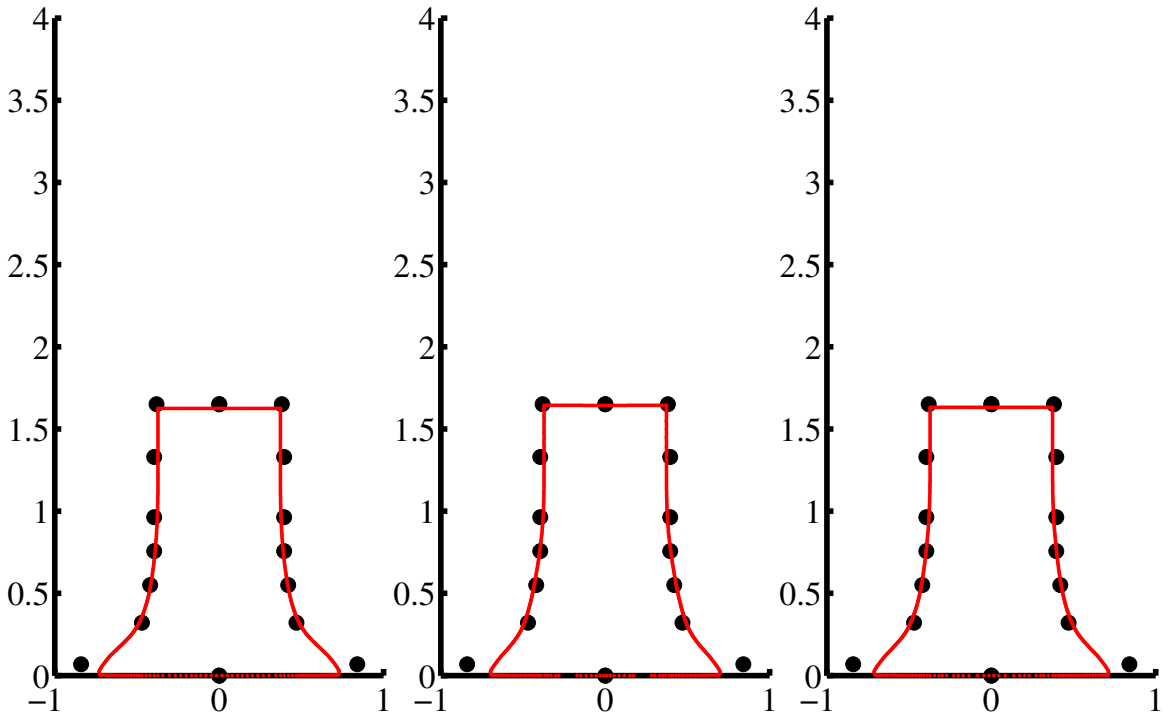

(a) JC (Al-A). (b) MTS (Al-A). (c) SCGL (Al-A).

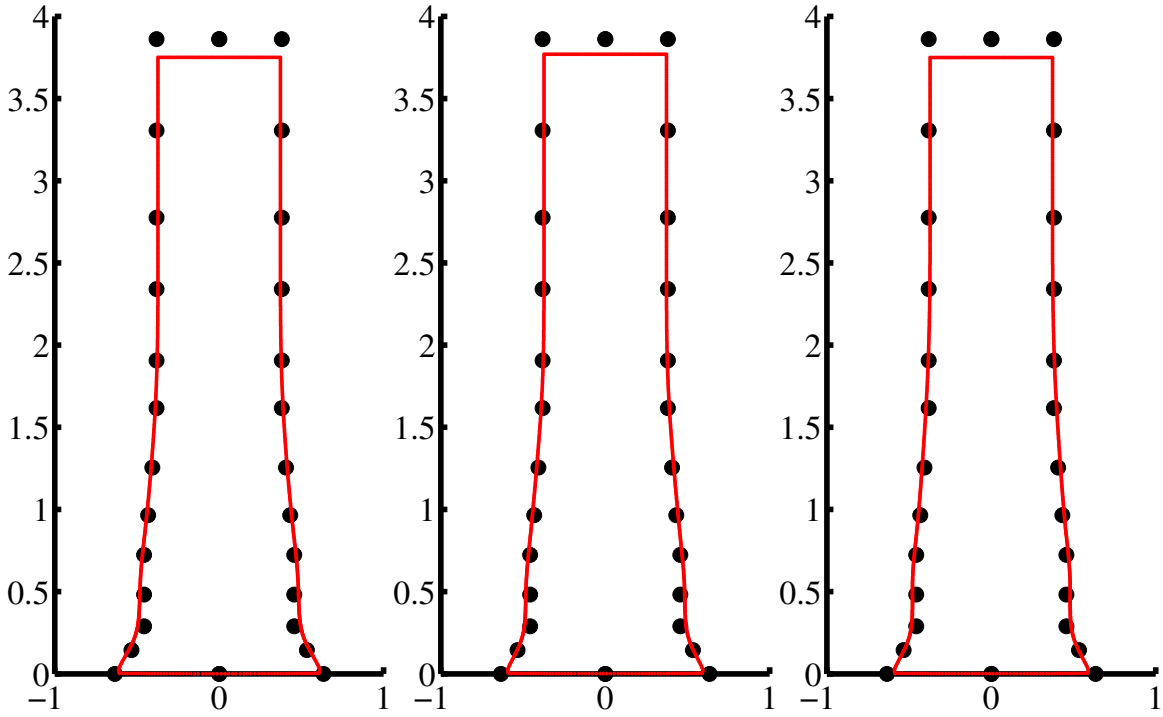

(d) JC (Al-C). (e) MTS (Al-C). (f) SCGL (Al-C).

Fig. 41. Comparison of experimental and computed shapes of 6061T6 aluminum cylinders Al-A and Al-C using the Johnson-Cook (JC), Mechanical Threshold Stress (MTS), and Steinberg-Cochran-Guinan-Lund (SCGL) plasticity models. The axes are shown in cm units. The circles represent experimental data. The solid lines represent the simulated profiles.

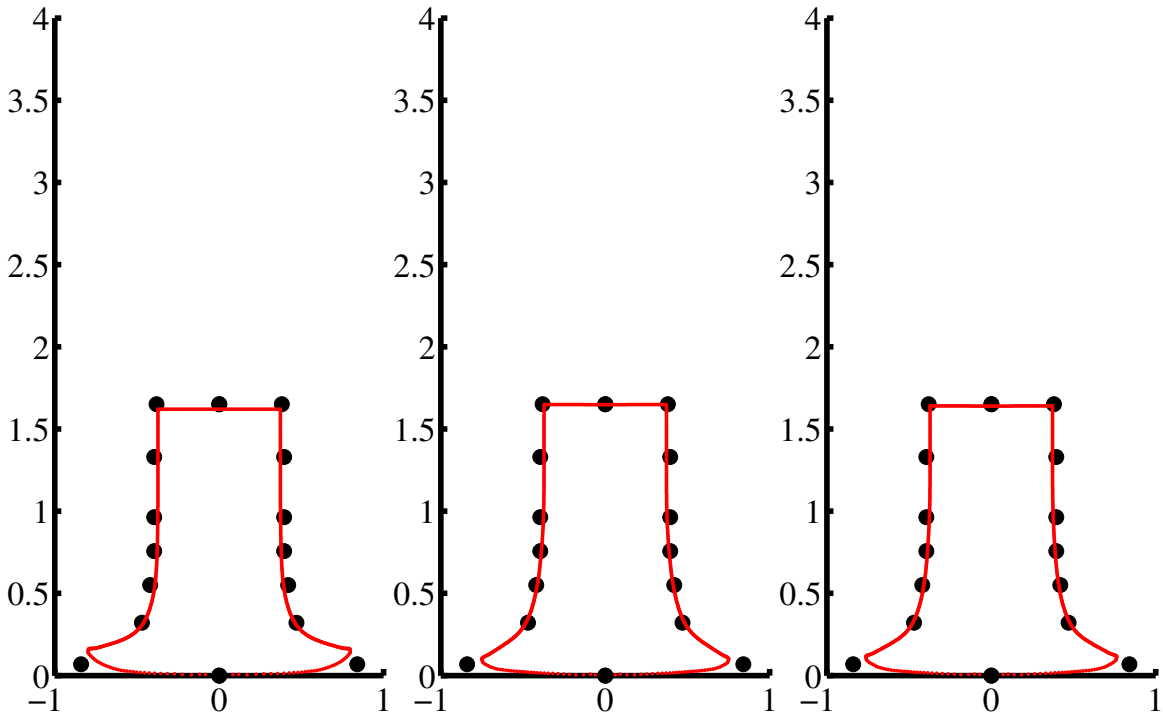

(a) JC (Al-A). (b) MTS (Al-A). (c) SCGL (Al-A).

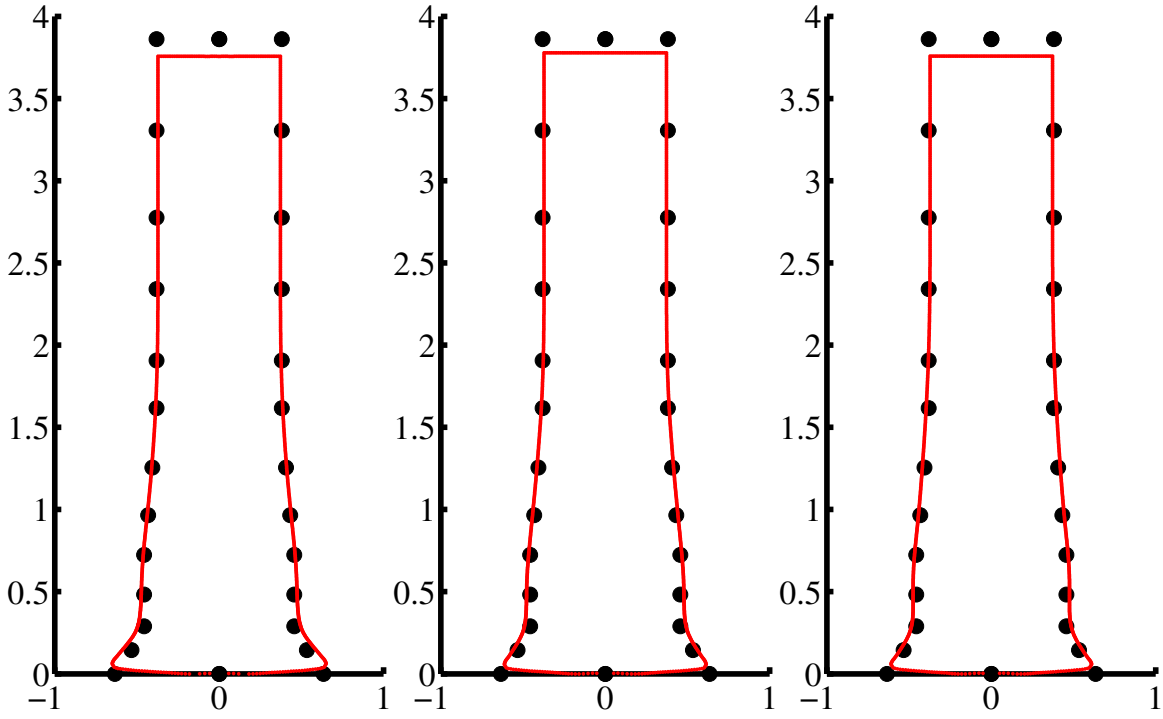

(a) JC (Al-C). (b) MTS (Al-C). (c) SCGL (Al-C).

Fig. 42. Effect of frictional contact between the 6061-T6 Al specimen and the anvil. The plots show the experimental and computed shapes of 6061T6 aluminum cylinders Al-A and Al-C. The profiles have been computed using the Johnson-Cook (JC), Mechanical Threshold Stress (MTS), and Steinberg-Cochran-Guinan-Lund (SCGL) plasticity models. The axes are shown in cm units. The circles represent experimental data. The solid lines represent the simulated profiles.

are also quite prominent for Al-A because of the larger initial velocity. The effect of friction is much smaller for cylinder Al-C.

We conclude that room temperature experiments can be predicted accurately by all the models. Hence, in simulations at room temperature, the least expensive model (the Johnson-Cook model in this case) should be used. Contact friction should also be included, if appropriate, for more realistic simulations.

5.4.2.2 Comparison of plasticity models at high temperature. At higher temperatures, the response of the three plasticity models is quite different. Comparisons between the computed and experimental profiles of 6061T6 aluminum alloy specimen Al-G are shown in Figure 43(a), (b), and (c). Those for specimen Al-H are shown in Figure 43(d), (e), and (f). Note that we have used frictional contact in these simulations with a coefficient of friction of 0.0002 between the cylinder and the anvil.

The profile predicted by the Johnson-Cook model for cylinder Al-G shows that:

(1) the final length is predicted accurately,
(2) the mushroom diameter is predicted accurately, and
(3) the bulge is underestimated indicating that the model underestimates strain hardening at 635 K.

The MTS model overestimates the final length and underestimates the mushroom diameter. This indicates that the parameters used for the Model (which were for an aluminum alloy with 1% magnesium) (Puchi-Cabrera et al. [73]) are not accurate enough to be used to model 6061-T6 Al. Both the MTS model and the SCGL model underestimate the mushroom diameter - indicating that the predicted yield stress is too high

For cylinder Al-H, the nominal strain rate is around 12,000 /s (around double that for cylinder Al-G). In this case, the final length predicted by the Johnson-Cook model is the closest to experiment. In addition, the JC model shows a pronounced curvature in the mushroomed end of the cylinder. We cannot decide the accuracy of the simulation because the final profile for this test is not available for comparison with the predicted profile.

On the other hand, the final lengths predicted by both the MTS and the SCGL model are more than 80% larger than the experimental value. This indicates that the temperature dependence of the yield stress is not modeled accurately by these models. Recalibration of the models is required if simulations at high temperatures and high strain rates are to be performed for 6061-T6 Al alloy.

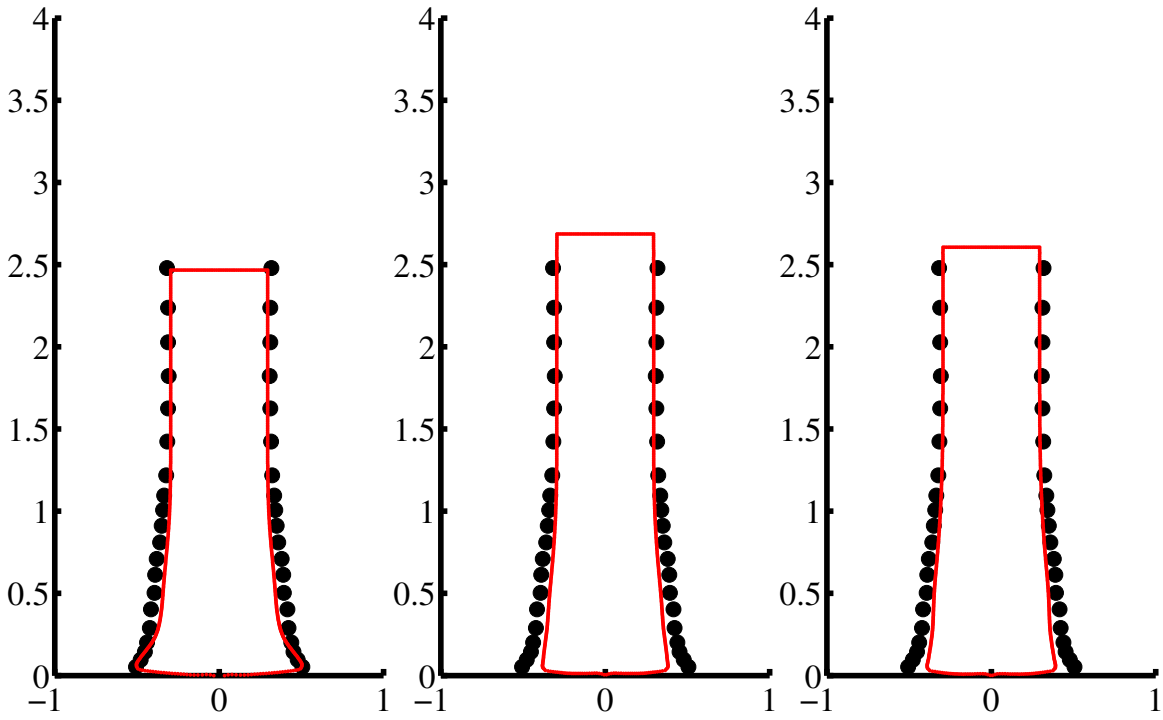

(a) JC (Al-G). (b) MTS (Al-G). (c) SCGL (Al-G).

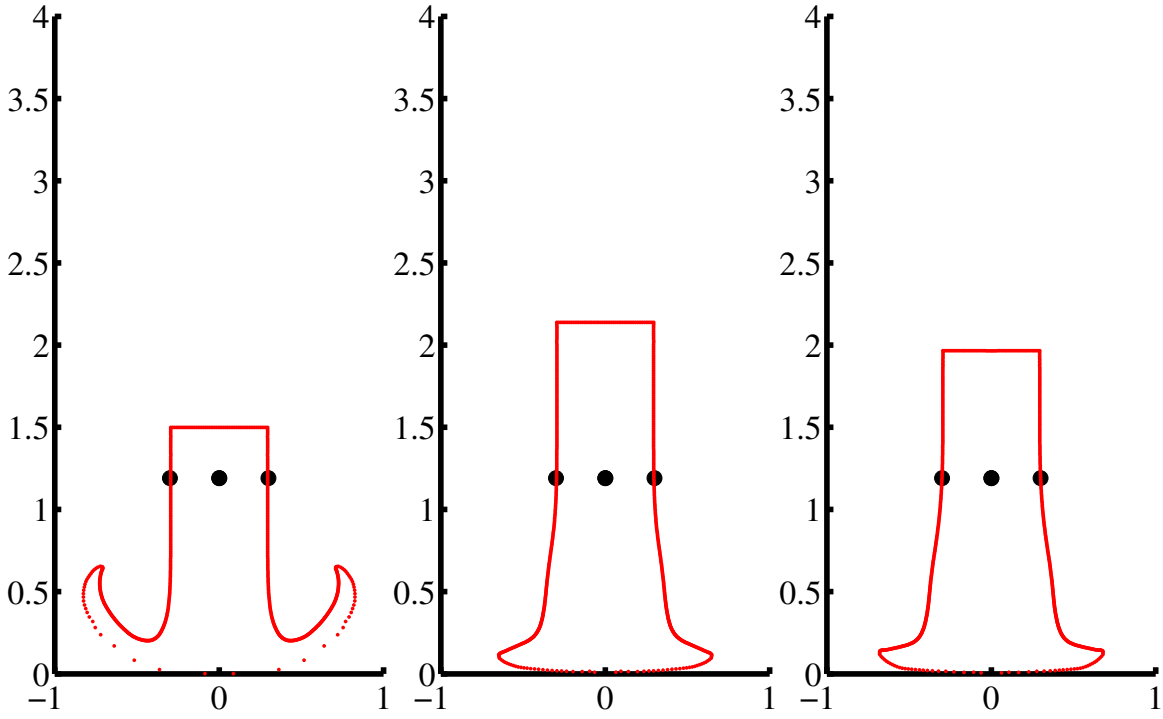

(a) JC (Al-H). (b) MTS (Al-H). (c) SCGL (Al-H).

Fig. 43. High temperature Taylor impact simulations. Comparison of experimental and computed shapes of 6061T6 aluminum cylinders Al-G and Al-H using the Johnson-Cook (JC), Mechanical Threshold Stress (MTS), and Steinberg-Cochran-Guinan-Lund (SCGL) plasticity models. The axes are shown in cm units. The circles represent experimental data. The solid lines represent the simulated profiles.

5.4.2.3 Comparisons between MPM and FEM. To determine how our MPM simulations compare with FEM simulations we have run two high temperature aluminum impact tests using LS-DYNA (with the coupled structural-thermal option). Figure 44 shows the final deformed shapes for the two cases from the MPM and FEM simulations using Johnson-Cook plasticity. Note that the FEM simulations have been performed with under-integrated elements and hourglass control.

The FEM simulations overestimate the final length and underestimate the mushroom diameter for cylinder Al-G. For cylinder Al-H, the final length predicted by FEM is more than 80% larger than the experimental value. The FEM prediction for model Al-G can be with adaptive mesh refinement at the highly deformed regions. It is unlikely that standard displacement or hybrid finite elements are capable of simulating cylinder Al-H without significant remeshing.

5.4.2.4 Taylor impact simulations with particle erosion. Since the MTS and SCG model predicted very stiff responses for the cylinders, we thought that it was possible that the cylinders were actually failing. This section presents simulations that include failure of MPM particles. The approach and models used to simulate particle failure are discussed in Appendix D.

Figure 45 shows Taylor impact profiles for cases Al-G and Al-H with particle erosion. If we compare these profiles with the simulated profiles without failure (Figure 43), we notice that there is essentially no difference for cylinder Al-G. However, we do notice some differences in the computed profiles for cylinder Al-H.

The profile predicted by the Johnson-Cook model for cylinder Al-H shows some necking of the mushroomed end that is not present in the simulation without failure. Interestingly, failure of particles does not cause the diameter of the mushroom to increase - instead we see a significant decrease in the final mushroom diameter. Finally, the deformed length of the cylinder does not appear to be affected by particle failure which occurs mostly at the highly strained region near the center of the base.

We conclude that it is the material model rather than failure that gives us stiffer responses for cylinder Al-H that experiments suggest. The models need to be recalibrated for the regime of strain rates and temperatures involved in this test.

5.4.2.5 Effect of mesh refinement. It could be suggested that the stiff response of the MTS and SCGL models are due to lack of convergence and that further mesh refinement is required. In this section we show the effect of mesh refinement on the response of cylinder Al-H with the Johnson-Cook model. Similar effects have been observed for the MTS and SCGL models and the conclusions are similar (though the mesh dependence is not as pronounced for these models).

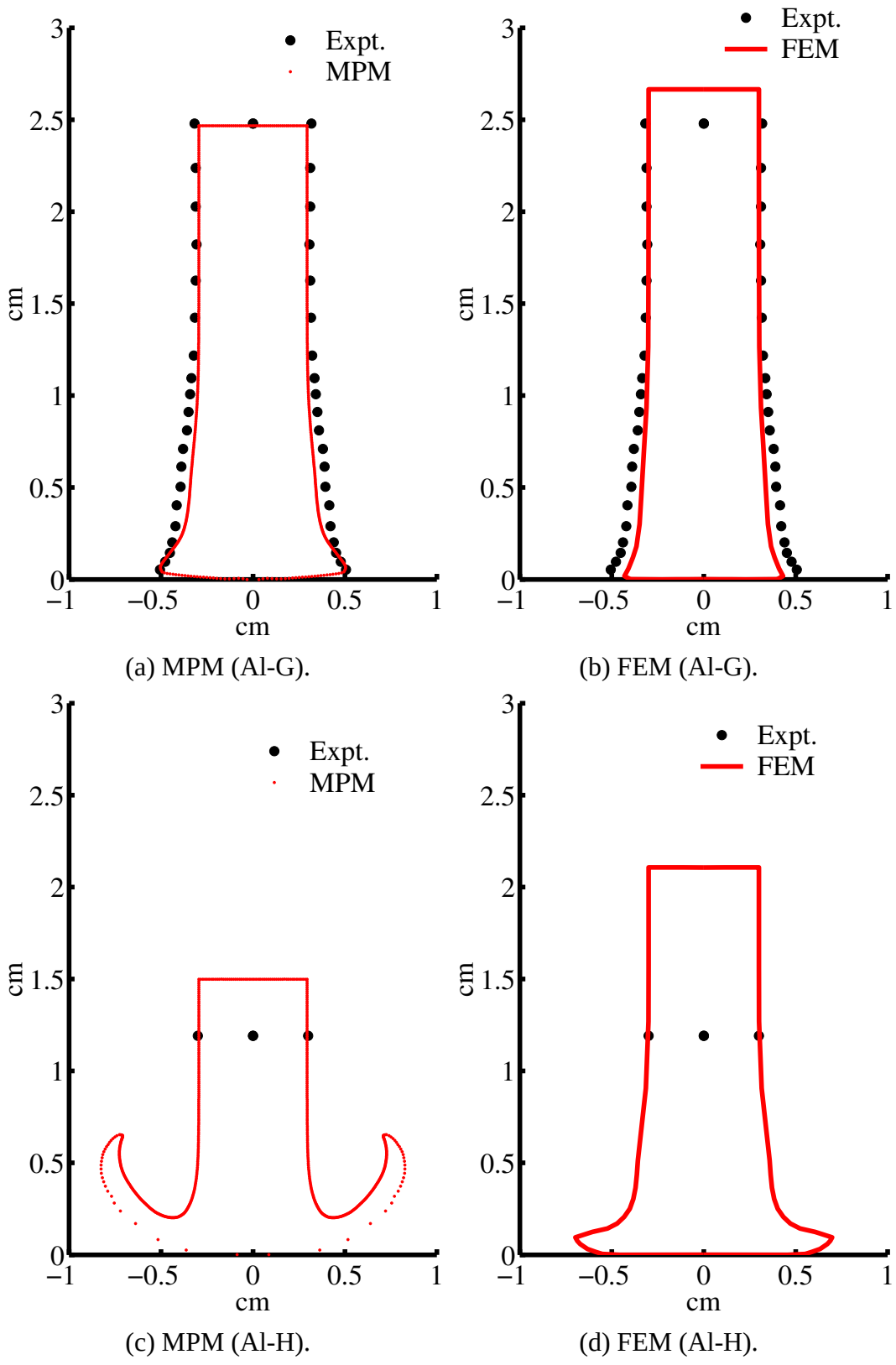

(a) MPM (Al-G). (b) FEM (Al-G).

(c) MPM (Al-H). (d) FEM (Al-H).

Fig. 44. Comparison of experimental and computed shapes of 6061T6 aluminum cylinders Al-G and Al-H using MPM and FEM and the Johnson-Cook plasticity model. The axes are in cm. The circles represent experimental data. The solid lines represent the simulated profiles.

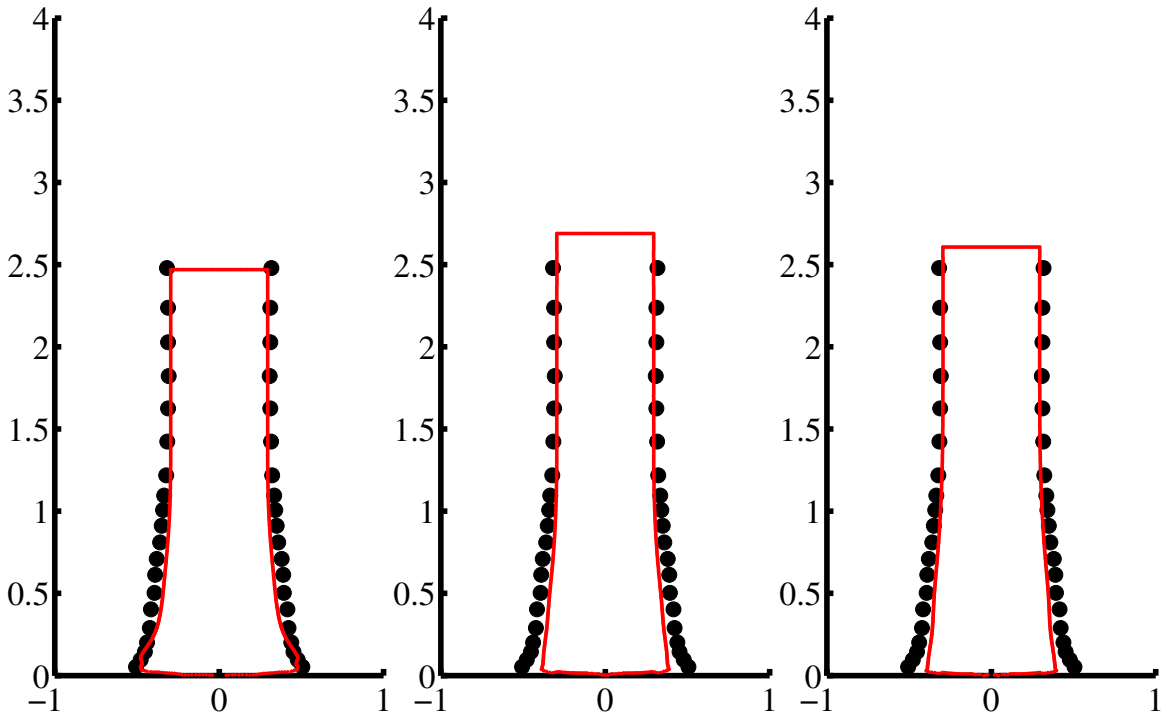

(a) JC (Al-G). (b) MTS (Al-G). (c) SCGL (Al-G).

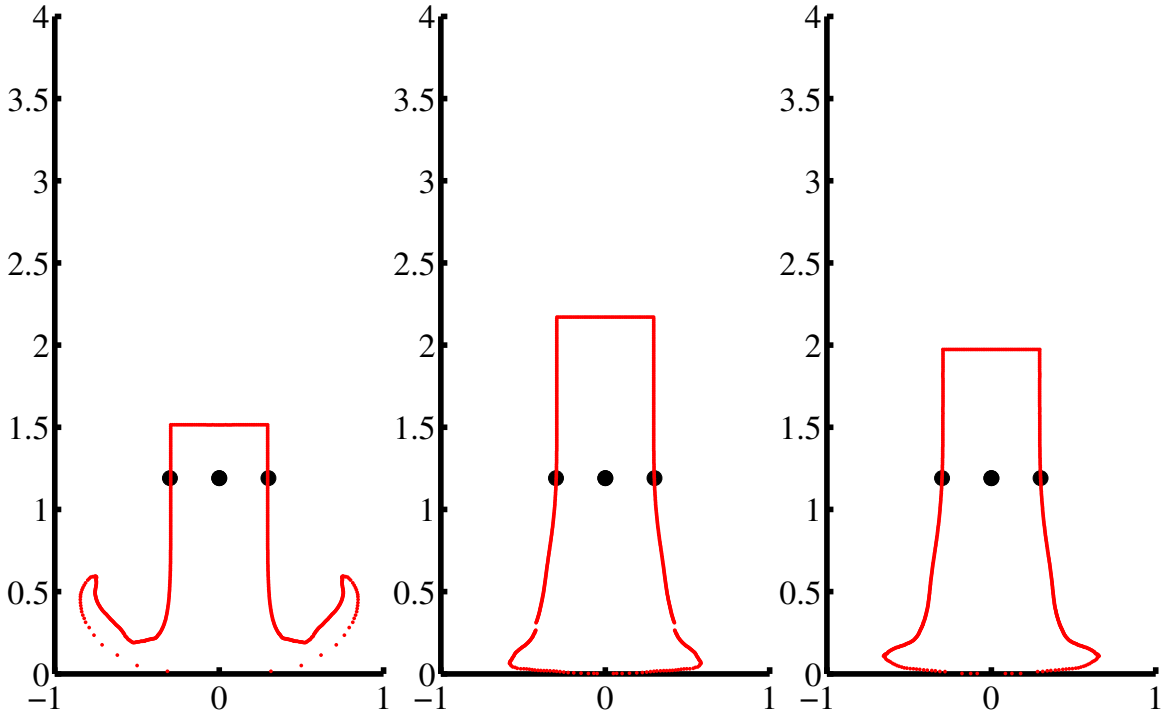

(a) JC (Al-H). (b) MTS (Al-H). (c) SCGL (Al-H).

Fig. 45. Effect of including particle failure. Comparison of experimental and computed shapes of 6061T6 aluminum cylinders using the Johnson-Cook (JC), Mechanical Threshold Stress (MTS), and Steinberg-Cochran-Guinan (SCG) plasticity models with particle erosion. The axes are shown in cm units. The circles represent experimental data. The solid lines represent the simulated profiles.

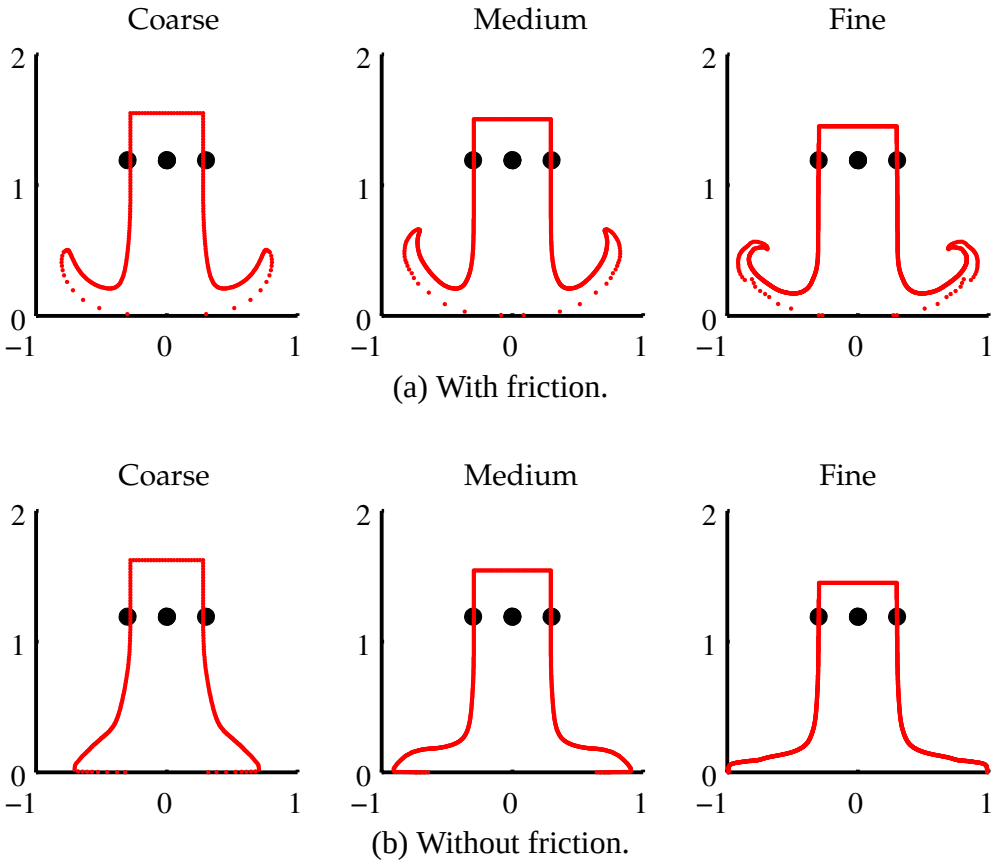

Fig. 46. Effect of mesh refinement. Comparison of experimental and computed shapes of 6061T6 aluminum cylinder Al-H using the Johnson-Cook (JC) model with increasing mesh refinement. The axes are in cm. The circles represent experimental data. The solid lines (and dots) represent the simulated profiles.

The coarse mesh has a grid spacing of 0.64 mm, the medium mesh has a grid spacing of 0.32 mm, and the fine mesh has a spacing of 0.16 mm. The number of particles per grid cell is 27 and a 27 node GIMP interpolation is used to move information from particles to the grid and vice versa.

Simulations of impact case Al-H with increasing mesh refinement are shown in Figure 46. We show both simulations with friction (Figure 46(a)) and without friction (Figure 46(b)) between the cylinder and the anvil.

If we look at the simulations with friction, we notice that as the mesh is refined the final length of the cylinder decreases and the mushroom shape changes (becomes thinner). The reason for this mesh dependence becomes obvious when we look at the spacing between particles. Due to the large deformation at the base, the particle spacing becomes larger than the zone of influence of the GIMP interpolation functions. Particles cease to see nearby neighbors at this stage. As the number of particles increases with mesh refinement, particles continue to interact with neighbors up to a late stage in the simulation. A solution to this problem is adaptive particle

addition in highly deformed regions so that particles do not cease to interact via the grid. Further work is needed to resolve this issue.

The same holds for the simulations without friction, except that the deformed end of the cylinder tends to flow along the surface of the anvil instead of rebounding back in the form of a true mushroom.

Our overall observations from the tests on 6061-T6 Al alloy are:

(1) All three models perform well at room temperature. The Johnson-Cook model is preferable at these temperatures because of the computational efficiency of the model.
(2) At high temperatures, the MTS and SCGL models predict a stiffer response than experiments suggest. These models have to be recalibrated for these temperatures.
(3) There is some mesh dependence for the Johnson-Cook model at high temperatures due to excessive deformation of the Taylor cylinder. Adaptive particle addition may be required (in highly deformed zones) to resolve this issue.

5.5 Taylor tests on 4340 steel

In this section we present the results from Taylor tests on 4340 steel specimens for different initial temperatures and impact velocities. More detailed comparisons for 4340 steel can be found elsewhere (Banerjee [10]).

5.5.1 Taylor impact experiments on 4340 steel

Figure 47 shows the ratio of the final lengths of Taylor cylinders to their initial lengths (L_f/L_0) for a number of Taylor impact tests. These ratios have been plotted as a function of the sum of the initial kinetic energy density and the initial internal energy density (relative to a fixed temperature of 294 K). The internal energy density has been added to shift the data according to temperature. The plot indicates the following:

(1) The ratio (L_f/L_0) is essentially independent of the initial length and diameter of the cylinder.
(2) There is a linear relationship between the ratio (L_f/L_0) and the initial kinetic energy density.
(3) As temperature increases, the absolute value of the slope of this line increases.

We have chosen to do detailed comparisons between experiment and simulation for the three tests marked with crosses on the figure. These tests represent situations in which fracture has not been observed in the cylinders and cover the range of

temperatures of interest to us.

The ratio of the diameter of the deformed end to the original diameter (D_f/D_0) for some of these tests is plotted as a function of the energy density in Figure 48. A linear relation similar to that for the length is observed.

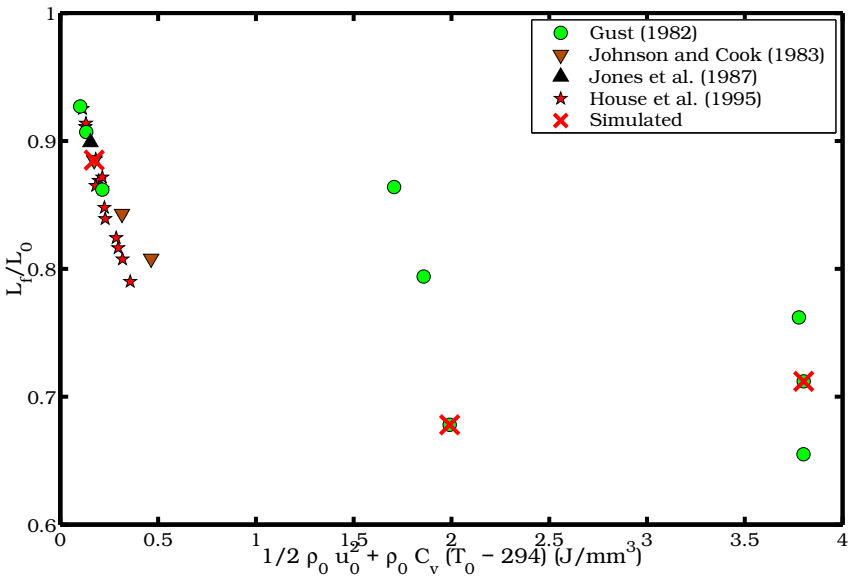

Fig. 47. Ratio of final length to initial length of 4340 steel Taylor cylinders for various conditions. The data are from Gust [40], Johnson and Cook [49], Jones and Gillis [53], and House et al. [47].

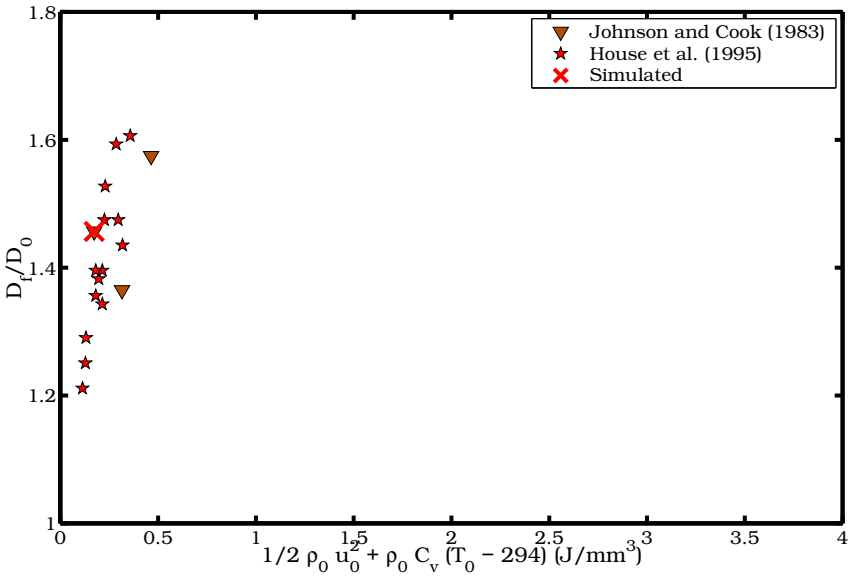

Fig. 48. Ratio of final length to initial length of 4340 steel Taylor cylinders for various conditions. The data are from Johnson and Cook [49], and House et al. [47].

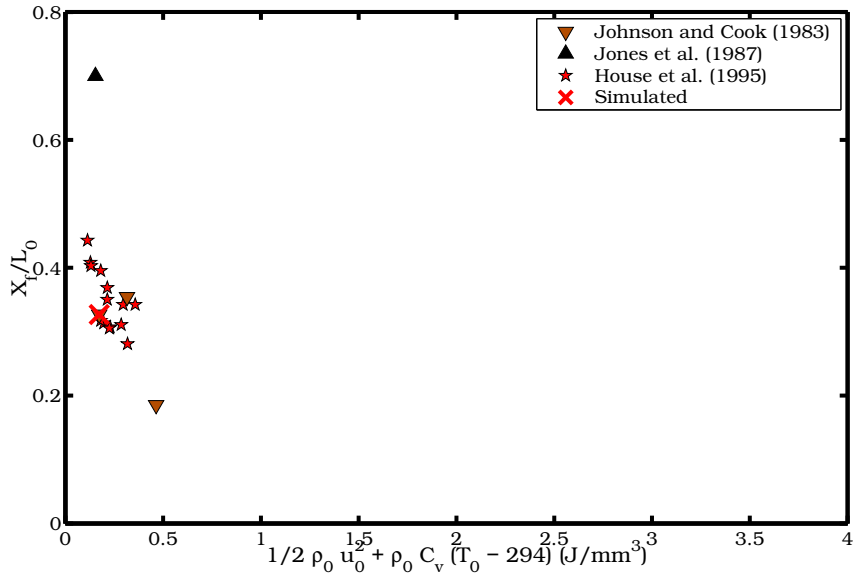

Fig. 49. Ratio of the length of the elastic zone to initial length of 4340 steel Taylor cylinders for various conditions. The data are from Johnson and Cook [49], Jones and Gillis [53], and House et al. [47].

The length of the elastic zone at the end of the test is difficult to determine (especially for high strain rate and high temperature tests) and may not be a suitable metric for these conditions. This can be seen from the amount of variability in this metric shown in Figure 49.

Finally, the volume of the cylinder should be preserved during the Taylor test if isochoric plasticity holds. This metric can be used to determine the error in digitization of the profile of the cylinder if we assume isochoric behavior. Figure 50 shows the ratio of the final volume to the initial volume (V_f/V_0) as a function of the energy density. The volume is not preserved in any of the experiments. We attribute this error to inaccuracies in the digitization of the profiles.

Detailed comparisons have been provided for the tests marked with crosses in figures shown in this section. We have also simulated a few other tests, the details of which are not discussed in the interest of brevity.

5.5.2 Taylor impact simulations of 4340 steel

Table 18 shows the initial dimensions, velocity, and temperature of the specimens (along with the type of copper used and the source of the data) that we have simulated and compared with experimental data.

5.5.2.1 Performance of plasticity models at room temperature. Figure 51 shows the simulated profile of case St-G without friction. The Johnson-Cook model

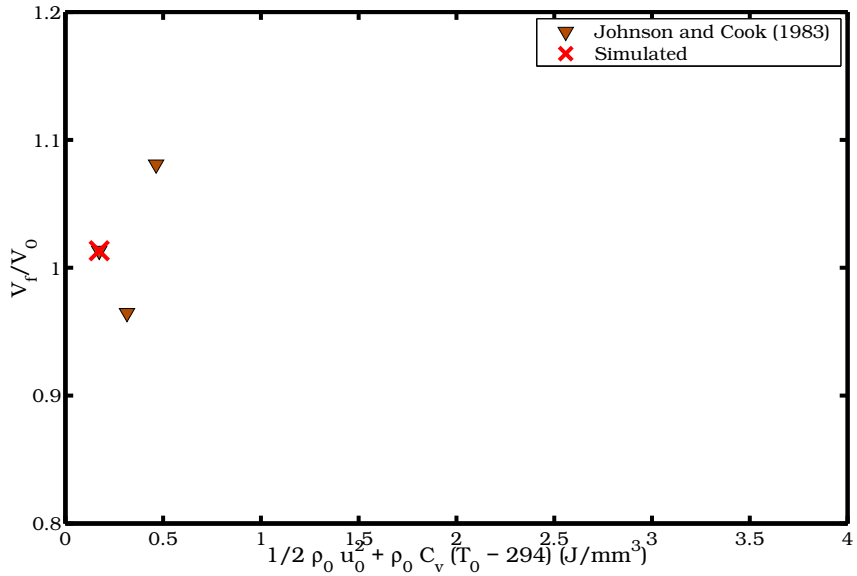

Fig. 50. Ratio of the final volume to initial volume of 4340 steel Taylor cylinders for various conditions. The data are from Wilkins and Guinan [95] and Gust [40].

predicts the profile quite accurately. We have observed the same behavior for the SCGL model for this case. Similar behavior is observed for the other room temperature simulations. We conclude that room temperature deformations are quite accurately modeled by both models.

Table 18
Initial data for 4340 steel simulations.

Case	Hardness	Initial Length (L_0 mm)	Initial Diameter (D_0 mm)	Initial Velocity (V_0 m/s)	Initial Temperature (T_0 K)	Source
St-A	$R_c = 40$	30	6.00	158	295	Gust [40]
St-B	$R_c = 40$	30	6.00	232	295	Gust [40]
St-C	$R_c = 40$	30	6.00	183	715	Gust [40]
St-D	$R_c = 40$	30	6.00	312	725	Gust [40]
St-E	$R_c = 40$	30	6.00	136	1285	Gust [40]
St-F	$R_c = 40$	30	6.00	160	1285	Gust [40]
St-G	$R_c = 30$	25.4	7.62	208	298	Johnson and Cook [49]
St-H	$R_c = 30$	12.7	7.62	282	298	Johnson and Cook [49]
St-I	$R_c = 30$	8.1	7.62	343	298	Johnson and Cook [49]

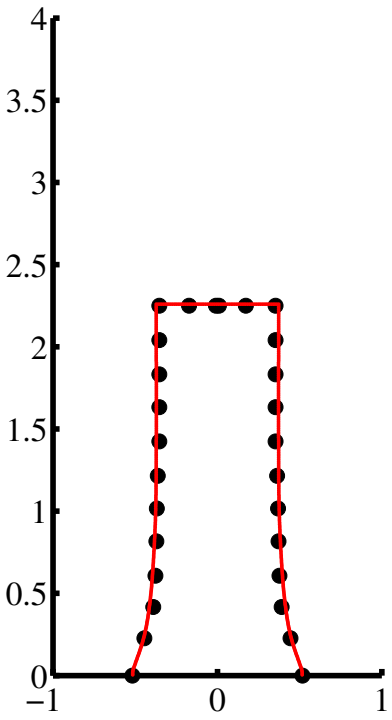

Fig. 51. Comparison of experimental and computed shapes of 4340 steel cylinder St-G without friction. The profile has been computed with the Johnson-Cook (JC) model. The Steinberg-Cochran-Guinan-Lund (SCGL) model gives the same profile. The axes are in cm. The circles represent experimental data. The solid lines represent the simulated profiles.

5.5.2.2 Performance of plasticity models at high temperatures. Figure 52 shows the simulated profile of cases St-D and St-F (with friction). Sample St-D has an initial temperature of 718 K while sample St-F has an initial temperature of 1285 K. The nominal strain rate for sample St-D is almost twice that of sample St-F.

The Johnson-Cook model predicts the final length of St-D quite accurately. However, the SCGL model predicts an extremely low value of the yield stress at this temperature and the cylinder flows until the ends deflect from the walls of the computational domain. This indicates that the strain rate dependence of the steel at high temperatures is not predicted accurately by the SCGL model for 4340 steel (source [40]).

On the other hand, the SCGL model predicts the correct final length of the cylinder St-F while the JC model overestimates the length by 15%. In this case, it is the JC model that has to be recalibrated.

These observations are true for the other tests at high temperatures.

5.5.2.3 Taylor impact simulations with particle failure. Figure 53 shows Taylor impact simulations for cases St-D and St-F with particle failure. We see that

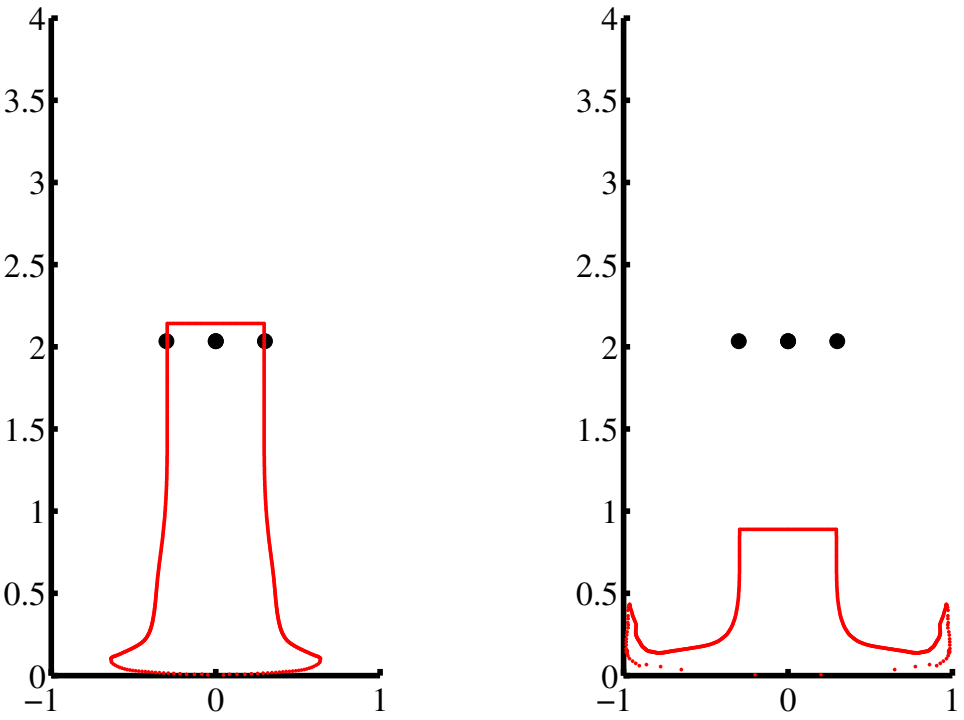

(a) JC (St-D).

(b) SCGL (St-D).

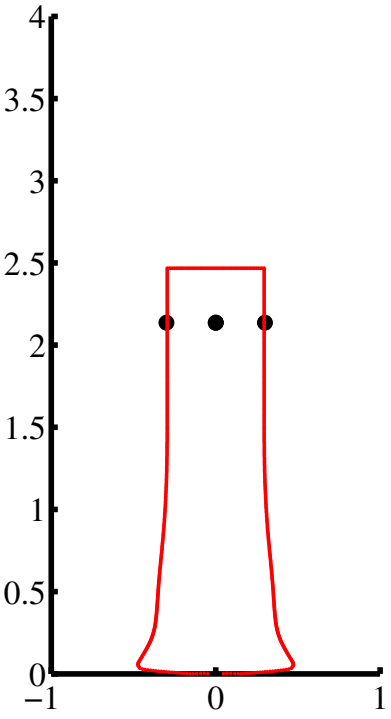

(c) JC (St-F).

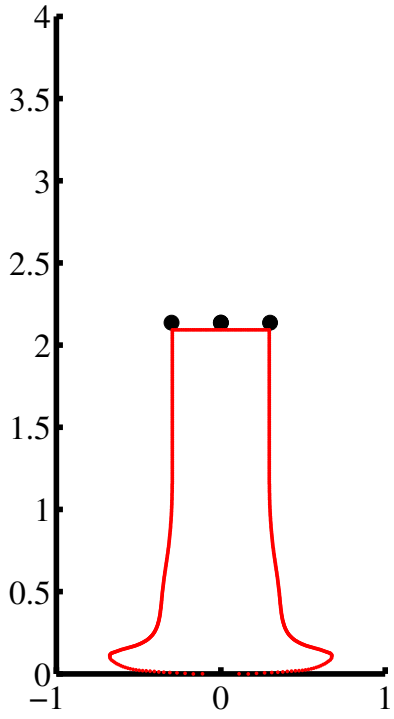

(d) SCGL (St-F).

Fig. 52. Comparison of experimental and computed shapes of 4340 steel cylinders St-D and St-F with friction. The profiles have been computed with the Johnson-Cook (JC) and the Steinberg-Cochran-Guinan-Lund (SCGL) models. The axes are in cm. The circles represent experimental data. The solid lines represent the simulated profiles.

particle failure does not significantly affect the final length or the overall behavior of the cylinders in these experiments. We expect to observe more complex failure behavior at higher velocity impacts. However, we have not simulated any such tests.

In summary:

(1) Both models have to be recalibrated for high temperature-high strain rate simulations.
(2) The Johnson-Cook model parameters (Johnson and Cook [49]) for 4340 steel are accurate at room temperature. At high temperatures, the strain rate dependence of softening of the steel is not represented adequately by the JC model. However, the Johnson-Cook model performs better at high strain rates than the SCG model (at high temperatures).
(3) The lack of rate dependence at high strain rates that is assumed by the SCGL model is a weakness that shows up in the simulation of cylinder St-D.

6 Final Remarks

We have performed detailed validation experiments for copper, 6061-T6 aluminum, and 4340 steel to determine how the models implemented in the UINTAH code perform at high temperatures and high strain rates. We observe that all the plasticity models predict similar stress-strain behavior at room temperature and this is reflected in the Taylor impact test profiles.

At high temperatures and relatively low strain rates, all models perform well provided that they are calibrated for those conditions. None of the models do well when the conditions include very high temperatures and strain rates greater that 10^5 /s when simulating three-dimensional problems.

We suggest that care be exercised when choosing one of the models discussed in this paper and that the models be recalibrated for the range of conditions of interest.

Acknowledgments

This work was supported by the the U.S. Department of Energy through the Center for the Simulation of Accidental Fires and Explosions, under grant W-7405-ENG-48.

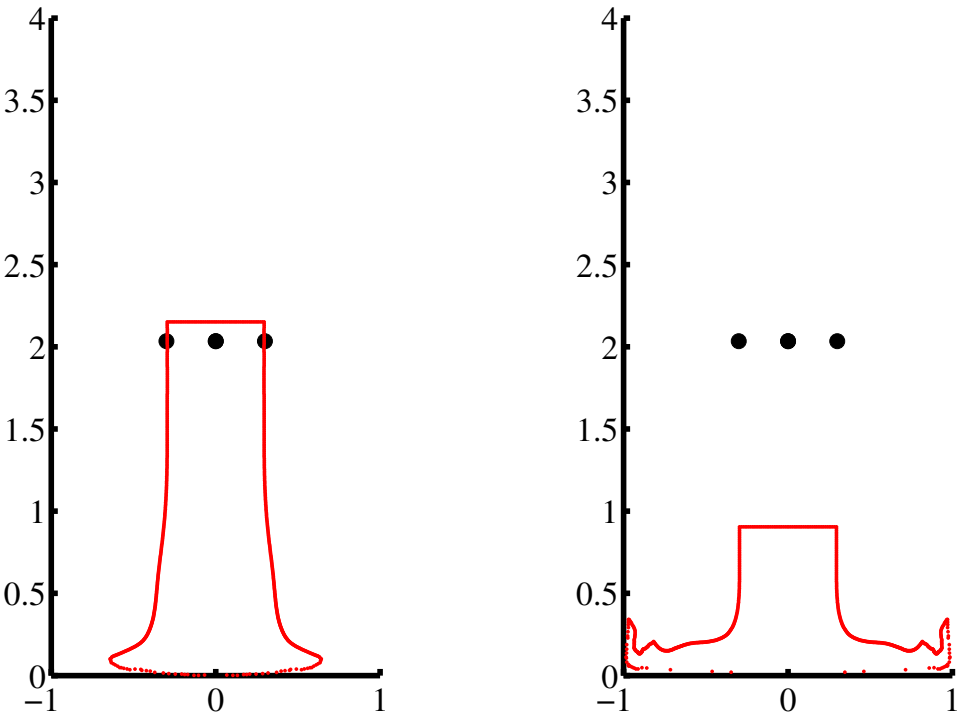

(a) JC (St-D).

(b) SCGL (St-D).

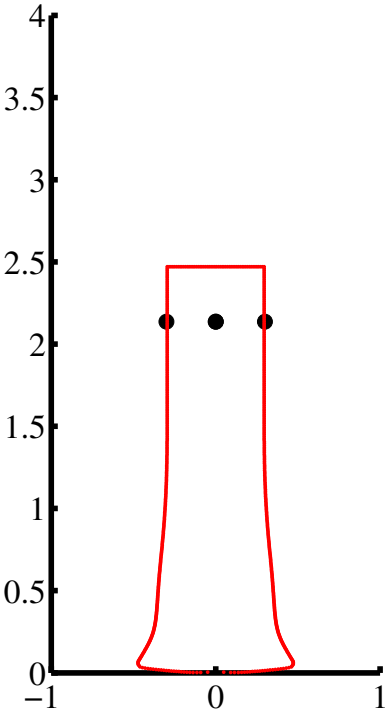

(c) JC (St-F).

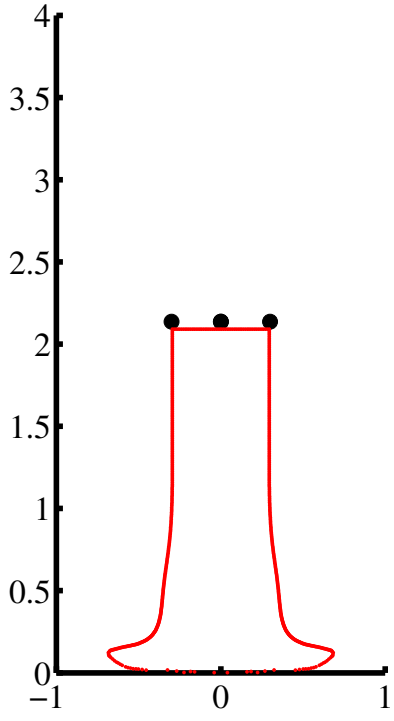

(d) SCGL (St-F).

Fig. 53. Effect of particle erosion. Comparison of experimental and computed shapes of 4340 steel cylinders St-D and St-F using the Johnson-Cook (JC) and Steinberg-Cochran-Guinan-Lund (SCGL) plasticity models with particle erosion. The axes are in cm. The circles represent experimental data. The solid lines represent the simulated profiles.

REFERENCES

[1] Abed, F. H., Voyiadjis, G. Z., 2005. A consistent modified Zerilli-Armstrong flow stress model for bcc and fcc metals for elevated temperatures. Acta Mechanica 175, 1–18.

[2] Addessio, F. L., Johnson, J. N., Maudlin, P. J., 1993. The effect of void growth on Taylor cylinder impact experiments. J. Appl. Phys. 73 (11), 7288–7297.

[3] Armstrong, R., Gammon, D., Geist, A., Keahey, K., Kohn, S., McInnes, L., Parker, S., Smolinski, B., 1999. Toward a Common Component Architecture for high-performance scientific computing. In: Proc. 1999 Conference on High Performance Distributed Computing.

[4] Babuska, I., Oden, J. T., 2004. Verification and validation in computational engineering and science: basic concepts. Comput. Methods Appl. Mech. Engrg. 193, 4057–4066.

[5] Bancroft, D., Peterson, E. L., Minshall, S., 1956. Polymorphism of iron at high pressure. J. Appl. Phys 27 (3), 291–298.

[6] Banerjee, B., 2004. Material point method simulations of fragmenting cylinders. In: Proc. 17th ASCE Engineering Mechanics Conference (EM2004). Newark, Delaware.

[7] Banerjee, B., 2004. MPM validation: Sphere-cylinder impact: Low resolution simulations. Tech. Rep. C-SAFE-CD-IR-04-002, Center for the Simulation of Accidental Fires and Explosions, University of Utah, USA.

[8] Banerjee, B., 2004. MPM validation: Sphere-cylinder impact: Medium resolution simulations. Tech. Rep. C-SAFE-CD-IR-04-003, Center for the Simulation of Accidental Fires and Explosions, University of Utah, USA.

[9] Banerjee, B., 2004. MPM validation: Sphere-cylinder impact tests: Energy balance. Tech. Rep. C-SAFE-CD-IR-04-001, Center for the Simulation of Accidental Fires and Explosions, University of Utah, USA.

[10] Banerjee, B., 2005. The Mechanical Threshold Stress model for various tempers of 4340 steel. arXiv:cond-mat 0510330, 1–39.

[11] Banerjee, B., 2005. Simulation of impact and fragmentation with the material point method. In: Proc. 11th International Conference on Fracture. Turin, Italy.

[12] Banerjee, B., 2005. Validation of UINTAH: Taylor impact and plasticity models. In: Proc. 2005 Joint ASME/ASCE/SES Conference on Mechanics and Materials (McMat 2005). Baton Rouge, LA.

[13] Bardenhagen, S. G., Guilkey, J. E., Roessig, K. M., BrackBill, J. U., Witzel, W. M., Foster, J. C., 2001. An improved contact algorithm for the material point method and application to stress propagation in granular material. Computer Methods in the Engineering Sciences 2 (4), 509–522.

[14] Bardenhagen, S. G., Kober, E. M., 2004. The generalized interpolation material point method. Comp. Model. Eng. Sci. 5 (6), 477–496.

[15] Barker, L. M., Hollenbach, R. E., 1974. Shock wave study of the $\alpha \rightleftarrows \epsilon$ phase transition in iron. J. Appl. Phys. 45 (11), 4872–4887.

[16] Bazant, Z. P., Belytschko, T., 1985. Wave propagation in a strain-softening bar: Exact solution. ASCE J. Engg. Mech 111 (3), 381–389.

[17] Becker, R., 2002. Ring fragmentation predictions using the gurson model with material stability conditions as failure criteria. Int. J. Solids Struct. 39, 3555–3580.

[18] Bennett, J. G., Haberman, K. S., Johnson, J. N., Asay, B. W., Henson, B. F., 1998. A constitutive model for non-shock ignition and mechanical response of high explosives. J. Mech. Phys. Solids 46 (12), 2303–2322.

[19] Bhawalkar, A., 2006. The verification and validation of material models in a parallel multiphysics code. Master's thesis, Department of Mechanical Engineering, University of Utah, Salt Lake City, UT, USA.

[20] Brown, J. M., Fritz, J. N., Hixson, R. S., 2000. Hugoniot data for iron. J. Appl. Phys. 88 (9), 5496–5498.

[21] Burakovsky, L., Preston, D. L., 2000. Analysis of dislocation mechanism for melting of elements. Solid State Comm. 115, 341–345.

[22] Burakovsky, L., Preston, D. L., Silbar, R. R., 2000. Analysis of dislocation mechanism for melting of elements: pressure dependence. J. Appl. Phys. 88 (11), 6294–6301.

[23] Burakovsky, L., Preston, D. L., Silbar, R. R., 2000. Melting as a dislocation-mediated phase transition. Phys. Rev. B 61 (22), 15011–15018.

[24] Carrington, W. E., Gayler, M. L. V., 1948. The use of flat-ended projectiles for determining dynamic yield stress III. Changes in microstructure caused by deformation under impact at high-striking velocities. Proc. Royal Soc. London A 194 (1038), 323–331.

[25] Chen, S. R., Gray, G. T., 1996. Constitutive behavior of tantalum and tantalum-tungsten alloys. Metall. Mater. Trans. A 27A, 2994–3006.

[26] Chhabildas, L. C., Konrad, C. H., Mosher, D. A., Reinhart, W. D., Duggins, B. D., Trucano, T. G., Summers, R. M., Peery, J. S., 1998. A methodology to validated 3D arbitrary Lagrangian Eulerian codes with applications to ALEGRA. Int. J. Impact Engrg. 23, 101–112.

[27] Chu, C. C., Needleman, A., 1980. Void nucleation effects in biaxially stretched sheets. ASME J. Engg. Mater. Tech. 102, 249–256.

[28] Coplien, J. O., 1992. Advanced C++ Programming Styles and Idioms. Addison-Wesley, Reading, MA.

[29] de St. Germain, J. D., McCorquodale, J., Parker, S. G., Johnson, C. R., Nov 2000. Uintah: a massively parallel problem solving environment. In: Ninth IEEE International Symposium on High Performance and Distributed Computing. IEEE, Piscataway, NJ, pp. 33–41.

[30] Dobrosavljevic, A. S., Maglic, K. D., 1991. Heat capacity and electrical resistivity of copper research material for calorimetry. High Temperatures-High Pressures 23, 129–133.

[31] Drucker, D. C., 1959. A definition of stable inelastic material. J. Appl. Mech. 26, 101–106.

[32] Follansbee, P. S., Kocks, U. F., 1988. A constitutive description of the deformation of copper based on the use of the mechanical threshold stress as an

internal state variable. Acta Metall. 36, 82–93.

[33] Fukuhara, M., Sanpei, A., 1993. Elastic moduli and internal friction of low carbon and stainless steels as a function of temperature. ISIJ International 33 (4), 508–512.

[34] Goto, D. M., Bingert, J. F., Chen, S. R., Gray, G. T., Garrett, R. K., 2000. The mechanical threshold stress constitutive-strength model description of HY-100 steel. Metallurgical and Materials Transactions A 31A, 1985–1996.

[35] Goto, D. M., Bingert, J. F., Reed, W. R., Garrett, R. K., 2000. Anisotropy-corrected MTS constitutive strength modeling in HY-100 steel. Scripta Mater. 42, 1125–1131.

[36] Guilkey, J. E., Harman, T. B., Kashiwa, B. A., McMurtry, P. A., 2004. An Eulerian-Lagrangian approach to large deformation fluid-structure interaction problems, submitted.

[37] Guilkey, J. E., Weiss, J. A., 2003. Implicit time integration for the material point method: Quantitative and algorithmic comparisons with the finite element method. Int. J. Numer. Meth. Engng. 57 (9), 1323–1338.

[38] Guinan, M. W., Steinberg, D. J., 1974. Pressure and temperature derivatives of the isotropic polycrystalline shear modulus for 65 elements. J. Phys. Chem. Solids 35, 1501–1512.

[39] Gurson, A. L., 1977. Continuum theory of ductile rupture by void nucleation and growth: Part 1. Yield criteria and flow rules for porous ductile media. ASME J. Engg. Mater. Tech. 99, 2–15.

[40] Gust, W. H., 1982. High impact deformation of metal cylinders at elevated temperatures. J. Appl. Phys. 53 (5), 3566–3575.

[41] Gust, W. H., Steinberg, D. J., Young, D. A., 1979. Hugoniot parameters to 320 GPa for three types of steel. High Temp. High Pres. 11, 271–280.

[42] Handbook, A., 1978. American Society of Metals Handbook: Volume 1. American Society of Metals, New York.

[43] Hao, S., Liu, W. K., Qian, D., 2000. Localization-induced band and cohesive model. J. Appl. Mech. 67, 803–812.

[44] Hill, R., Hutchinson, J. W., 1975. Bifurcation phenomena in the plane tension test. J. Mech. Phys. Solids 23, 239–264.

[45] Hobart, R., 1965. Peierls stress dependence on dislocation width. J. Appl. Phys. 36 (4), 1944–1948.

[46] Hoge, K. G., Mukherjee, A. K., 1977. The temperature and strain rate dependence of the flow stress of tantalum. J. Mater. Sci. 12, 1666–1672.

[47] House, J. W., Lewis, J. C., Gillis, P. P., Wilson, L. L., 1995. Estimation of the flow stress under high rate plastic deformation. Int. J. Impact Engng. 16 (2), 189–200.

[48] Jansen, H. J. F., Hathaway, K. B., Freeman, A. J., 1984. Structural properties of ferromagnetic bcc iron: A failure of the local-spin-density approximation. Phys. Rev. B 30 (10), 6177–6179, lattice constant for bcc iron.

[49] Johnson, G. R., Cook, W. H., 1983. A constitutive model and data for metals subjected to large strains, high strain rates and high temperatures. In: Proc. 7th International Symposium on Ballistics. pp. 541–547.

[50] Johnson, G. R., Cook, W. H., 1985. Fracture characteristics of three metals subjected to various strains, strain rates, temperatures and pressures. Int. J. Eng. Fract. Mech. 21, 31–48.
[51] Johnson, G. R., Holmquist, T. J., 1988. Evaluation of cylinder-impact test data for constitutive models. J. Appl. Phys. 64 (8), 3901–3910.
[52] Johnson, J. N., Addessio, F. L., 1988. Tensile plasticity and ductile fracture. J. Appl. Phys. 64 (12), 6699–6712.
[53] Jones, S. E., Gillis, P. P., 1987. On the equation of motion of the undeformed section of a Taylor impact specimen. J. Appl. Phys. 61 (2), 499–502.
[54] Katz, S., Doran, D. G., Curran, D. R., 1959. Hugoniot equation of state of aluminum and steel from oblique shock measurements. J. Appl. Phys. 30 (4), 568–576.
[55] Kocks, U. F., 2001. Realistic constitutive relations for metal plasticity. Materials Science and Engrg. A317, 181–187.
[56] Lederman, F. L., Salamon, M. B., Shacklette, L. W., 1974. Experimental verification of scaling and test of the universality hypothesis from specific heat data. Phys. Rev. B 9 (7), 2981–2988.
[57] Lesuer, D. R., Kay, G. J., LeBlanc, M. M., 2001. Modeling large-strain, high-rate deformation in metals. Tech. Rep. UCRL-JC-134118, Lawrence Livermore National Laboratory, Livermore, CA, johnson-Cook plasticity model for 6061T6 Aluminum.
[58] Long, G. T., Wight, C. A., 2002. Thermal decomposition of a melt-castable high explosive: isoconversional analysis of TNAZ. J. Phys. Chem. B 106, 2791–2795.
[59] MacDonald, R. A., MacDonald, W. M., 1981. Thermodynamic properties of fcc metals at high temperatures. Physical Review B 24 (4), 1715–1724.
[60] Marsh, S. P., 1980. LASL Shock Hugoniot Data: Los Alamos series on dynamic material properties. University of California, Berkeley, CA.
[61] Maudlin, P. J., Schiferl, S. K., 1996. Computational anisotropic plasticity for high-rate forming applications. Comput. Methods Appl. Mech. Engrg. 131, 1–30.
[62] McQueen, R. G., Marsh, S. P., Taylor, J. W., Fritz, J. N., Carter, W. J., 1970. The equation of state of solids from shock wave studies. In: Kinslow, R. (Ed.), High Velocity Impact Phenomena. Academic Press, New York, pp. 294–417.
[63] Mitchell, A. C., Nellis, W. J., 1981. Shock compression of aluminum, copper, and tantalum. J. Appl. Phys. 52 (5), 3363–3374.
[64] Nadal, M.-H., Le Poac, P., 2003. Continuous model for the shear modulus as a function of pressure and temperature up to the melting point: analysis and ultrasonic validation. J. Appl. Phys. 93 (5), 2472–2480.
[65] Nemat-Nasser, S., 1991. Rate-independent finite-deformation elastoplasticity: a new explicit constitutive algorithm. Mech. Mater. 11, 235–249.
[66] Nemat-Nasser, S., 2004. Plasticity: A Treatise on Finite Deformation of Heteogeneous Inelastic Materials. Cambridge University Press, Cambridge.
[67] Nemat-Nasser, S., Chung, D. T., 1992. An explicit constitutive algorithm for

large-strain, large-strain-rate elastic-viscoplasticity. Comput. Meth. Appl. Mech. Engrg 95 (2), 205–219.

[68] Oberkampf, W. L., Trucano, T. G., Hirsch, C., 2002. Verification, validation, and predictive capability in computational engineering and physics. In: Verfification and Validation for Modeling and Simulation in Computational Science and Engineering Applications. Foundations for Verfification and Validation in the 21st Century Workshop, Johns Hopkins University, Laurel, Maryland.

[69] Osborne, D. W., Kirby, R. K., 1977. Research material 5, copper heat capacity specimen. Tech. Rep. Report of Investigation, National Bureau of Standards, Gaithersburg, MD.

[70] Overton, W. C., Gaffney, J., 1955. Temperature variation of the elastic constants of cubic elements. I. Copper. Physical Review 98 (4), 969–977.

[71] Perzyna, P., 1998. Constitutive modelling of dissipative solids for localization and fracture. In: P., P. (Ed.), Localization and Fracture Phenomena in Inelastic Solids: CISM Courses and Lectures No. 386. SpringerWien, New York, pp. 99–241.

[72] Preston, D. L., Tonks, D. L., Wallace, D. C., 2003. Model of plastic deformation for extreme loading conditions. J. Appl. Phys. 93 (1), 211–220.

[73] Puchi-Cabrera, E. S., Villabos-Gutiérres, C., Castro-Fariñas, G., April 2001. On the mechanical threshold stress of aluminum: Effect of the alloying content. ASME J. Engg. Mater. Tech. 123, 155–161.

[74] Ramaswamy, S., Aravas, N., 1998. Finite element implementation of gradient plasticity models Part I: Gradient-dependent yield functions. Comput. Methods Appl. Mech. Engrg. 163, 11–32.

[75] Ramaswamy, S., Aravas, N., 1998. Finite element implementation of gradient plasticity models Part II: Gradient-dependent evolution equations. Comput. Methods Appl. Mech. Engrg. 163, 33–53.

[76] Ravichandran, G., Rosakis, A. J., Hodowany, J., Rosakis, P., 2001. On the conversion of plastic work into heat during high-strain-rate deformation. In: Proc. , 12th APS Topical Conference on Shock Compression of Condensed Matter. American Physical Society, pp. 557–562.

[77] Rudnicki, J. W., Rice, J. R., 1975. Conditions for the localization of deformation in pressure-sensitive dilatant materials. J. Mech. Phys. Solids 23, 371–394.

[78] Samanta, S. K., 1971. Dynamic deformation of aluminium and copper at elevated temperatures. J. Mech. Phys. Solids 19, 117–135.

[79] Shacklette, L. W., 1974. Specific heat and resistivity of iron near its Curie point. Phys. Rev. B 9 (9), 3789–3792.

[80] Simo, J. C., Hughes, T. J. R., 1998. Computational Inelasticity. Springer-Verlag, New York.

[81] Steinberg, D. J., Cochran, S. G., Guinan, M. W., 1980. A constitutive model for metals applicable at high-strain rate. J. Appl. Phys. 51 (3), 1498–1504.

[82] Steinberg, D. J., Lund, C. M., 1989. A constitutive model for strain rates from $10^{-}4$ to $10^{}6$ s^{-1}. J. Appl. Phys. 65 (4), 1528–1533.

[83] Sulsky, D., Chen, Z., Schreyer, H. L., 1994. A particle method for history dependent materials. Comput. Methods Appl. Mech. Engrg. 118, 179–196.

[84] Sulsky, D., Zhou, S., Schreyer, H. L., 1995. Application of a particle-in-cell method to solid mechanics. Computer Physics Communications 87, 236–252.

[85] Sutanthavibul, S., et al., 2002. Xfig User Manual Version 3.2.4. http://www.xfig.org.

[86] Taylor, G. I., 1948. The use of flat-ended projectiles for determining dynamic yield stress I. Theoretical considerations. Proc. Royal Soc. London A 194 (1038), 289–299.

[87] Tvergaard, V., Needleman, A., 1984. Analysis of the cup-cone fracture in a round tensile bar. Acta Metall. 32 (1), 157–169.

[88] Tvergaard, V., Needleman, A., 1990. Ductile failure modes in dynamically loaded notched bars. In: Ju, J. W., Krajcinovic, D., Schreyer, H. L. (Eds.), Damage Mechanics in Engineering Materials: AMD 109/MD 24. American Society of Mechanical Engineers, New York, NY, pp. 117–128.

[89] Varshni, Y. P., 1970. Temperature dependence of the elastic constants. Physical Rev. B 2 (10), 3952–3958.

[90] Wallace, D. C., Sidles, P. H., Danielson, G. C., 1960. Specific heat of high purity iron by a pulse heating method. J. Appl. Phys. 31 (1), 168–176.

[91] Wang, L. H., Atluri, S. N., 1994. An analysis of an explicit algorithm and the radial return algorithm, and a proposed modification, in finite elasticity. Computational Mechanics 13, 380–389.

[92] Wang, Y., Chen, D., Zhang, X., 2000. Calculated equation of stae of Al, Cu, Ta, Mo, and W to 1000 GPa. Physical Review Letters 84 (15), 3220–3223.

[93] Whiffin, A. C., 1948. The use of flat-ended projectiles for determining dynamic yield stress II. Tests on various metallic materials. Proc. Royal Soc. London A 194 (1038), 300–322.

[94] Wilkins, M. L., 1999. Computer Simulation of Dynamic Phenomena. Springer-Verlag, Berlin.

[95] Wilkins, M. L., Guinan, M. W., 1973. Impact of cylinders on a rigid boundary. J. Appl. Phys. 44 (3), 1200–1206.

[96] Williams, Q., Jeanloz, R., Bass, J., Svendsen, B., Ahrens, T. J., 1987. The melting curve of iron to 250 gigapascals: a constraint of the temperature at earth's center. Science 236, 181–182.

[97] Yoo, C. S., Holmes, N. C., Ross, M., 1993. Shock temperatures and melting of iron at earth core conditions. Phys. Rev. Lett. 70 (25), 3931–3934.

[98] Zerilli, F. J., 2004. Dislocation mechanics-based constitutive equations. Metall. Mater. Trans. A 35A, 2547–2555.

[99] Zerilli, F. J., Armstrong, R. W., 1987. Dislocation-mechanics-based constitutive relations for material dynamics calculations. J. Appl. Phys. 61 (5), 1816–1825.

[100] Zerilli, F. J., Armstrong, R. W., 1993. Constitutive relations for the plastic deformation of metals. In: High-Pressure Science and Technology - 1993. American Institute of Physics, Colorado Springs, Colorado, pp. 989–992.

[101] Zocher, M. A., Maudlin, P. J., Chen, S. R., Flower-Maudlin, E. C., 2000. An evaluation of several hardening models using Taylor cylinder impact data. In: Proc. , European Congress on Computational Methods in Applied Sciences and Engineering. ECCOMAS, Barcelona, Spain.

A The Material Point Method

The Material Point Method (MPM) Sulsky et al. [83] is a particle method for structural mechanics simulations. In this method, the state variables of the material are described on Lagrangian particles or "material points". In addition, a regular, structured Eulerian grid is used as a computational scratch pad to compute spatial gradients and to solve the governing conservation equations. An explicit time-stepping version of the Material Point Method has been used in the simulations presented in this paper. The MPM algorithm is summarized below Sulsky et al. [84] for the sake of completeness.

It is assumed that an particle state at the beginning of a time step is known. The mass (m), external force ($\boldsymbol{f}^{\text{ext}}$), and velocity ($\boldsymbol{v}$) of the particles are interpolated to the grid using the relations

$$m_g = \sum_p S_{gp}\, m_p\ , \quad \boldsymbol{v}_g = (1/m_g) \sum_p S_{gp}\, m_p\, \boldsymbol{v}_p\ , \quad \boldsymbol{f}_g^{\text{ext}} = \sum_p S_{gp}\, \boldsymbol{f}_p^{\text{ext}} \tag{A.1}$$

where the subscript (g) indicates a quantity at a grid node and a subscript (p) indicates a quantity on a particle. The symbol $\sum_p$ indicates a summation over all particles. The quantity (S_{gp}) is the interpolation function of node (g) evaluated at the position of particle (p). Details of the interpolants used can be found elsewhere Bardenhagen and Kober [14].

Next, the velocity gradient at each particle is computed using the grid velocities using the relation

$$\boldsymbol{\nabla v}_p = \sum_g \boldsymbol{G}_{gp} \boldsymbol{v}_g \tag{A.2}$$

where $\boldsymbol{G}_{gp}$ is the gradient of the shape function of node (g) evaluated at the position of particle (p). The velocity gradient at each particle is used to determine the Cauchy stress ($\boldsymbol{\sigma}_p$) at the particle using a stress update algorithm.

The internal force at the grid nodes ($\boldsymbol{f}_g^{\text{int}}$) is calculated from the divergence of the stress using

$$\boldsymbol{f}_g^{\text{int}} = \sum_p \boldsymbol{G}_{gp}\, \boldsymbol{\sigma}_p\, V_p \tag{A.3}$$

where V_p is the particle volume.

The equation for the conservation of linear momentum is next solved on the

grid. This equation can be cast in the form

$$\boldsymbol{m}_g \, a_g = \boldsymbol{f}_g^{\text{ext}} - \boldsymbol{f}_g^{\text{int}} \tag{A.4}$$

where $\boldsymbol{a}_g$ is the acceleration vector at grid node (g).

The velocity vector at node (g) is updated using an explicit (forward Euler) time integration, and the particle velocity and position are then updated using grid quantities. The relevant equations are

$$\boldsymbol{v}_g(t + \Delta t) = \boldsymbol{v}_g(t) + \boldsymbol{a}_g \, \Delta t \tag{A.5}$$

$$\boldsymbol{v}_p(t + \Delta t) = \boldsymbol{v}_p(t) + \sum_g S_{gp} \, \boldsymbol{a}_g \, \Delta t \; ; \quad \boldsymbol{x}_p(t + \Delta t) = \boldsymbol{x}_p(t) + \sum_g S_{gp} \, \boldsymbol{v}_g \, \Delta t \tag{A.6}$$

The above sequence of steps is repeated for each time step. The above algorithm leads to particularly simple mechanisms for handling contact. Details of these contact algorithms can be found elsewhere Bardenhagen et al. [13].

B Stress Update Algorithm

A modified form of a hypoelastic-plastic, semi-implicit elastic-plastic stress update algorithm (Nemat-Nasser [65], Nemat-Nasser and Chung [67], Wang and Atluri [91], Maudlin and Schiferl [61], Zocher et al. [101]) has been used for the stress update in the simulations presented in this paper. An additive decomposition of the rate of deformation tensor into elastic and plastic parts has been assumed. One advantage of this approach is that it can be used for both low and high strain rates. Another advantage is that many strain-rate and temperature-dependent plasticity and damage models are based on the assumption of additive decomposition of strain rates, making their implementation straightforward.

The stress update is performed in a co-rotational frame which is equivalent to using the Green-Naghdi objective stress rate. The accuracy of model is good if elastic strains are small compared to plastic strains and the material is not unloaded completely from a plastic state. It is also assumed that the stress tensor can be divided into a volumetric and a deviatoric component. The plasticity model is used to update only the deviatoric component of stress assuming isochoric behavior. The hydrostatic component of stress is updated using a solid equation of state.

In the general case, a particle is tagged as “failed” when its temperature is greater than the melting point of the material at the applied pressure. An additional condition for failure is when the porosity of a particle increases beyond a critical limit. A final condition for failure is when a bifurcation condition such as the

Drucker stability postulate is satisfied. Upon failure, a particle is either removed from the computation by setting the stress to zero or is converted into a material with a different velocity field which interacts with the remaining particles via contact. Either approach leads to the simulation of a newly created surface. However, this option was turned off in the simulations discussed in this paper.

In the parallel implementation of the stress update algorithm, sockets have been added to allow for the incorporation of a variety of plasticity, damage, yield, and bifurcation models without requiring any change in the stress update code. The algorithm is shown in Algorithm 1. The equation of state, plasticity model, yield condition, damage model, and the stability criterion are all polymorphic objects created using a factory idiom in C++ (Coplien [28]).

The elastic-plastic stress update process is discussed below. Following Maudlin and Schiferl [61], the rotated spatial rate of deformation tensor ($\boldsymbol{d}$) is decomposed into an elastic part ($\boldsymbol{d}^e$) and a plastic part ($\boldsymbol{d}^p$)

$$\boldsymbol{d} = \boldsymbol{d}^e + \boldsymbol{d}^p \tag{B.1}$$

If we assume plastic incompressibility ($\mathrm{tr}(\boldsymbol{d}^p) = 0$), we get

$$\boldsymbol{\eta} = \boldsymbol{\eta}^e + \boldsymbol{\eta}^p \tag{B.2}$$

where $\boldsymbol{\eta}$, $\boldsymbol{\eta}^e$, and $\boldsymbol{\eta}^p$ are the deviatoric parts of $\boldsymbol{d}$, $\boldsymbol{d}^e$, and $\boldsymbol{d}^p$, respectively. For isotropic materials, the hypoelastic constitutive equation for deviatoric stress is

$$\dot{\boldsymbol{s}} = 2\mu(\boldsymbol{\eta} - \boldsymbol{\eta}^p) \tag{B.3}$$

where $\boldsymbol{s}$ is the deviatoric part of the stress tensor and μ is the shear modulus. We assume that the flow stress obeys the Huber-von Mises yield condition

$$f := \sqrt{\frac{3}{2}}\|\boldsymbol{s}\| - \sigma_y \leq 0 \;\text{ or, }\; F := \frac{3}{2}\boldsymbol{s} : \boldsymbol{s} - \sigma_y^2 \leq 0 \tag{B.4}$$

where σ_y is the flow stress. Assuming an associated flow rule, and noting that $\boldsymbol{d}^p = \boldsymbol{\eta}^p$, we have

$$\boldsymbol{\eta}^p = \boldsymbol{d}^p = \lambda\frac{\partial f}{\partial \boldsymbol{\sigma}} = \Lambda\frac{\partial F}{\partial \boldsymbol{\sigma}} = 3\Lambda\boldsymbol{s} \tag{B.5}$$

where $\boldsymbol{\sigma}$ is the stress. Let $\boldsymbol{u}$ be a tensor proportional to the plastic straining direction, and define γ as

$$\boldsymbol{u} = \sqrt{3}\frac{\boldsymbol{s}}{\|\boldsymbol{s}\|}; \quad \gamma := \sqrt{3}\Lambda\|\boldsymbol{s}\| \quad \Longrightarrow \gamma\boldsymbol{u} = 3\Lambda\boldsymbol{s} \tag{B.6}$$

Therefore, we have

$$\boldsymbol{\eta}^p = \gamma\boldsymbol{u}; \quad \dot{\boldsymbol{s}} = 2\mu(\boldsymbol{\eta} - \gamma\boldsymbol{u}) \tag{B.7}$$

Algorithm 1. Stress Update Algorithm

Persistent:Initial moduli, temperature, porosity,
scalar damage, equation of state, plasticity model,
yield condition, stability criterion, damage model
Temporary:Particle state at time t
Output: Particle state at time $t + \Delta t$

For *all the patches in the domain*
Read the particle data and initialize updated data storage
For *all the particles in the patch*
Compute the velocity gradient and the rate of deformation tensor
Compute the deformation gradient and the rotation tensor
Rotate the Cauchy stress and the rate of deformation tensor
to the material configuration
Compute the current shear modulus and melting temperature
Compute the pressure using the equation of state,
update the hydrostatic stress, and
compute the trial deviatoric stress
Compute the flow stress using the plasticity model
Evaluate the yield function
If *particle is elastic*
Update the elastic deviatoric stress from the trial stress
Rotate the stress back to laboratory coordinates
Update the particle state
Else
Compute the elastic-plastic deviatoric stress
Compute updated porosity, scalar damage, and
temperature increase due to plastic work
Compute elastic-plastic tangent modulus and evaluate stability condition
Rotate the stress back to laboratory coordinates
Update the particle state
End If
If *Temperature* $>$ *Melt Temperature* or *Porosity* $>$ *Critical Porosity* or *Unstable*
Tag particle as failed
End If
Convert failed particles into a material with a different velocity field
End For
End For

From the consistency condition, if we assume that the deviatoric stress remains constant over a timestep, we get

$$\gamma = \frac{\boldsymbol{s} : \boldsymbol{\eta}}{\boldsymbol{s} : \boldsymbol{u}} \tag{B.8}$$

which provides an initial estimate of the plastic strain rate. To obtain a semi-implicit update of the stress using equation (B.7), we define

$$\tau^2 := \frac{3}{2}\boldsymbol{s} : \boldsymbol{s} = \sigma_y^2 \tag{B.9}$$

Taking a time derivative of equation (B.9) gives us

$$\sqrt{2}\dot{\tau} = \sqrt{3}\frac{\boldsymbol{s} : \dot{\boldsymbol{s}}}{\|\boldsymbol{s}\|} \tag{B.10}$$

Plugging equation (B.10) into equation $(B.7)_2$ we get

$$\dot{\tau} = \sqrt{2}\mu(\boldsymbol{u} : \boldsymbol{\eta} - \gamma \boldsymbol{u} : \boldsymbol{u}) = \sqrt{2}\mu(d - 3\gamma) \tag{B.11}$$

where $d = \boldsymbol{u} : \boldsymbol{\eta}$. If the initial estimate of the plastic strain rate is that all of the deviatoric strain rate is plastic, then we get an approximation to γ, and the corresponding error (γ_{er}) given by

$$\gamma_{\text{approx}} = \frac{d}{3}; \quad \gamma_{\text{er}} = \gamma_{\text{approx}} - \gamma = \frac{d}{3} - \gamma \tag{B.12}$$

The incremental form of the above equation is

$$\Delta\gamma = \frac{d^*\Delta t}{3} - \Delta\gamma_{\text{er}} \tag{B.13}$$

Integrating equation (B.11) from time t_n to time $t_{n+1} = t_n + \Delta t$, and using equation (B.13) we get

$$\tau_{n+1} = \tau_n + \sqrt{2}\mu(d^*\Delta t - 3\Delta\gamma) = \tau_n + 3\sqrt{2}\mu\Delta\gamma_{\text{er}} \tag{B.14}$$

where d^* is the average value of d over the timestep. Solving for $\Delta\gamma_{\text{er}}$ gives

$$\Delta\gamma_{\text{er}} = \frac{\tau_{n+1} - \tau_n}{3\sqrt{2}\mu} = \frac{\sqrt{2}\sigma_y - \sqrt{3}\|\boldsymbol{s}_n\|}{6\mu} \tag{B.15}$$

The direction of the total strain rate ($\boldsymbol{u}^\eta$) and the direction of the plastic strain rate ($\boldsymbol{u}^s$) are given by

$$\boldsymbol{u}^\eta = \frac{\boldsymbol{\eta}}{\|\boldsymbol{\eta}\|}; \quad \boldsymbol{u}^s = \frac{\boldsymbol{s}}{\|\boldsymbol{s}\|} \tag{B.16}$$

Let θ be the fraction of the time increment that sees elastic straining. Then

$$\theta = \frac{d^* - 3\gamma_n}{d^*} \tag{B.17}$$

where $\gamma_n = d_n/3$ is the value of γ at the beginning of the timestep. We also assume that

$$d^* = \sqrt{3}\boldsymbol{\eta} : [(1-\theta)\boldsymbol{u}^\eta + \frac{\theta}{2}(\boldsymbol{u}^\eta + \boldsymbol{u}^s)] \tag{B.18}$$

Plugging equation (B.17) into equation (B.18) we get a quadratic equation that can be solved for d^* as follows

$$\frac{2}{\sqrt{3}}(d^*)^2 - (\boldsymbol{\eta} : \boldsymbol{u}^s + \|\boldsymbol{\eta}\|)d^* + 3\gamma_n(\boldsymbol{\eta} : \boldsymbol{u}^s - \|\boldsymbol{\eta}\|) = 0 \tag{B.19}$$

The real positive root of the above quadratic equation is taken as the estimate for d. The value of $\Delta\gamma$ can now be calculated using equations (B.13) and (B.15). A semi-implicit estimate of the deviatoric stress can be obtained at this stage by integrating equation $(B.7)_2$

$$\tilde{\boldsymbol{s}}_{n+1} = \boldsymbol{s}_n + 2\mu\left(\eta\Delta t - \sqrt{3}\Delta\gamma\frac{\tilde{\boldsymbol{s}}_{n+1}}{\|\boldsymbol{s}_{n+1}\|}\right) \tag{B.20}$$

$$= \boldsymbol{s}_n + 2\mu\left(\eta\Delta t - \frac{3}{\sqrt{2}}\Delta\gamma\frac{\tilde{\boldsymbol{s}}_{n+1}}{\sigma_y}\right) \tag{B.21}$$

Solving for $\tilde{\boldsymbol{s}}_{n+1}$, we get

$$\tilde{\boldsymbol{s}}_{n+1} = \frac{\boldsymbol{s}^{\text{trial}}_{n+1}}{1 + 3\sqrt{2}\mu\dfrac{\Delta\gamma}{\sigma_y}} \tag{B.22}$$

where $\boldsymbol{s}^{\text{trial}}_{n+1} = \boldsymbol{s}_n + 2\mu\Delta t\boldsymbol{\eta}$. A final radial return adjustment is used to move the stress to the yield surface

$$\boldsymbol{s}_{n+1} = \sqrt{\frac{2}{3}}\sigma_y\frac{\tilde{\boldsymbol{s}}_{n+1}}{\|\tilde{\boldsymbol{s}}_{n+1}\|} \tag{B.23}$$

A pathological situation arises if $\gamma_n = \boldsymbol{u}_n : \boldsymbol{\eta}_n$ is less than or equal to zero or $\Delta\gamma_{\text{er}} \geq \frac{d^*}{3}\Delta t$. This can occur is the rate of plastic deformation is small compared to the rate of elastic deformation or if the timestep size is too small (see Nemat-Nasser and Chung [67]). In such situations, we use a locally implicit stress update that uses Newton iterations (as discussed in Simo and Hughes [80], page 124) to compute $\tilde{\boldsymbol{s}}$.

Since the material in the container may unload locally after fracture, the hypoelastic-plastic stress update may not work accurately under certain circumstances. An improvement would be to use a hyperelastic-plastic stress update algorithm. Also, the plasticity models are temperature dependent. Hence there is the issue of severe mesh dependence due to change of the governing equations from hyperbolic to elliptic in the softening regime (Hill and Hutchinson [44], Bazant and Belytschko [16], Tvergaard and Needleman [88]). Viscoplastic stress update models or nonlocal/gradient plasticity models (Ramaswamy and Aravas [74], Hao et al. [43]) can be used to eliminate some of these effects and are currently under investigation.

C Computation of Metrics

The length of the elastic zone after deformation (X_f) is determined by checking the deformed diameter with the original diameter of the cylinder. If the difference is greater than 0.003 mm, plastic deformation is assumed to have taken place. The value of X_f is the distance from the free end of the cylinder to the first point from the free end where the above criterion is met.

Let the closed polygon representing the final profile of the Taylor cylinder be given by $P = p_1, p_2, p_3, ..., p_n, p_{n+1} = p_1$, where n is the number of vertices of the polygon. We assume that the points are ordered in the counter-clockwise direction. Each point p_i has a pair of coordinates (x_i, y_i).

Then, the area of the profile (A_f) is given by

$$A_f = \frac{1}{2}\sum_{i=1}^{n}(x_i\ y_{i+1} - x_{i+1}\ y_i)\ . \tag{C.1}$$

The centroid of the profile is given by

$$C_{xf} = \frac{1}{6A_f}\sum_{i=1}^{n}(x_i\ y_{i+1} - x_{i+1}\ y_i)(x_i + x_{i+1}) \tag{C.2}$$

$$C_{yf} = \frac{1}{6A_f}\sum_{i=1}^{n}(x_i\ y_{i+1} - x_{i+1}\ y_i)(y_i + y_{i+1})\ . \tag{C.3}$$

The volume of the deformed cylinder is given by the Pappus theorem. The formula for the volume is

$$V_f = 2\pi C_{xf} A_f\ . \tag{C.4}$$

The moments of inertia are computed by converting the volume integral into a surface integral over the boundary of the profile. The resulting formulas for the moments of inertia are

$$I_{xf} = -\frac{1}{12}\sum_{i=1}^{n}(x_{i+1} - x_i)(y_{i+1} + y_i)(y_{i+1}^2 + y_i^2) \tag{C.5}$$

$$I_{yf} = \frac{1}{12}\sum_{i=1}^{n}(y_{i+1} - y_i)(x_{i+1} + x_i)(x_{i+1}^2 + x_i^2)\ . \tag{C.6}$$

D Approach and models for simulating particle erosion

A particle is tagged as "failed" when its temperature is greater than the melting point of the material at the applied pressure. An additional condition for failure is when the porosity of a particle increases beyond a critical limit and the strain exceeds the fracture strain of the material. Another condition for failure is when a material bifurcation condition such as the Drucker stability postulate is satisfied. Upon failure, a particle is either removed from the computation by setting the stress to zero or is converted into a material with a different velocity field which interacts with the remaining particles via contact. Either approach leads to the simulation of a newly created surface. More details of the approach can be found in Banerjee [6, 7, 11].

When failure is to be simulated we use the Gurson-Tvergaard-Needleman yield condition instead of the von Mises condition. The Gurson-Tvergaard-Needleman (GTN) yield condition [39, 87] depends on porosity. An associated flow rule is used to determine the plastic rate parameter in either case. The GTN yield condition can be written as

$$\Phi = \left(\frac{\sigma_{eq}}{\sigma_f}\right)^2 + 2q_1 f_* \cosh\left(q_2 \frac{Tr(\sigma)}{2\sigma_f}\right) - (1 + q_3 f_*^2) = 0 \tag{D.1}$$

where q_1, q_2, q_3 are material constants and f_* is the porosity (damage) function given by

$$f* = \begin{cases} f & \text{for } f \leq f_c, \\ f_c + k(f - f_c) & \text{for } f > f_c \end{cases} \tag{D.2}$$

where k is a constant and f is the porosity (void volume fraction). The flow stress in the matrix material is computed using either of the two plasticity models discussed earlier. Note that the flow stress in the matrix material also remains on the undamaged matrix yield surface and uses an associated flow rule.

The evolution of porosity is calculated as the sum of the rate of growth and the rate of nucleation [75]. The rate of growth of porosity and the void nucleation rate are given by the following equations [27]

$$\dot{f} = \dot{f}_{\text{nucl}} + \dot{f}_{\text{grow}} \tag{D.3}$$

$$\dot{f}_{\text{grow}} = (1 - f)\text{Tr}(\boldsymbol{D}_p) \tag{D.4}$$

$$\dot{f}_{\text{nucl}} = \frac{f_n}{(s_n\sqrt{2\pi})} \exp\left[-\frac{1}{2}\frac{(\epsilon_p - \epsilon_n)^2}{s_n^2}\right] \dot{\epsilon}_p \tag{D.5}$$

where $\boldsymbol{D}_p$ is the rate of plastic deformation tensor, f_n is the volume fraction of void nucleating particles , ϵ_n is the mean of the distribution of nucleation strains, and s_n is the standard deviation of the distribution.

Under normal conditions, the heat generated at a material point is conducted away at the end of a time step using the heat equation. If special adiabatic conditions apply (such as in impact problems), the heat is accumulated at a material point and is not conducted to the surrounding particles. This localized heating can be used to determine whether a material point has melted.

After the stress state has been determined on the basis of the yield condition and the associated flow rule, a scalar damage state in each material point can be calculated using the Johnson-Cook model [50]. The Johnson-Cook model has an explicit dependence on temperature, plastic strain, ans strain rate.

The damage evolution rule for the Johnson-Cook damage model can be written as

$$\dot{D} = \frac{\dot{\epsilon_p}}{\epsilon_p^f}\,;\ \epsilon_p^f = \left[D_1 + D_2 \exp\left(\frac{D_3}{3}\sigma^*\right)\right]\left[1 + D_4 \ln(\dot{\epsilon_p}^*)\right]\left[1 + D_5 T^*\right]\ ;\ \sigma^* = \frac{\mathrm{Tr}(\boldsymbol{\sigma})}{\sigma_{eq}}\,; \tag{D.6}$$

where D is the damage variable which has a value of 0 for virgin material and a value of 1 at fracture, ϵ_p^f is the fracture strain, D_1, D_2, D_3, D_4, D_5 are constants, $\boldsymbol{\sigma}$ is the Cauchy stress, and T^* is the scaled temperature as in the Johnson-Cook plasticity model.

The determination of whether a particle has failed can be made on the basis of either or all of the following conditions:

- The particle temperature exceeds the melting temperature.
- The TEPLA-F fracture condition [52] is satisfied. This condition can be written as
$$(f/f_c)^2 + (\epsilon_p/\epsilon_p^f)^2 = 1 \tag{D.7}$$
where f is the current porosity, f_c is the maximum allowable porosity, ϵ_p is the current plastic strain, and ϵ_p^f is the plastic strain at fracture.
- An alternative to ad-hoc damage criteria is to use the concept of bifurcation to determine whether a particle has failed or not. Two stability criteria have been explored in this paper - the Drucker stability postulate [31] and the loss of hyperbolicity criterion (using the determinant of the acoustic tensor) [77, 71].

The simplest criterion that can be used is the Drucker stability postulate [31] which states that time rate of change of the rate of work done by a material cannot be negative. Therefore, the material is assumed to become unstable (and a particle fails) when

$$\dot{\boldsymbol{\sigma}} : \boldsymbol{D}^p \leq 0 \tag{D.8}$$

Another stability criterion that is less restrictive is the acoustic tensor criterion which states that the material loses stability if the determinant of the acoustic tensor changes sign [77, 71]. Determination of the acoustic tensor requires a search for a normal vector around the material point and is therefore computationally expensive.

A simplification of this criterion is a check which assumes that the direction of instability lies in the plane of the maximum and minimum principal stress [17]. In this approach, we assume that the strain is localized in a band with normal $\boldsymbol{n}$, and the magnitude of the velocity difference across the band is $\boldsymbol{g}$. Then the bifurcation condition leads to the relation

$$R_{ij}g_j = 0 \; ; \quad R_{ij} = M_{ikjl}n_k n_l + M_{ilkj}n_k n_l - \sigma_{ik}n_j n_k \tag{D.9}$$

where M_{ijkl} are the components of the co-rotational tangent modulus tensor and σ_{ij} are the components of the co-rotational stress tensor. If $\det(R_{ij}) \leq 0$, then g_j can be arbitrary and there is a possibility of strain localization. If this condition for loss of hyperbolicity is met, then a particle deforms in an unstable manner and failure can be assumed to have occurred at that particle. We use a combination of these criteria to simulate failure.

Since the material in the container may unload locally after fracture, the hypoelastic-plastic stress update may not work accurately under certain circumstances. An improvement would be to use a hyperelastic-plastic stress update algorithm. Also, the plasticity models are temperature dependent. Hence there is the issue of severe mesh dependence due to change of the governing equations from hyperbolic to elliptic in the softening regime [44, 16, 88]. Viscoplastic stress update models or nonlocal/gradient plasticity models [74, 43] can be used to eliminate some of these effects and are currently under investigation.